

**AEROSOL DIRECT RADIATIVE EFFECTS AND HEATING
IN THE NEW ERA OF ACTIVE SATELLITE OBSERVATIONS**

By

Alexander V. Matus

A dissertation submitted in partial fulfillment of
the requirements for the degree of

Doctor of Philosophy

(Atmospheric and Oceanic Sciences)

at the

UNIVERSITY OF WISCONSIN–MADISON

2017

Date of final oral examination: 7/17/2017

The dissertation is approved by the following members of the Final Oral Committee:

Tristan S. L'Ecuyer, Professor, Atmospheric and Oceanic Sciences

Grant W. Petty, Professor, Atmospheric and Oceanic Sciences

Tracey Holloway, Professor, Atmospheric and Oceanic Sciences

R. Bradley Pierce, Adjunct Assistant Professor, Atmospheric and Oceanic Sciences

Ankur R. Desai, Professor, Atmospheric and Oceanic Sciences

**Copyright © 2017
Alexander V. Matus
All Rights Reserved**

ACKNOWLEDGMENTS

Reflecting on my journey as a graduate student, I realize words cannot begin to adequately express my gratitude to everyone who has helped me along the way. There are so many people who believed in me and helped me get to the point where I am today. I consider myself incredibly lucky to be in this position – to have the opportunity to attend graduate school and pursue a meaningful career. Very few people in the world are afforded such a golden opportunity, which is the reason why I am so grateful to be here and do not take any of it for granted.

First and foremost, I would like to thank my advisor Professor Tristan L’Ecuyer. What I admire most about Tristan is that he dreams big. When I first met Tristan in August 2011, we were both just starting out at the UW-Madison. Tristan was looking for students and I was looking for an advisor. We met in Tristan’s office and he shared his big vision for the research group. I took notes as Tristan excitedly described his vision to pursue ambitious cutting-edge research projects, conduct fieldwork abroad in exotic locations, and build a large network of collaborators both domestic and international. At the time, honestly, this plan seemed unbelievable and unrealistic. Tristan had no funding, no students, we were in an empty office with no furniture and I was sitting on a stool. To say this made a strong impression on me would be a major understatement. Six years later, as I look back on those notes, I am inspired by the realization that everything that Tristan originally dreamed for the group has come true. As Tristan’s first graduate student, I am humbled and honored to be a part of this journey and gratified that I could help play a role in turning this dream into a reality.

Second, I wish to thank my Ph.D. dissertation committee (Profs. Tristan L’Ecuyer, Grant Petty, Tracey Holloway, Brad Pierce, and Ankur Desai). Thank you for all the advice you have provided throughout the process of completing my dissertation. Your ideas, inquiries, and insights have challenged me to be a better researcher, challenged me to be a better writer, and challenged me to be a better scientist. Because of you, I have learned the importance of asking good questions, thinking deeply about research, and trusting the scientific method. You have always been fair, open, and honest and I appreciate all that you have done. Thank you for being phenomenal instructors and for giving me and countless other students an outstanding educational experience. Last but not least, I

would like to give a special thanks to Professor Grant Petty for providing research funding during my first semester at UW-Madison. This support enabled me to have a smooth transition to graduate school and for that I am truly grateful.

Third, I wish to thank everyone in the AOS department. I especially want to thank all my officemates over the years (Ke Li, Mark Smalley, Ethan Nelson, Tracey Dorian, Kristof Van Tricht, Kai-Wei Chang, Will Hahn, and Josh Weber) and members of our research group for their support. I wish you the best and I am sure you will all be very successful in your careers post-graduate school. I am grateful to our administrative staff for all their work to keep the department running smoothly and Pete Pokrandt for his amazing feats of computer wizardry. I especially would like to acknowledge Dave Henderson, Norm Wood, and Phil Partain for their support in the continued development of CloudSat products. Satellites have always fascinated me so it has been a dream come true to pursue my interests at UW-Madison, the Mecca of satellite meteorology. Thank you to all faculty, staff, and students for letting me be a part of the AOS community.

Most importantly, I would like to thank my family. My Mom, Dad, and brother John – you are the reason why I dream big and work hard. You deserve as much credit for this accomplishment as anyone. You have always been there for me and none of this would have been possible without your love, support, and encouragement. The path as a graduate student has been unpredictable with twists and turns that I could never have imagined. Throughout it all, you have been a constant source of inspiration and motivation to continue moving forward. You have been my biggest fans since day one and it means everything to me. I can't thank you enough.

TABLE OF CONTENTS

	Page
LIST OF TABLES	vi
LIST OF FIGURES	viii
ABSTRACT	xiv
1 Introduction	1
1.1 Overview of atmospheric aerosols	1
1.2 Climate impacts of aerosols	2
1.3 Aerosol direct effects	3
1.4 Significance of research	7
1.5 Research questions	9
2 Previous Assessments of Aerosol Direct Effects	20
2.1 Overview	20
2.2 Aerosol measurement capabilities	20
2.2.1 Ground-based networks	21
2.2.2 Intensive field campaigns	21
2.2.3 Satellite remote sensing	22
2.3 Satellite-based estimates	23
2.3 Model-based estimates	25
2.3 Reducing uncertainties in estimates	26
2.3 Remaining questions	27
3 Data and Methodology	31
3.1 Overview	31
3.2 The A-Train satellite constellation	31
3.3 CloudSat’s 2B-FLXHR-LIDAR	33
3.3.1 Product description	33
3.3.2 Algorithm performance	37
3.4 Community Earth System Model (CESM)	40
3.5 Methodology	41
3.5.1 Classifying surface types	43
3.5.2 Classifying sky types	44

	Page
4 The Influence of Cloud Cover on Aerosol Direct Effects	54
4.1 Introduction	54
4.2 Methodology	57
4.3 Global aerosol direct effects	61
4.4 Evidence of the importance of cloud cover	66
4.4.1 Marine aerosols over the SE Pacific Ocean	66
4.4.2 Biomass aerosols over the SE Atlantic Ocean	69
4.5 Chapter summary	72
5 The Self-lofting of Aerosols by Solar Radiative Heating	89
5.1 Introduction	89
5.2 Methodology	92
5.3 Aerosol heating rates	93
5.4 Potential for self-lofting aerosols	95
5.5 Chapter summary	98
6 The Contribution of Direct Radiative Forcing by Aerosol Type	111
6.1 Introduction	111
6.2 Methodology	115
6.3 CALIPSO aerosol type classification	116
6.4 Direct radiative effects by aerosol type	117
6.5 Satellite-based estimates of aerosol direct radiative forcing	119
6.6 Chapter summary	120
7 Conclusions	136
7.1 Summary	136
7.2 Broader impacts	138
7.3 Future work	138

Appendix	141
A.1 Introduction	141
A.2 New updates to 2B-FLXHR-LIDAR	144
A.3 Algorithm performance	145
A.4 Global cloud radiative effects	148
A.5 Effects of mixed-phase clouds	151
A.5.1 Global distribution	151
A.5.2 Implications for heat transport	153
A.6 Mixed-phase cloud regimes	154
A.7 Summary	155

LIST OF TABLES

Table	Page
2.1	Satellite-based estimates of annual mean DRE (W m^{-2}) at the top-of-atmosphere and surface, as evaluated over ocean and land surfaces separately. 29
2.2	Model-based estimates of annual mean DRE (W m^{-2}) at the top-of-atmosphere and surface, as evaluated over ocean and land surfaces separately. 30
3.1	The bias and RMSE (in parentheses) of fluxes, in W m^{-2} , from R05 2B-FLXHR-LIDAR relative to CERES averaged over a range of time and spatial scale. 46
3.2	Bias and Root-Mean-Square Differences (RMSD) of fluxes, in percent, from 2B-FLXHR-LIDAR relative to CERES for scenes containing a given cloud phase (liquid, ice, mixed-phase, and multilayered). 47
4.1	Optical properties of the six CALIPSO aerosol types in the visible band, including mean radii for both fine and coarse modes, single scattering albedo, and asymmetry parameter. . 75
4.2	Global estimates of annual mean DRE (W m^{-2}) from 2B-FLXHR-LIDAR and CESM1(CAM5) datasets. The fractional occurrence for each category is shown in parentheses. For this analysis, sea ice is included in the land category. 76
4.3	Annual mean DRE (W m^{-2}) over the southeastern Pacific Ocean (35° - 5° S, 130° - 65° W) from 2B-FLXHR-LIDAR and CESM1(CAM5) datasets. The fractional occurrence for each category is shown in parentheses. 77
4.4	Annual mean DRE (W m^{-2}) over the southeastern Atlantic Ocean (25° S- 0° , 10° W- 30° E) from 2B-FLXHR-LIDAR and CESM1(CAM5) datasets. The fractional occurrence for each category is shown in parentheses. The standard deviations, σ , of the 2.5° -binned estimates are also reported. 78
5.1	Each CALIPSO aerosol type is assigned a lidar ratio representing the fraction of extinction to backscatter signal. The lidar ratio is determined based on a cluster analysis of AERONET observations and are used to retrieve extinction profiles for each CALIPSO overpass (Omar et al., 2009). 100

6.1	Global estimates of aerosol direct radiative forcing between 1750 and 2011 of seven aerosol components in the IPCC SAR, TAR, AR4, and AR5 reports (Myhre et al., 2013).	122
6.2	Global estimates of annual mean direct radiative effect (W m^{-2}) and anthropogenic direct radiative forcing (W m^{-2}) separated by four aerosol type classification using 2B-FLXHR-LIDAR. The pollution classification represents the combination of polluted continental and polluted dust subtypes from CALIPSO.	123
A.1	Summary of phase-separated global mean cloud radiative effects (top) and differences between the northern and southern hemispheres (bottom), in W m^{-2} . Both SW and LW effects from liquid, ice, mixed-phase, and multilayered clouds are computed at the top of atmosphere (TOA), surface (SFC), and within the atmospheric column (ATM). All data presented are from 2B-FLXHR-LIDAR, 2007–2010.	158
A.2	Monthly mean heat flux from mixed-phase clouds, binned in 20° latitude bands from 80°S to 80°N . Heat flux, reported in units of Terawatts (TW or 10^{12} W), is computed at the top of atmosphere (TOA), surface (SFC), and in atmosphere (ATM). A positive (negative) heat flux represents a net gain (loss) of energy at a given atmospheric level. All data are from R05 2B-FLXHR-LIDAR, 2007–2010.	159

LIST OF FIGURES

Figure		Page
1.1	Aerosols exist over a range of sizes, shapes, and concentrations. The wide variety of aerosol properties makes it particularly challenging to simulate aerosols in global models.	12
1.2	Aerosols may alter global radiative balance through direct, indirect, and semi-direct effects on radiation (Forster et al., 2007). This study focuses exclusively on evaluating the direct effects of aerosols on shortwave radiation.	13
1.3	Scattering aerosols (e.g. sulfate) in cloud-free air have a negative aerosol direct effect, or cooling effect, at the top-of-atmosphere. However, the aerosol direct effect is negligible for scattering aerosols above an optically thick cloud.	14
1.4	Absorbing aerosols (e.g. black carbon) over underlying bright surfaces and clouds have a positive aerosol direct effect, or warming effect, at the top-of-atmosphere. However, the top-of-atmosphere aerosol direct effect is negative for absorbing aerosols in cloud-free air.	15
1.5	The cooling from aerosol radiative forcing partially offsets the warming contributed from greenhouse gas radiative forcing (Myhre et al., 2013). However, the broader distribution from aerosol radiative forcing indicates a greater uncertainty in our understanding of aerosol processes that limits our confidence in estimates of the total anthropogenic radiative forcing.	16
3.1	NASA’s A-Train constellation of satellites monitor Earth’s climate using a suite of nearly simultaneous, collocated spaceborne sensors.	48
3.2	A general flowchart of the CloudSat 2B-FLXHR-LIDAR algorithm.	49
3.3	Annual mean land-ocean masks used in the 2B-FLXHR-LIDAR dataset are based on surface classifications from the International Geosphere-Biosphere Programme (IGBP).	50
3.4	Comparisons of annual mean top-of-atmosphere (TOA) albedo from R05 2B-FLXHR-LIDAR, R04 2B-FLXHR-LIDAR, and CERES SSF over 2007–2010. Values displayed in the top right of all maps are area-weighted global averages.	51
3.5	Same as Figure 3.4 but for outgoing longwave radiation (OLR).	52
3.6	Scatterplots of outgoing shortwave (OSR) and longwave radiation (OLR), in $W m^{-2}$, comparing R05 2B-FLXHR-LIDAR to CERES. Each point represents a $2.5^{\circ} \times 2.5^{\circ}$ latitude-longitude grid box of fluxes averaged over 2007–2010.	53

4.1	Maps of annual mean DRE from 2B-FLXHR-LIDAR, as partitioned by sky conditions. The global mean and uncertainty are displayed in the top-right corner of each panel.	79
4.2	Maps of annual mean AOD (a) observed by CALIPSO and (b) simulated in CESM1(CAM5). The global mean is displayed in the top-right corner of each panel.	80
4.3	Annual mean all-sky DRE and total cloud fraction from (left) 2B-FLXHR-LIDAR and (right) CESM1(CAM5) datasets. Note that brighter shading corresponds to higher cloud fraction. The global mean is displayed in the top-right corner of each panel.	81
4.4	Observed and simulated probability density functions of the global (a) ocean-only all-sky DRE and (b) sample counts expressed as a function of cloud fraction. Estimates of monthly mean DRE and cloud fraction are evaluated at 2.5° resolution over a 5-year time period for both 2B-FLXHR-LIDAR (2006-2011) and CESM1(CAM5) (2000-2005).	82
4.5	Maps of annual mean AOD over the southeastern Pacific Ocean (35°-5°S, 130°-65°W) as separated by CALIPSO aerosol types. The area-weighted mean is displayed in the top-right corner of each panel.	83
4.6	Annual mean DRE and low cloud fraction over the southeastern Pacific Ocean (35°-5°S, 130°-65°W) from (left column) 2B-FLXHR-LIDAR and (right column) CESM1(CAM5) datasets. Note than brighter shading corresponds to higher cloud fraction. Low clouds are defined as those with cloud-top temperatures above 0°C. The area-weighted mean is displayed in the top-right corner of each panel.	84
4.7	Maps of annual mean CALIPSO AOD over the southeastern Atlantic Ocean (25°S-0°, 10°W-30°E) as partitioned by CALIPSO aerosol types. The area-weighted mean is displayed in the top-right corner of each panel.	85
4.8	Maps of seasonal mean DRE over the southeastern Atlantic Ocean (25°S-0°, 10°W-30°E) from (top) 2B-FLXHR-LIDAR and (bottom) CESM1(CAM5) datasets. The area-weighted mean is displayed in the top-right corner of each panel.	86
4.9	Cumulative density functions of seasonal mean DRE in the southeastern Atlantic Ocean (25°S-0°, 10°W-30°E) as sorted by sky conditions from the 2B-FLXHR-LIDAR dataset. The beige shading shows the spread within one standard deviation of the median.	87
4.10	Monthly mean (a) all-sky DRE, (b) low cloud fraction, and (c) AOD over the southeastern Atlantic Ocean (25°S-0°, 10°W-30°E) from the 2B-FLXHR-LIDAR (blue) and CESM1(CAM5) (red) datasets. The JJA period is shaded in beige to highlight the onset of the biomass burning season.	88

- 5.1 Time series of monthly mean (top) 2B-FLXHR-LIDAR DRE and (bottom) CALIPSO AOD over the SE Atlantic from 2007-2010. The aerosol optical depth is separated by various aerosol types (marine=blue, dust=red, polluted continental=yellow, polluted dust=green, smoke=gray). During September, shown in beige, positive DRE values are coincident with high values of smoke AOD. 101
- 5.2 A 3D view of annual mean (a) 2B-FLXHR-LIDAR aerosol heating rates, (b) 2B-FLXHR-LIDAR smoke aerosol heating rate, (c) MERRA vertical velocity, and (d) MERRA boundary layer height. 102
- 5.3 A 3D view by height of aerosol heating rate (in Kelvin per day) and cloud fraction during September. Low-lying marine clouds (at an altitude of 1 km) provide the environmental conditions necessary for aerosol solar heating over the Atlantic Ocean. 103
- 5.4 Estimated uncertainty in 2B-FLXHR-LIDAR aerosol shortwave heating rate (in K/day). Uncertainty is computed by perturbing radiative fluxes over a range of possible values of single scattering albedo. 104
- 5.5 Vertical velocity profiles over the southeast Atlantic Ocean (0°S-20°S, 10°W-10°E) from (blue) MERRA reanalysis, (red) 2B-FLXHR-LIDAR aerosol heating, and (black) the combination of both. While the vertical velocity from aerosols is strongest during September, it is still considerably weaker than the predominant subsidence observed over this region. 105
- 5.6 Areal extent of aerosol heating rate greater than 0.05 K/day from 2B-FLXHR-LIDAR. The largest extent of heating over the southeast Atlantic Ocean is during September, followed by Sept-Nov, and then on annual timescales. 106
- 5.7 Vertical profiles of an A-Train overpass over the tropical Atlantic Ocean (5°N-20°S). The (top) scene classification shows the CloudSat/CALIPSO cloud mask and CALIPSO aerosol types. The (middle) aerosol heating rate from 2B-FLXHR-LIDAR. The (bottom) aerosol vertical velocity from 2B-FLXHR-LIDAR is an estimate of vertical motion of aerosol layer due to diabatic heating. 107
- 5.8 Regional maps of the (left) clear-sky and (right) cloudy-sky column-integrated aerosol absorption in SON from 2B-FLXHR-LIDAR. Aerosol absorption is nearly 50% stronger in cloudy scenes because of absorption of reflected solar radiation due to the presence of underlying clouds. 108
- 5.9 (from Boers et al., 2010) Simulated height gain of an aerosol layer in a period of 24 hours due to solar absorption. For an aerosol layer with SSA = 0.75, $\alpha = 1.50$ 109

5.10	(from Zuidema et al., 2016) Biomass burning aerosols from fires over central Africa are transported over marine clouds in the southeast Atlantic Ocean. The aerosol optical depth (warm colors), fire count (green to red), and cloud fraction (contoured in blue) are shown.	110
6.1	Schematic illustrating an idealized size distribution of aerosols. Shortwave effects tend to strongest for aerosols in the accumulation mode, in which particle diameter is comparable to the wavelengths of visible light according to Mie theory. Image courtesy of Jim Davies (LBNL).	124
6.2	Plots of (left) single scattering albedo and (right) asymmetry factor in the shortwave for various aerosol components. The aerosol optical properties are computed according to Mie theory in the Optical Properties of Aerosols and Clouds (OPAC) dataset (Hess et al., 1998).	125
6.3	Probability density functions of all-sky DRE for selected regions. The shape of each function gives information about the relative likelihood of that value of DRE observed by 2B-FLXHR-LIDAR. A broad distribution indicates a large variability in aerosol radiative effects, whereas a narrow distribution suggests relatively little variability.	126
6.4	(from Myhre et al., 2013) AeroCom II model mean (left) aerosol DRF and (right) standard deviation. AeroCom II is an intercomparison of a large set of global aerosol models including an extensive evaluation against measurements and is used in the best estimate of DRF reported by the IPCC AR5.	127
6.5	Aerosol direct radiative effects of shortwave, longwave, and net radiation are computed using 2B-FLXHR-LIDAR, 2007-2010. Global radiative effects at the top-of-atmosphere (TOA), within the atmospheric column (ATM), and at the bottom-of-atmosphere (BOA) are shown.	128
6.6	SPRINTARS global aerosol model simulations provide global estimates of aerosol optical depth for various aerosol species. The (left) pre-industrial AOD, (center) present day AOD, and (right) difference maps between pre-industrial and present day AOD are shown. Emissions inventories are based primarily from the Global Emissions Inventory Activities (GEIA) and atmospheric chemistry prescribed by the CHASER model.	129
6.7	Annual mean aerosol direct radiative effects separated by CALIPSO aerosol types. The capability of CALIPSO to distinguish aerosol layers provides a tool for assessing the contributions of each type to the total radiative impact.	130
6.8	Annual mean aerosol direct radiative forcing separated by CALIPSO aerosol types. The direct radiative forcing is computed using observation-based radiative kernels of aerosol optical depth from 2B-FLXHR-LIDAR.	131

6.9	Radiative kernels on the sensitivity of DRE due to changes in AOD. The radiative kernels are computed using radiative fluxes from 2B-FLXHR-LIDAR and AOD from CALIPSO.	132
6.10	Comparison of global estimates of aerosol direct radiative forcing from (left) AeroCom II and (right) 2B-FLXHR-LIDAR. The AeroCom II multi-model intercomparison study of DRF was used to establish a best estimate of aerosol radiative forcing in the IPCC AR5 (Myhre et al., 2013).	133
6.11	Satellite-based radiative kernels representing the sensitivity of outgoing shortwave radiation in response to change in aerosol optical depth. These kernels are computed using radiative fluxes from 2B-FLXHR-LIDAR and AOD from CALIPSO.	134
6.12	(adapted from Jacobson, 2000). Conceptual illustration of the aerosol mixing states of black carbon and their radiative effects in W/m^2 . While our understanding of aerosol mixing states is still incomplete, it is widely believed that an inorganic coating (i.e. sulfate) on black carbon serves to enhance the absorption efficiency of aged soot aerosol.	135
A.1	(left column) CloudSat/CALIPSO cloud occurrence according to water phase and (right column) the daytime minus nighttime difference in cloud occurrence. Cloud phase is determined based on the 2B-CLDCLASS-LIDAR cloud phase classification. Mixed-phase clouds are defined as single-layer clouds containing multiple phases, whereas multilayered (ML) clouds are assigned if CALIPSO detects cloud layers of more than one phase within a given profile. All data are $2.5^\circ \times 2.5^\circ$ gridded annual averages from 2007 to 2010.	160
A.2	Annual average shortwave, longwave, and net cloud radiative effects at the top of atmosphere (TOA). Radiative effects are separated by water phase (liquid, ice, mixed, and multilayered) using R05 2B-FLXHR-LIDAR, 2007–2010.	161
A.3	Same as Figure 5 but for CRE at the surface.	162
A.4	Same as Figure 5 but for cloud radiative effects in the atmosphere (ATM), defined as the difference between TOA CRE and surface CRE.	163

- A.5 (top row) Zonal mean cloud fraction, (middle row) top of atmosphere cloud radiative effect, and (bottom row) surface cloud radiative effect using CloudSat/CALIPSO observations from 2007 to 2010. The left column distinguishes clouds by water phase (liquid, ice, mixed phase, and multilayered), while the right column separates mixed-phase clouds by season: December–February (DJF) and June–August (JJA). Mixed-phase clouds are defined as single-layer clouds containing multiple phases, whereas multilayered clouds are assigned to scenes with multiple discrete cloud layers of different phases. Gray shading indicates the estimated range of uncertainty in mixed-phase cloud radiative effects, computed in 2B-FLXHR-LIDAR as the flux perturbation under a scenario in which all supercooled liquid is converted to ice. 164
- A.6 Seasonal and annual mean radiative effect of mixed-phase clouds at the TOA. Seasons are defined as December–February (DJF) and June–August (JJA). All data are from R05 2B-FLXHR-LIDAR, 2007–2010. 165
- A.7 Same as Figure 9 but for mixed-phase CRE at the surface. 166
- A.8 Annual mean net radiative effects from mixed-phase clouds binned into 10°-latitude bands. Cloud radiative effects at the TOA and surface are stratified by (left column) convective/non-convective clouds and (right column) precipitating/non-precipitating clouds. All data are from R05 2B-FLXHR-LIDAR, 2007–2010. 167
- A.9 Conceptual illustration of the location of mixed-phase clouds and their influence on global heat transport. Boxed values indicate the contribution of annual heat flux from mixed-phase clouds within the atmosphere and at the surface. Color shading indicates the observed cloud occurrence of liquid (red), ice (blue), and mixed-phase (purple) clouds using cloud phase classification data from 2B-CLDCLASS-LIDAR, 2007–2010. For illustrative purposes, black arrows indicate the general structure of large-scale atmospheric circulations and gray outlines indicate the boundaries of idealized cloud regimes. 168

ABSTRACT

Atmospheric aerosols impact the global energy budget by scattering and absorbing solar radiation. Despite their impacts, aerosols remain a significant source of uncertainty in our ability to predict future climate. Multi-sensor observations from the A-Train satellite constellation provide valuable observational constraints necessary to reduce uncertainties in model simulations of aerosol direct effects. This study will discuss recent efforts to quantify aerosol direct effects globally and regionally using CloudSat's radiative fluxes and heating rates product. Improving upon previous techniques, this approach leverages the capability of CloudSat and CALIPSO to retrieve vertically resolved estimates of cloud and aerosol properties critical for accurately evaluating the radiative impacts of aerosols. We estimate the global annual mean aerosol direct effect to be $-1.9 \pm 0.6 \text{ W/m}^2$, which is in better agreement with previously published estimates from global models than previous satellite-based estimates. Detailed comparisons against a fully coupled simulation of the Community Earth System Model, however, reveal that this agreement on the global annual mean masks large regional discrepancies between modeled and observed estimates of aerosol direct effects related to model biases in cloud cover. A low bias in stratocumulus cloud cover over the southeastern Pacific Ocean, for example, leads to an overestimate of the radiative effects of marine aerosols. Stratocumulus clouds over the southeastern Atlantic Ocean can enhance aerosol absorption by 50% allowing aerosol layers to remain self-lofted in an area of subsidence. Aerosol heating is found to peak at $0.6 \pm 0.3 \text{ K/day}$ at an altitude of 4 km in September when biomass burning reaches a maximum. Finally, the contributions of observed aerosol components are evaluated to estimate the direct radiative forcing of anthropogenic aerosols. Aerosol forcing is computed using satellite-based radiative kernels that describe the sensitivity of shortwave fluxes in response to aerosol optical depth. The direct radiative forcing is estimated to be -0.21 W/m^2 with the largest contributions from pollution that is partially offset by a positive forcing from smoke aerosols. The results from these analyses provide new benchmarks on the global radiative effects of aerosols and offer new insights for improving future assessments.

Chapter 1

Introduction

1.1 Overview of atmospheric aerosols

Aerosols are airborne liquid and/or solid particles suspended in Earth's atmosphere. Typically sized between 1 nanometer and 100 microns, aerosols are small enough to remain suspended in the atmosphere for hours to days. Since aerosols originate from a wide variety of sources, these particles are highly variable in size, shape, concentration, and composition, as shown in Figure 1.1. The production of aerosols may be classified as either primary or secondary. Primary aerosols are particles directly emitted from Earth's surface into the atmosphere, whereas secondary aerosols form within the atmosphere as a result of gas-to-particle reactions with precursor species. Both primary and secondary aerosols derive from a variety of natural and manmade sources.

Natural aerosols (e.g. sea salt, mineral dust, and volcanic ash) typically have a diameter larger than one micron, a distinction commonly referred to as the coarse mode. Manmade, or anthropogenic, aerosols (e.g. sulfate and nitrate) typically have a diameter smaller than one micron that is known as the fine mode. Some particle constituents, including organic and black carbon, may have either natural or anthropogenic (human-caused) origins. Natural aerosols comprise about 90% of all aerosols by mass while the remaining 10% originate from anthropogenic sources (Schulz et al., 2006). Despite their relative scarcity on a global scale, anthropogenic aerosol concentrations tend to predominate locally near regions of heavy industry or agricultural burning.

The concentration of aerosols has increased in recent years over some regions due to changes in land use (such as deforestation, overgrazing, and irrigation practices) and emissions from industrial, residential, commercial, and agricultural sectors. Observed aerosol concentrations are typically largest within the atmospheric boundary layer with concentrations decreasing with altitude in the free troposphere where aerosols are primarily removed from the air through cloud processing and precipitation. The process of wet deposition generally limits aerosol lifetimes in the troposphere to a week or less. However, aerosols from particularly strong volcanic eruptions and wildfires may be

lofted above the tropopause to the stratosphere where their atmospheric lifetimes may be extended to months or years. This distinction is important since the location, duration, and concentration of these particles are significant factors that influence their potential impact on climate.

1.2 Climate impacts of aerosols

Atmospheric aerosols are known to have a profound impact on the climate system by altering the global energy budget. As noted in the IPCC Fifth Assessment Report (AR5) and illustrated in Figure 1.2, there are three pathways by which aerosols may perturb radiative balance: the direct effect, indirect effect, and semi-direct effect. First, the aerosol direct effect is the process in which particles directly interact with solar radiation by scattering and absorbing sunlight. Scattering aerosols cool the atmosphere, whereas absorbing aerosols warm the atmosphere. Most aerosol constituents are observed to have a single scattering albedo greater than 0.9, meaning these particles effectively scatter over 90% of incident light (Ramanathan et al., 2001). The single scattering albedo may be reduced by the presence of aerosol constituents like black carbon that absorb solar radiation and locally heat the atmospheric column. On a global scale, scattering aerosols tend to predominate over absorbing aerosols. This means that the presence of aerosols enhances the overall backscatter of solar radiation to space and leads to a net cooling of the climate system (Ocko et al., 2012).

Second, the aerosol indirect effect describes how particles interact indirectly with radiation by modifying the microphysical properties of clouds. Submicron particles serve as ideal sites onto which water vapor may condense into cloud droplets. Higher concentrations of particles increase the cloud droplet number concentrations while reducing the size of each droplet, under the assumption of constant liquid water path. The result is an increase in cloud albedo described as the first indirect effect (Twomey et al., 1974). A reduction in water droplet size also decreases the efficiency of warm cloud precipitation and increases cloud height. The presence of aerosols can lead to longer-lived clouds, a phenomenon known as the second indirect effect (Albrecht et al., 1989). Through indirect effects, aerosols perturb radiative fluxes not by direct interaction with light, but rather by altering the

microphysical properties of clouds. The net result of direct and indirect aerosol effects is a brightening of Earth's reflectance and, hence, a net cooling of the climate system.

Finally, the aerosol semi-direct effect is the process by which atmospheric heating from absorbing aerosols can reduce cloud cover and liquid water path. The semi-direct effect is a phenomenon in which aerosols directly interact with light to influence cloud properties. Black carbon, found in soot, is an absorbing aerosol that may contribute to the semi-direct effect. The presence of absorbing aerosols near clouds can heat the atmospheric column and promote cloud burn-off. Furthermore, these aerosols may reduce relative humidity and alter tropospheric stability. The result of the semi-direct effect is proposed to affect radiative balance by modifying cloud properties, although the magnitude of the effect is still uncertain.

1.3 Aerosol direct radiative effects

The mechanisms by which aerosols directly interact with radiation are not yet fully understood. The radiative flux imbalances resulting from aerosol-radiation interactions may be quantified to understand the energy exchanges of aerosols within the atmosphere. The direct radiative effect (DRE) is defined as the perturbation of net radiative flux due to the presence of aerosols.

$$DRE = (F^\downarrow - F^\uparrow)_{aero}^{TOA} - (F^\downarrow - F^\uparrow)_{noaero}^{TOA} \quad (1)$$

By convention, a positive DRE at the top-of-atmosphere (TOA) denotes an addition of energy to the earth-atmosphere system (a warming effect), whereas a negative DRE denotes a loss of energy from the earth-atmosphere system (a cooling effect). Aerosols can interact with both shortwave (0.1-4 μm) and longwave (4-50 μm) radiation. However, aerosol effects on longwave radiation tend to be comparatively weaker and considered negligible under most scenarios. Longwave effects have been shown to be non-negligible for heavy aerosol loads at higher altitudes (Zhou et al., 2014), although this scenario is quite rare in Earth's atmosphere. As a result, aerosol direct radiative effects are by convention assessed only for interactions with shortwave radiation.

Although DRE may be evaluated at any level of the atmosphere, from a radiative balance perspective, the two most important levels to consider are the TOA and surface. These levels represent the upper and lower boundaries of the climate system. Also commonly evaluated is aerosol atmospheric heating, which is defined as the difference between DRE at the TOA and surface. In addition to the amount of aerosol present, the direct radiative effect is highly dependent on single scattering albedo (SSA or ω), which represents the ratio of scattering to total extinction. Whereas sulfate and sea salt aerosols (SSA \approx 1.0 at 0.5 μm) are mostly scattering in the visible spectrum, black carbon aerosols (SSA \approx 0.2 at 0.5 μm) are considerably more absorbing (Ramanathan et al., 2001). Nearly all aerosols are composed not of a single species, but rather an amalgamated mixture of several constituents with highly variable optical properties.

Biomass burning aerosols, composed of black carbon, organic carbon, and inorganic compounds, have a 0.55 μm SSA between 0.85 and 0.89, based on measurements from the Aerosol Robotic Network (AERONET) (Eck, 2003). Aged biomass burning aerosols are less absorbing with an SSA of 0.91, resulting from the condensation of non-absorbing organic gases on existing aerosol particles (Haywood, 2003). Furthermore, biomass burning aerosols from boreal forests tend to have weaker absorption than biomass burning aerosols produced from tropical fires (Wong and Li, 2002).

Arid regions also contribute aerosols through the emission of dust. Mineral dust aerosols have a 0.67 μm SSA of 0.95 over the Sahara and a 0.67 μm SSA of 0.93 over China, according to AERONET measurements (Dubovik and Holben, 2002; Mikami et al., 2006). Although less absorbing than black carbon, mineral dust is one of the most abundant aerosol species globally, with an anthropogenic contribution ranging between 30 and 50% (Tegen and Fung, 1995). Overall, particles that absorb solar radiation, including those from biomass burning and mineral dust, reduce the effective SSA of aerosols that strongly influences radiative transfer through the atmosphere. In the Northern Hemisphere, measurements from field campaigns and dedicated observing networks show that many aerosols have a SSA between 0.85 and 0.95 (Ramanathan et al., 2001). This is important because aerosols generally exert a net negative DRE when SSA exceeds 0.95, and a net positive DRE when SSA is less than 0.85 (Ramanathan et al., 2001). In this study, particles with an SSA greater than 0.95 are termed scattering aerosols and those with an SSA less than 0.85 are termed

absorbing aerosols. Scattering and absorbing aerosols elicit various responses on radiative heating throughout the atmosphere, as conceptualized in Figures 1.3 and 1.4.

Figure 1.3 shows three scenarios in which solar radiation is modified by the presence of clouds and/or scattering aerosols. In the left panel, bright aerosols overlay a dark ocean surface. Sunlight is reflected off the aerosols back to space. This produces a negative DRE, or cooling, at the TOA and surface. In the center panel, a bright cloud is present over a dark surface. Since no aerosols exist in this scenario, there is no aerosol DRE but the cloud enhances the amount of reflected radiation. In the right panel, we observe bright aerosols over a bright cloud. Since the cloud is brighter than aerosols, there is no flux perturbation due to aerosols. Consequently, there is no aerosol DRE when scattering aerosols are present over bright clouds.

Whereas scattering aerosols are largely responsible for cooling at the TOA, the same does not necessarily hold true for absorbing aerosols. Figure 1.4 shows three scenarios in which solar radiation is modified by the presence of clouds and/or absorbing aerosols. In the left panel, dark aerosols overlay an even darker ocean surface. Only a small fraction of sunlight is reflected off of the aerosols back to space. This produces slight cooling at the TOA, warming within the aerosol layer, and cooling at the surface. In the right panel, dark aerosols overlay a bright cloud. Sunlight is absorbed within the aerosol layer, which reduces the quantity of solar radiation that can be reflected off of the cloud. This scenario produces warming at the TOA, warming within the aerosol layer, and cooling at the surface.

Although aerosol research has been conducted since the 1960's, the role of aerosols in climate was not widely recognized until the early 1990's (Charlson et al., 1992). During this time, aerosols were identified as a critical missing component in global models that were needed to accurately simulate observed temperature trends over the industrial period. Aerosols had been given increased attention in the climate community and were, for the first time, included in global climate models. The inclusion of aerosols in climate models have made it possible to simulate aerosol processes and perform global assessments of aerosol radiative effects. In recent years, improved aerosol datasets from surface, air, and space-based observing platforms have shifted estimates of aerosol radiative effects from largely model-based in IPCC TAR (2001) to increasingly satellite-based in IPCC AR4

(2007) (CCSP, 2009). However, the quantification of aerosol radiative effects has proven challenging for both model-based and satellite-based assessments due to large variations in aerosol compositions, distributions, and lifetimes.

While a flux perturbation by all aerosols is called an *aerosol radiative effect*, a flux perturbation by only anthropogenic aerosols is called an *aerosol radiative forcing*. Averaged globally, aerosol radiative forcing is likely negative and comparable in magnitude to the forcing from anthropogenic greenhouse gases (Forster et al., 2007). In regions with high concentrations of anthropogenic particles, aerosol forcing can be much larger than the global average, and even exceed the magnitude of greenhouse gas forcing (NRC, 2005). However, aerosol forcing is more difficult to quantify than greenhouse gas forcing. Aerosols are more variable in space and time due to the short atmospheric lifetimes of aerosols, the intermittency of aerosol sources, and the complex interactions of aerosols with clouds and precipitation. Due to limited understanding of aerosol properties on global scales, current estimates of aerosol radiative effects remain uncertain.

The U.S. Climate Change Science Program identified three areas necessary for reducing aerosol forcing uncertainties: (i) improving measurement quality and coverage, (ii) achieving effective use of these measurements to constrain models, and (iii) producing a more accurate representation of aerosols and clouds in models (CCSP, 2009). In the past decade, significant efforts have been made to integrate data from a variety of platforms (ground-based networks, ship, aircraft, and satellite) and techniques (in-situ measurement, remote sensing, numerical modeling, and data assimilation). While significant progress is being made, there are still substantial uncertainties associated with aerosol forcing that inhibit informed decisions on climate policy.

One of the greatest challenges in studying aerosol properties is characterizing the large diversity of aerosol sizes, compositions, sources, spatial distributions, and temporal distributions. Over the past two decades, dedicated aerosol field experiments and ground-based networks have provided detailed measurements of aerosol physical, chemical, and optical properties. However, these measurements fail to capture the large spatial and temporal heterogeneity of aerosol distributions essential for estimating aerosol radiative effects on global scales. Satellite remote sensing remains the only means of translating information from localized field measurements in order to characterize aerosol

properties over broad spatial and temporal scales. The most important properties for assessing radiative effects are aerosol optical depth (AOD), single scattering albedo (SSA), and asymmetry parameter. AOD is the column-integrated magnitude of light extinction from aerosols. SSA is the ratio of the scattering coefficient to the extinction coefficient. The asymmetry parameter is the cosine-weighted average of the scattering phase function. Accurate representation of these aerosol optical properties is critical for global assessments of aerosol direct effects.

To date, satellite estimates of aerosol DRE have relied on passive instruments including the Moderate-resolution Imaging Spectroradiometer (MODIS), Multi-angle Imaging Spectroradiometer (MISR), Polarization and Directionality of the Earth's Reflectances (POLDER), Ozone Monitoring Instrument (OMI), and Clouds and the Earth's Radiant Energy System (CERES). While these estimates have provided useful benchmarks for model evaluation, passive sensors are typically only able to retrieve aerosol optical properties under clear-sky conditions. Although some methods have been developed to evaluate DRE over land by integrating satellite and model data, most satellite estimates of DRE currently report values only over ocean. These limitations severely reduce sampling, lead to a clear-sky bias, and introduce systematic error for retrievals sampled in the proximity of clouds. The accuracy of AOD from passive sensors (0.05 to 0.20) is severely compromised compared to that of ground-based sun-photometers (0.01 to 0.02) (Kahn, 2005, Remer et al., 2005). Satellite-based retrievals of aerosol optical properties from passive sensors tend to be most accurate over dark ocean surfaces.

1.4 Significance of research

This study addresses key issues in understanding the radiative effects of aerosols in the climate system through the synthesis of satellite and model analyses. It embraces NASA's goal of using Earth system observations to improve understanding of important processes in the Earth-atmosphere system and improve climate predictability. The results of this study are expected to advance current understanding of aerosol radiative effects and reduce uncertainties in representing these effects in climate models. Dedicated aerosol research over the past two decades has greatly advanced our

understanding of complex aerosol processes. The IPCC AR5 has published estimates of the radiative forcing between 1750 and 2011 for various natural and anthropogenic forcing agents, including aerosol-radiation interactions (Figure 1.5). Despite increased knowledge on aerosol-radiation interactions, there remain significant uncertainties concerning the role of aerosol forcing of the climate system. Currently, the large uncertainty in aerosol radiative forcing (RF) from preindustrial times to the present must be reduced to allow for meaningful projections of future climate.

According to the IPCC AR5, the present-day global average RF is $+2.9 \text{ W m}^{-2}$ (with a 90% confidence interval of 2.6 to 3.2 W m^{-2}) from long-lived greenhouse gases and -1.3 (-2.2 to -0.5 W m^{-2}) from aerosols. This produces a total RF of $+1.6$ (0.6 to 2.4 W m^{-2}), as shown in Figure 1.6. Given an increase in global mean surface temperature of 0.7°C since preindustrial times, the RF response yields a transient climate sensitivity of 0.3 to 1.1°C per W m^{-2} . Many global emission scenarios anticipate a doubling of CO_2 by the second half of the 21st century, which equates to a RF of about 4 W m^{-2} . Therefore, the estimated surface temperature increase due to doubled CO_2 ranges from 1.2 to 4.7°C . This range of uncertainty in projected temperatures is considerably large for climate policy. The largest contribution to the overall uncertainty is aerosol RF, which underscores the need for improved measurements of aerosol radiative properties.

Over the past decade, there has been significant progress in improving aerosol measurements from a variety of observing platforms, including satellite, airborne, and ground-based, and laboratory instrumentation. Each observing platform has strengths and weaknesses for sampling measured quantities. Accurate measurements of aerosol optical properties are critical given the dependence of composition on aerosol-radiation interactions, as shown in Figure 1.7. Laboratory measurements provide highly detailed characterization of aerosols under limited atmospheric conditions. Aircraft and ground-based sampling can accurately measure physical and chemical properties, albeit with limited spatial and temporal coverage. These measurements are often used to better constrain more global evaluations of aerosol properties from GCM simulations and satellite observations.

Satellite observations offer the greatest spatial coverage of aerosol measurements. The wide spatial coverage of satellites provides the data sampling necessary to perform global assessments of aerosol radiative effects from observations. Satellite passive imagers have the capability to retrieve a

near-global distribution of AOD daily over cloud-free and dark surfaces. Active spaceborne sensors, such as CALIPSO lidar shown in Figure 1.8, can retrieve the vertical profile of aerosol properties along the orbital path of the sensor. Despite global coverage, the sampling from satellite observations is often an issue over locations where retrievals are difficult or impossible due to instrument limitations. For this reason, measurements from multiple satellite platforms, often combined with model simulations to fill in the gaps, are synthesized for more comprehensive retrievals of desired aerosol properties.

The coordinated efforts of data integration represent a significant step forward towards advancing the quality of aerosol measurements. Despite limitations inherent in all observational data techniques, the individual strengths of each may be exploited through effective data integration. Complementary sensors from multiple platforms and datasets provide the necessary observational constraints to reduce uncertainties in the retrieval of aerosol properties. High-quality observations improve climate model simulations of aerosol radiative effects. The effective use of advanced instrument platforms, coordinated measurement strategies, and numerical techniques offer important advances toward reducing uncertainties in current estimates of aerosol radiative effects.

Collectively, the sensors aboard the A-Train satellite constellation offer an unprecedented dataset for understanding climate processes including the interactions of atmospheric aerosols with solar and terrestrial radiation. A key advantage of A-Train measurements, and CALIPSO in particular, is the ability to detect aerosols in the presence of clouds. Vertical profiles of aerosol and clouds distributions can be used to compute aerosols radiative properties using a combination of active and passive sensors from the A-Train. Together, these sensors provide the accuracy and spatial coverage necessary for improving global assessments of aerosol radiative effects.

1.5 Research questions

This research approach overcomes previous observational limitations using new multi-sensor aerosol, cloud, precipitation, and radiative flux products from the A-Train satellite constellation. This product, called 2B-FLXHR-LIDAR, features collocated observations from CloudSat, CALIPSO,

MODIS, and AMSR-E, specifically designed to detect the precise location of clouds, aerosols, and precipitation with complementary estimates of water contents, AOD, and precipitation intensity. A combination of active and passive observations has the unique capability of estimating aerosol radiative effects in historically poorly sampled regions including above clouds and land surfaces.

The 2B-FLXHR-LIDAR dataset uses information about aerosol layers retrieved by CALIPSO. It is fair to acknowledge that CALIPSO does have a few limitations for observing aerosols. CALIPSO cannot see the entire Earth at one time. CALIPSO cannot explicitly measure aerosol properties. CALIPSO cannot detect aerosol layers below optically thick clouds. However, CALIPSO has unique observational capabilities that offer several advantages over conventional passive sensors. In particular, CALIPSO has three important advantages:

1. CALIPSO aerosol retrievals can be made over land and cloudy-sky scenes.
2. CALIPSO aerosol retrievals are vertically resolved, as opposed to column-integrated.
3. CALIPSO aerosol layers can be distinguished by aerosol type.

The 2B-FLXHR-LIDAR dataset offers a powerful new tool for investigating and understanding the major players in Earth's radiation budget. This multi-sensor satellite product is designed to take full advantage of the unique capabilities of CALIPSO and other sensors aboard the A-Train constellation. By leveraging the unique capabilities of active remote sensing, it may now be possible to investigate important science questions that have been difficult or impossible to answer previously. This study aims to test the following hypotheses:

1. Biases in modeled cloud cover will lead to errors in assessments of aerosol direct effects.
2. Solar-heated aerosol layers may heat the surrounding air sufficiently to overcome large-scale subsidence and remain self-lofted.
3. Anthropogenic aerosol forcing will have the strongest contribution from aerosols identified by CALIPSO as polluted continental.

The hypotheses presented in this dissertation are specifically designed to leverage the strengths of CloudSat and CALIPSO cloud and aerosol observations, in the context of broader swath AMSR-E and MODIS products, to improve estimates of the direct radiative effects of aerosols on global scales. In addition, these hypotheses investigate the radiative efficiency of aerosols to absorb solar radiation and seek to identify the types of aerosols most significant in modulating fluxes on global and regional scales. By using a new dataset of radiative fluxes derived using observations from A-Train sensors, this study is expected to lead to a better understanding of aerosol processes in the global radiation budget and lead to their improved representation in global climate model simulations.

This dissertation presents research conducted by the author in three separate analyses. The results of these analyses are featured in Chapter 4 (The Influence of Cloud Cover on Aerosol Direct Effects), Chapter 5 (The Self-lofting of Aerosols by Solar Radiative Heating), and Chapter 6 (The Contribution of Direct Radiative Forcing by Aerosol Type). A version of Chapter 4 has been published in a peer-reviewed journal (Matus et al., 2015). Chapter 5 and 6 include ongoing analyses presented with the intention of being published in the near future. Finally, the Appendix (The Role of Cloud Phase in Earth's Radiation Budget) provides additional insights into cloud radiative effects on climate and a comprehensive description of new algorithm updates in the R05 2B-FLXHR-LIDAR product in the context of improving the representation of cloud water phase. The Appendix includes work that has been published in a peer-reviewed journal (Matus and L'Ecuyer, 2017).

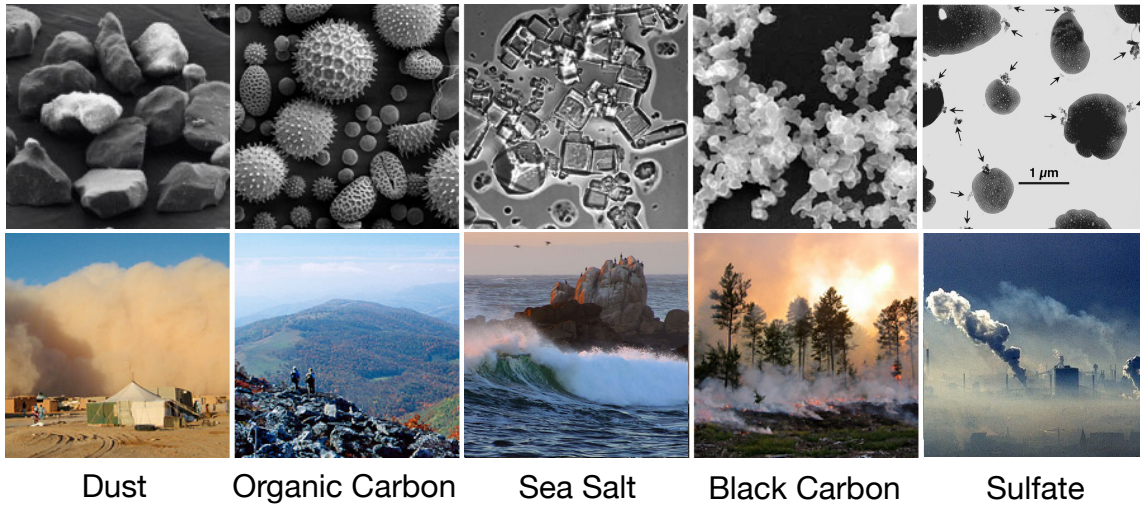


Figure 1.1: Aerosols exist over a range of sizes, shapes, and concentrations. The wide variety of aerosol properties makes it particularly challenging to simulate aerosols in global models.

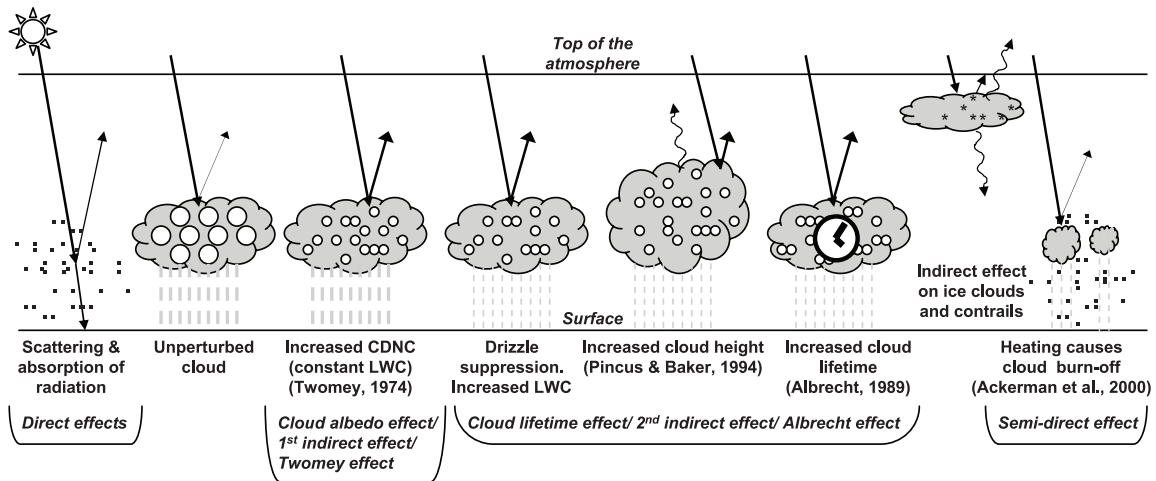


Figure 1.2: Aerosols may alter global radiative balance through direct, indirect, and semi-direct effects on radiation (Forster et al., 2007). This study focuses exclusively on evaluating the direct effects of aerosols on shortwave radiation.

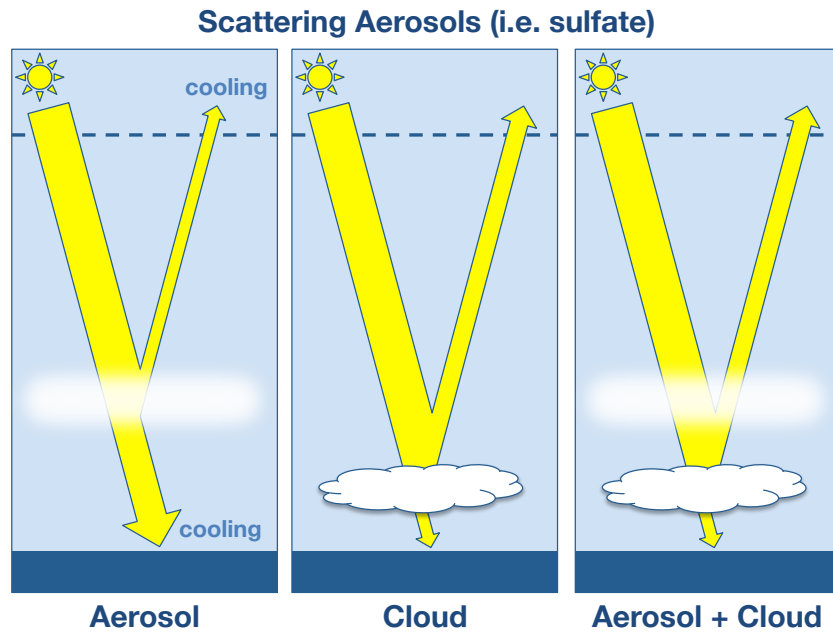


Figure 1.3: Scattering aerosols (e.g. sulfate) in cloud-free air have a negative aerosol direct effect, or cooling effect, at the top-of-atmosphere. However, the aerosol direct effect is negligible for scattering aerosols above an optically thick cloud.

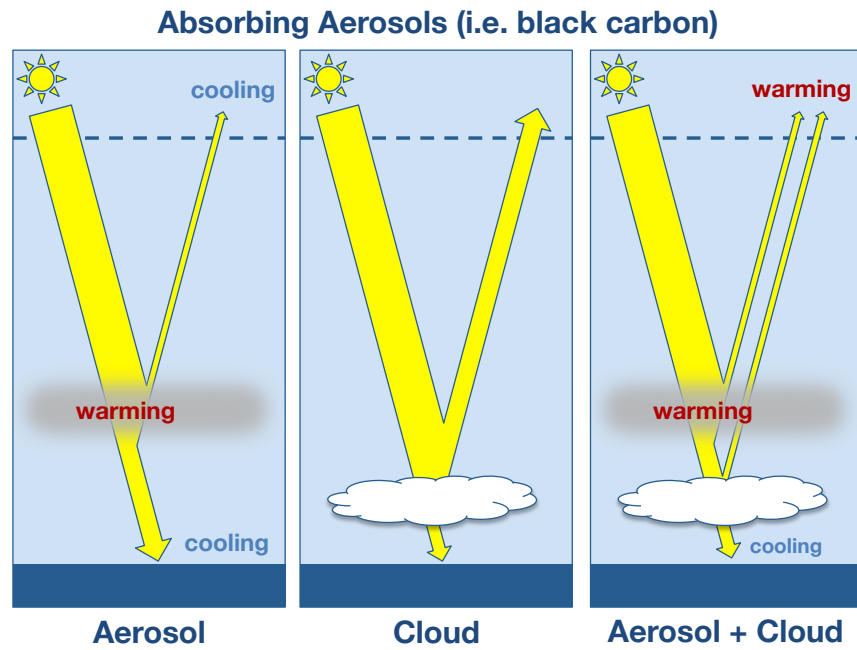


Figure 1.4: Absorbing aerosols (e.g. black carbon) over underlying bright surfaces and clouds have a positive aerosol direct effect, or warming effect, at the top-of-atmosphere. However, the top-of-atmosphere aerosol direct effect is negative for absorbing aerosols in cloud-free air.

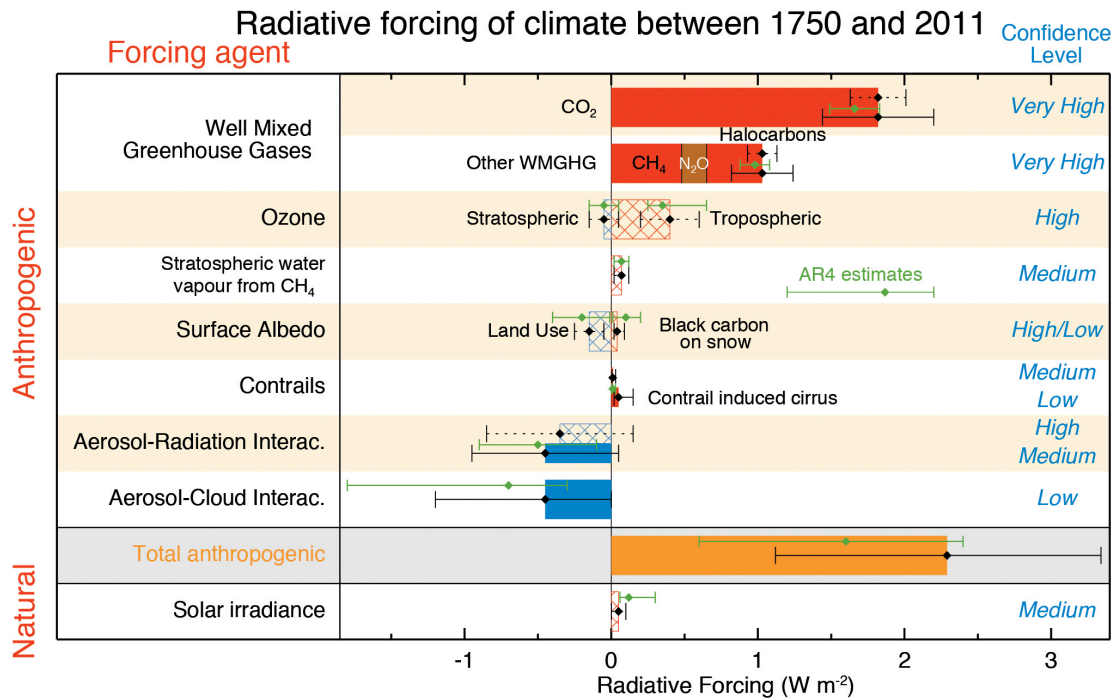


Figure 1.5: The IPCC AR5 estimate of radiative forcing between 1750 and 2011 for natural and anthropogenic forcing agents (Myhre et al., 2013). The forcing agent responsible for the direct radiative effects of aerosols are referred to as aerosol-radiation interactions.

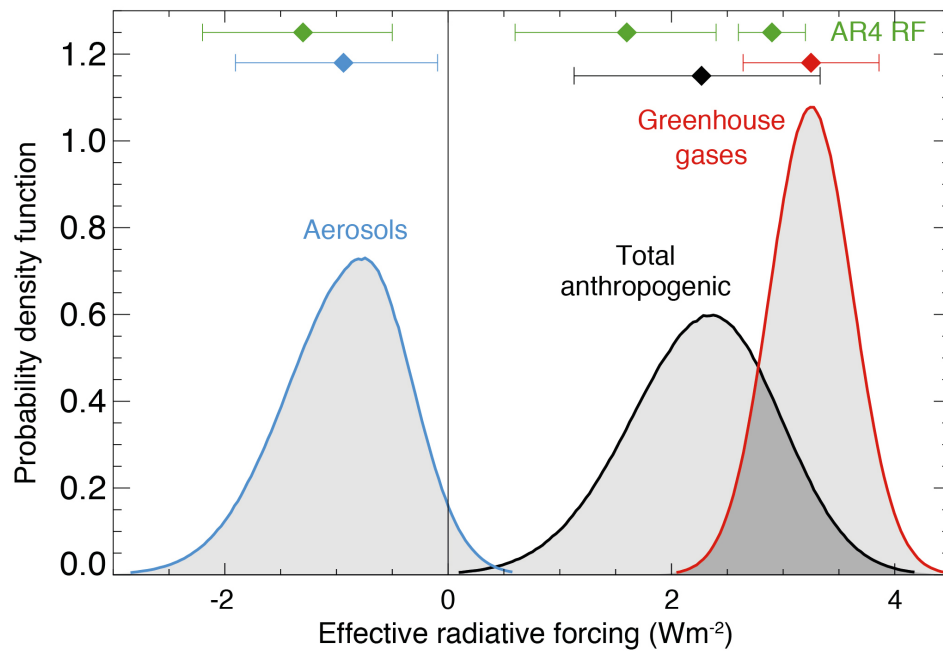
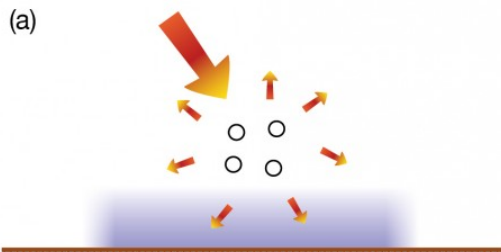


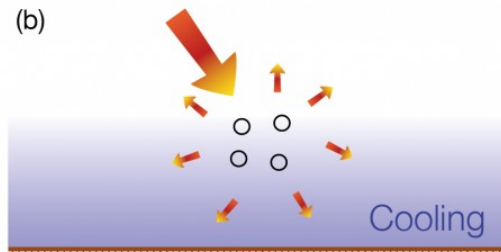
Figure 1.6: The cooling from aerosol radiative forcing partially offsets the warming contributed from greenhouse gas radiative forcing (Myhre et al., 2013). However, the broader distribution from aerosol radiative forcing indicates a greater uncertainty in our understanding of aerosol processes that limits our confidence in estimates of the total anthropogenic radiative forcing.

Aerosol-radiation interactions

Scattering aerosols

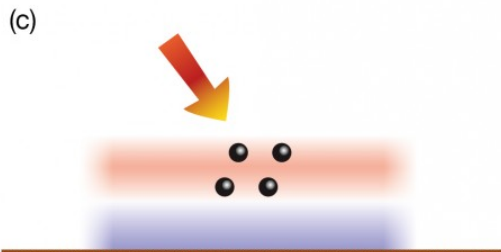


Aerosols scatter solar radiation. Less solar radiation reaches the surface, which leads to a localised cooling.



The atmospheric circulation and mixing processes spread the cooling regionally and in the vertical.

Absorbing aerosols



Aerosols absorb solar radiation. This heats the aerosol layer but the surface, which receives less solar radiation, can cool locally.



At the larger scale there is a net warming of the surface and atmosphere because the atmospheric circulation and mixing processes redistribute the thermal energy.

Figure 1.7: Aerosol-radiation interactions are strongly dependent on the composition of aerosol particles. Scattering aerosols (a, b) produce a localized cooling effect that gradually spreads in the vertical, whereas absorbing aerosols (c, d) have a localized warming effect that eventually redistributes that heat vertically (Myhre et al., 2013).

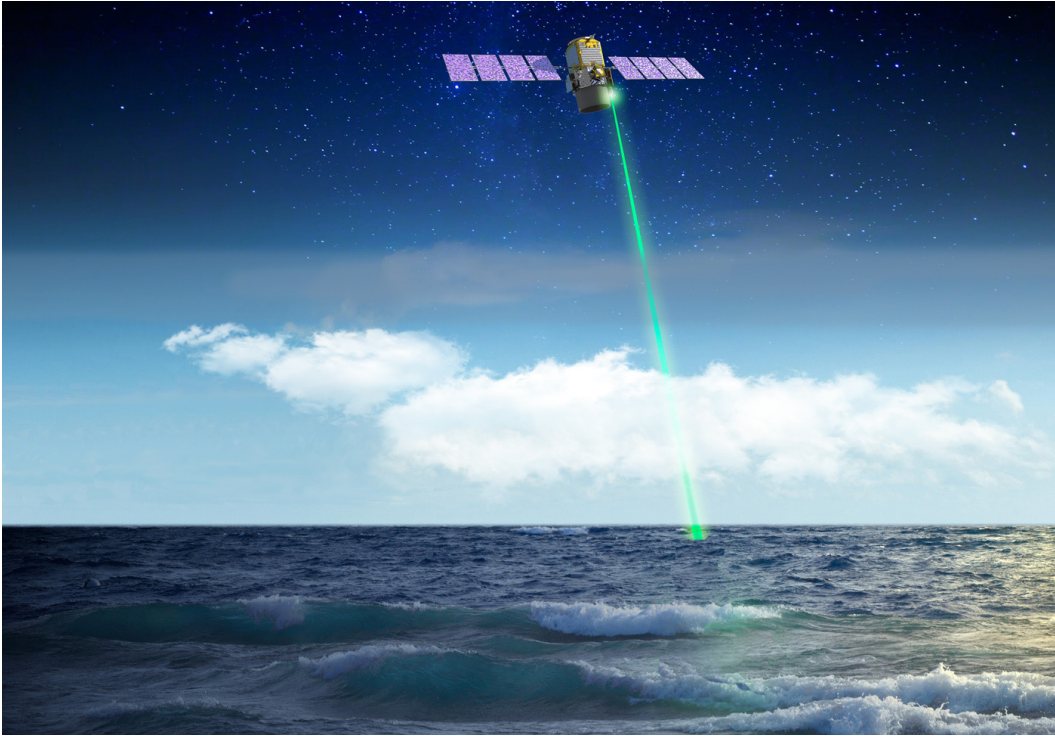


Figure 1.8: Conceptual illustration of CALIPSO lidar retrieving a vertical profile of an aerosol layer over a low level marine cloud (Image courtesy of NASA/Timothy Marvel).

Chapter 2

Previous Assessments of Aerosol Direct Effects

2.2 Overview

As discussed in Chapter 1, one of the greatest challenges in estimating aerosol radiative effects on a global scale arises from the large spatial and temporal heterogeneity of aerosol sizes, shapes, concentrations, and compositions. Accurately characterizing the wide variety of aerosol properties has proven challenging in previous global assessments of aerosol direct effects. Satellite observations, aircraft measurements, or model simulations alone are often inadequate for characterizing the wide diversity of aerosol properties. For this reason, global assessments of DRE tend to require an integrated approach that effectively combines satellite observations and model simulations. As such, satellites are not viewed as a replacement to models but rather a complement.

2.2 Aerosol measurement capabilities

Measurements of aerosol properties provide useful constraints on model simulations of aerosol processes. The accuracy of a measurement needs to be sufficiently high to achieve the desired accuracy for radiative forcing estimates. For example, to obtain an accuracy of 1 W m^{-2} in instantaneous estimates of TOA clear-sky aerosol DRE, the accuracy of measured AOD must be within 0.02 and the accuracy of SSA must be within 0.02 over land (CCSP, 2009). To achieve the same forcing accuracy at the surface, even better sensor accuracy is required. The importance of measurement accuracy highlights the need for high-quality datasets of aerosol optical properties. There currently exist several platforms for measuring aerosol optical properties. These include ground-based networks, field campaigns, and satellite remote sensing. Each measurement technique has advantages and disadvantages. Errors in the measurement of aerosol optical properties can introduce bias to the estimate of the aerosol direct effect, which will be discussed in greater detail later in this chapter.

2.2.1 Ground-based networks

Ground-based networks provide highly accurate measurements of aerosol properties at fixed locations over extended periods of time. The largest ground-based aerosol network in the world is the Aerosol Robotic Network (AERONET). Comprised of over 200 sites globally, AERONET performs high quality measurements of all major tropospheric aerosol regimes using a connected suite of well-calibrated sun photometers and radiometers. Spectral measurements of sun and sky radiance are calibrated and screened for cloud-free conditions (Smirnov et al., 2000). Stations measure spectral AOD at 440, 670, 870, and 1020 nm with an accuracy of ± 0.015 . From the AERONET network, sky-scanning radiometers perform measurements of single scattering albedo with an accuracy of ± 0.03 provided AOD is greater than 0.4 (Smirnov et al., 2000).

AERONET station measurements provide a high-quality climatology of aerosols and their optical properties including optical depth, single scattering albedo, and asymmetry parameter. Data are uniformly acquired and processed at all stations that, in some cases, have been in continuous operation for over 10 years to provide a valuable record of aerosol annual and inter-annual variability. The measurements are complementary to other ground-based aerosol networks with lesser spatial or temporal coverage, including the Department of Energy's Atmospheric Radiation Measurement (ARM) network, NOAA's national SURFace RADiation budget (SURFRAD) network, NASA's Micro Pulse Lidar NETwork (MPL-NET), and the European Aerosol Research Lidar NETwork (EARLINET).

2.2.2 Intensive field campaigns

Field experiments provide the opportunity to combine in situ and remote sensing observations of physical and chemical aerosol properties from a variety of measurement platforms. Ground-based, aircraft, ship, and satellite observations are synthesized over limited spatial and temporal domains to study aerosol processes in exhaustive detail. Field campaigns are typically conducted downwind of known continental aerosol source regions, such as North America, East Asia, and North Africa.

Intensive measurements coupled with model simulations allow field experiments to vastly improve physical and microphysical understanding of regional aerosols in the atmosphere over time periods ranging from weeks to months. Understanding aerosol-cloud-radiation processes over regions of particular interest has been the primary focus of numerous recent field campaigns, including SAFARI-2000, ACE-ASIA 2001, SEAC4RS-2013, and ORACLES-2016.

2.2.3 Satellite remote sensing

Satellite remote sensing remains the only way of characterizing the large spatial and temporal heterogeneities of aerosol optical properties. Space-based monitoring of aerosols has been performed for over two decades. Although originally designed for other purposes, the earliest aerosol sensors provided benchmark studies of global aerosol distributions. These instruments, both launched in 1978, include the Advanced Very High Resolution Radiometer (AVHRR) and the Total Ozone Mapping Spectrometer (TOMS). AVHRR observed radiances in the visible and near infrared wavelengths that could be used to retrieve aerosol properties over the ocean. TOMS, an ozone monitoring sensor, featured UV channels sensitive to aerosol absorption over ocean and land.

More recently, satellites have been launched that were specifically designed for aerosol measurements. These newer sensors have the capability to observe aerosol properties over multiple wavelengths, polarizations, and scattering angles. In addition, advanced cloud screening techniques improve aerosol retrievals in close proximity to clouds. The recent suite of spaceborne passive sensors with aerosol detection capabilities includes MODIS, VIIRS, AHI, ABI, MISR, and CERES. Each sensor features unique measurement capabilities for retrieving aerosol optical properties.

Aboard the Terra and Aqua satellite platforms, MODIS measures radiance in 36 spectral channels in the visible, near infrared, and infrared parts of the spectrum. MODIS aerosol retrievals employ separate algorithms over land and ocean, with greater accuracy for retrievals over ocean. Retrieved aerosol optical depths tend to be overestimated by 10-15% due to contamination of cirrus clouds. MODIS can also derive an aerosol fine-mode fraction, which is the fraction of small particles

in terms of aerosol extinction. On a monthly basis, the MODIS fine-mode fraction agrees with AERONET retrievals over ocean to within 20% (Remer et al., 2005).

MISR aboard Terra measures upwelling shortwave radiances in 4 spectral bands (446, 558, 672, and 866 nm) and at 9 viewing angles in the forward and aft directions along the orbital path (Diner et al., 2002). Its wide range of along-track viewing angles allows for increased accuracy in aerosol retrievals over bright surfaces compared to mono-directional instruments. The accuracy of AOD measurements from both the MODIS and MISR sensors is about 0.05 globally, and slightly improved over dark water (Kahn, 2005, Remer et al., 2005).

Aboard Terra and Aqua, CERES is an instrument that observes broadband shortwave and longwave radiances at three channels. Radiances observed from the radiometer are converted to TOA flux using the Angular Distribution Models (ADM) as a function of sun angle, viewing angle, and scene type (Loeb et al., 2002). CERES retrievals of TOA flux under clear-sky conditions can be compared to the expected flux for an aerosol-free atmosphere to derive the aerosol direct radiative effect over such scenes. Assessments of aerosol direct effects using CERES often require ancillary measurements of AOD from other complementary sensors, such as MODIS or MISR.

2.3 Satellite-based estimates

Global estimates of aerosol direct effects from satellite-based techniques are most effectively achieved through satellite remote sensing. Although observations from ground-based networks and field campaigns may fill in missing data, satellite retrievals ultimately form the foundation for characterizing global aerosol properties. Since aerosol measurements from satellites are typically limited to cloud-free conditions, previous satellite-based estimates focus on clear-sky DRE. To obtain aerosol properties in the shortwave spectrum, satellite sensors often perform retrievals at mid-visible wavelengths, such as 550 nm. Given that aerosol retrievals from passive instruments have traditionally used different algorithms for separating retrievals over ocean versus over land, satellite-based estimates of DRE are separated accordingly.

For context, it is useful to review current estimates of aerosol direct radiative effect published in the literature. In the IPCC AR5, aerosol direct radiative effects are also referred to as aerosol-radiation interactions (RE_{ari}) (Myhre et al., 2007). Table 2.1 presents several satellite-based estimates of annual average DRE at the TOA and surface, using various observational methods from satellite sensors including MODIS, CERES, MISR, and POLDER. Separate results are shown over ocean and land since passive instruments commonly use different aerosol retrieval algorithms for ocean versus land. Satellite-based estimates of the clear-sky ocean DRE ranges from -4 to -6 W m⁻² and is primarily contributed by sea spray (Bellouin et al., 2005; Loeb and Manalo-Smith, 2005; Yu et al., 2006; Myhre et al., 2007). The mean of all estimates yield an annual average DRE over ocean of -5.5 ± 0.7 W m⁻² at the TOA and -8.8 ± 0.7 W m⁻² at the surface, as reported in Yu et al. (2006). Over ocean, the cooling effect at the surface is nearly 60% greater than the cooling effect at the TOA, with the difference attributed to atmospheric absorption by aerosols.

It has been noted that the value of -5.5 ± 0.7 W m⁻² reported by Yu et al. (2006) is likely exaggerated due to sub-pixel cloud contamination from passive observations with large spatial footprints (Chand et al., 2012). Loeb and Manalo-Smith (2005) used MODIS and CERES retrievals to convert clear-sky ocean DRE to all-sky ocean DRE. This technique assumes no contribution to DRE from cloudy regions, which is shown to impact global DRE estimates. Loeb and Manalo-Smith (2005) used MODIS and CERES retrievals to convert clear-sky ocean DRE to all-sky ocean DRE. This technique assumes no contribution to DRE from cloudy regions, which is shown to impact global DRE estimates. Loeb and Manalo-Smith (2005) reported an all-sky ocean DRE of -1.6 to -1.8 W m⁻² that is slightly weaker than the estimate reported in Yu et al. (2006). Nonetheless, there is generally greater confidence in estimates of DRE over ocean than over land surfaces.

Over land, passive satellite sensors traditionally have had difficulty accurately retrieving aerosol measurements especially over surfaces that are reflective in the shortwave and spatially heterogeneous. In general, land is more difficult to characterize in retrievals than ocean. Therefore, DRE estimates over land often rely on filling in missing satellite data with model simulations as well as satellite-model integrations. Averaged annually, satellite-based techniques estimate the clear-sky DRE over land surfaces at -4.9 ± 0.3 W m⁻² at the TOA and -11.7 ± 0.7 W m⁻² at the surface (Yu et

al., 2006). Compared to DRE over ocean, DRE estimates over land are more positive at the TOA and more negative at the surface, suggesting that aerosol absorption over land is stronger than over oceans.

The results published in the IPCC AR5 represent the current state of knowledge on aerosol direct effects. Satellite-based estimates of DRE are most commonly reported under clear-sky conditions owing to the inherent difficulty in retrieving aerosol properties in cloudy scenes. Attempts to estimate aerosol direct radiative effects in the presence of clouds have remained elusive, although now possible using passive and active remote sensing (Torres et al., 2007; Omar et al., 2009; Waquet et al., 2009; de Graaf et al., 2012). The active sensors used in these analyses are either CALIOP or POLDER. Chand et al. (2009) used CALIOP retrievals to estimate a July-October all-sky DRE over the southeast Atlantic Ocean of 2.4 W m^{-2} . Similarly, de Graaf et al. (2012) used POLDER retrievals to estimate a cloudy-sky shortwave-infrared DRE over the southeast Atlantic Ocean of $23 \pm 8 \text{ W m}^{-2}$. While previous studies have performed regional assessments of aerosol direct effects using active sensors, no satellite-based estimates of global all-sky DRE are reported in AR5.

2.4 Model-based estimates

In recent years, there have been significant advances in modeling aerosol direct effects. Many current global climate models (GCMs) now have the capability to estimate aerosol direct radiative effects, with horizontal spatial resolutions often finer than 2° and vertical resolutions of 20 levels or greater. Current global models include effects from most important anthropogenic and natural aerosol species. Some of the more complex models can even account for the evolution of particle size distributions throughout aerosol lifetimes. Internal and external mixing of aerosol components is another feature employed in most newer models (CCSP, 2009). Recent developments in climate modeling have led to significantly more physically realistic simulations of aerosol processes.

Table 2.2 displays several model-based estimates of annual mean aerosol direct radiative effects. Similar to Table 2.1, results are shown over ocean and land as well as at the top-of-atmosphere and at the surface. The ensemble of five GCMs, including GOCART, SPRINTARS, GISS, LMDZ-INCA,

and LMDZ-LOA, yield an annual average DRE over ocean of $3.2 \pm 0.6 \text{ W m}^{-2}$ at the TOA and $-4.9 \pm 0.8 \text{ W m}^{-2}$ at the surface (Yu et al., 2006). Model-based estimates, although weaker than satellite-based estimates, give a surface cooling about 53% greater at the TOA than at the surface.

Since it currently remains challenging to estimate aerosol properties over land from passive measurements, DRE estimates over land generally rely heavily on model simulations. Model-based estimates of annual average DRE over land are $-3.0 \pm 0.6 \text{ W m}^{-2}$ at the TOA and $-7.6 \pm 0.9 \text{ W m}^{-2}$ at the surface (Yu et al., 2006). These values are over 50% less than those reported using satellite-based techniques. Table 2.2 shows that simulations of DRE over land generally produce stronger absorption from dust and smoke aerosols than those observed in satellite-based estimates.

2.5 Reducing uncertainties in estimates

Averaged globally, satellite-based estimates of DRE are 55-80% larger than model-based estimates. On regional scales, the differences between measurements and models can be even greater. In particular, the AeroCom Phase II simulations reported large inter-model discrepancies in aerosol radiative forcing over East Asia and central Africa (Myhre et al., 2013). Such discrepancies likely result from uncertainties in observed and simulated aerosol optical depth, single scattering albedo, surface albedo, as well as differences in radiative transfer schemes (Yu et al., 2006). While optical depth is relatively well-constrained, there are often large uncertainties associated with aerosol single scattering albedo (Loeb and Su, 2010) and the vertical profile (Zarzycki and Bond, 2010). Since MODIS-retrieved AOD tends to be overestimated due to cloud contamination, MODIS-based assessments likely result in comparable overestimates of aerosol DRE (Chand et al., 2012). As for model-based estimates, it is possible that complex aerosol processes (especially in the vicinity of clouds) are not realistically represented in models and could lead to biases in simulated estimates of aerosol direct effects.

Despite much progress in our understanding of aerosols and their radiative impacts, uncertainties still exist in global estimates of DRE from both satellite-based and model-based techniques. The largest discrepancies generally occur in DRE estimates over land and in cloudy skies. Furthermore,

anthropogenic aerosols are often difficult to isolate using current observational techniques. While current global models have the capability to simulate the radiative forcing from anthropogenic aerosols, uncertainties in these assessments still remain as current estimates are poorly constrained by observations. Fortunately, advances in observations of aerosol optical properties through a variety of techniques are continuing to help better constrain aerosol models, reduce outstanding uncertainties, and improve our confidence in assessments of aerosol-radiation interactions.

Active remote sensing of aerosols offers the potential to reduce key uncertainties. In particular, uncertainties in the vertical profile of aerosols can be greatly reduced using spaceborne lidar systems. CALIPSO is currently the best spaceborne lidar available for observing aerosols globally. Yet, like any sensor, there are potential sources of uncertainty. The 16-day repeating orbital configuration of CALIPSO limits retrievals to a twice-daily sampling pattern. Compared to MODIS, CALIPSO retrievals of AOD tend to have a low bias (Redemann et al., 2012). This low bias in AOD may at least partly be attributed to a misclassification of aerosols as clouds (Schuster et al., 2013). As a result, analyses using CALIPSO data may underestimate DRE by 30-50% due to aerosols missed by the sensor (Thorsen and Fu, 2015). These uncertainties are important to consider in global assessments of aerosol radiative effects. As spaceborne sensors and modeling capabilities continue to advance, these uncertainties are expected to be even better constrained in the future assessments.

2.5 Remaining questions

Many assessments of aerosol direct effects using observations from passive spaceborne sensors consider aerosol direct effects under clear-sky conditions only. Over many regions where aerosols are common, it is perfectly reasonable to assume clear-sky conditions. For example, the ability of these sensors to measure aerosols in clear skies has proven valuable over arid deserts where the air is relatively cloud-free and dust aerosols can be prevalent. While there is considerable merit and value in measuring cloud-free radiative fluxes, the inherent limitations of many passive sensors to measure aerosols in cloudy skies inhibit our current global estimates of DRE. Since the magnitude and sign of

aerosol direct effects are highly dependent on clouds, it is critically essential that clouds are adequately represented in global DRE assessments.

Evaluating DRE over land and in cloudy skies requires characterization of the vertical cloud and aerosol distributions. This has proved challenging for both models and observations due to the large errors introduced by incorrect assumptions on the three-dimensional structure of cloud and aerosol fields. The lack of aerosol observations over cloudy-sky conditions ultimately hinders global assessments of aerosol direct effects. What environmental factors influence the radiative efficiency of aerosols? What role do clouds play? How well do we understand aerosol processes over deserts and ice where observations are sparse? Improving measurements of aerosol properties in poorly sampled regions is necessary to reduce uncertainties in current global estimates of DRE.

Products	Ocean		Land	
	TOA	SFC	TOA	SFC
MODIS (Remer and Kaufman, 2006)	-15.9	---	---	---
MODIS_A (Bellouin et al., 2005)	-6.4	-8.4	---	---
CERES_A (Loeb and Manalo-Smith, 2005)	-5.5	---	---	---
CERES_B (Loeb and Manalo-Smith, 2005)	-3.8	---	---	---
CERES_C (Zhang et al., 2005)	-5.3	---	---	---
MODIS_G (Yu et al., 2004)	-5.7	-10.0	-5.5	-13.5
MISR_G (Yu et al., 2004)	-6.5	-11.1	-4.9	-11.8
MO_GO (Yu et al., 2004)	-5.1	-8.8	-4.8	-11.6
MO_MI_G (Yu et al., 2004)	-5.1	-8.7	-4.4	-10.6
POLDER (Boucher and Tanre, 2000)	-5.7	-7.7	---	---
Mean \pm StdDev	-5.5 ± 0.7	-8.7 ± 1.7	-4.9 ± 0.4	-11.9 ± 1.2

Table 2.1: Satellite-based estimates of annual mean DRE (W m^{-2}) at the top-of-atmosphere and surface, as evaluated over ocean and land surfaces separately.

Products	Ocean		Land	
	TOA	SFC	TOA	SFC
GOCART (Chin et al., 2002)	-4.1	-6.9	-4.1	-9.7
SPRINTARS (Takemura and Nakajima, 2002)	-1.6	-2.7	-1.7	-5.1
GISS (Koch et al., 2005)	-3.5	-4.8	-2.8	-7.2
LMDZ-INCA (Balkanski and Schulz, 2007)	-4.7	-5.8	-4.3	-9.2
LMDZ-LOA (Reddy et al., 2005)	-2.3	-4.1	-2.0	-6.9
Mean \pm StdDev	-3.2 \pm 1.3	-4.9 \pm 1.6	-3.0 \pm 1.2	-7.6 \pm 1.9

Table 2.2: Model-based estimates of annual mean DRE (W m^{-2}) at the top-of-atmosphere and surface, as evaluated over ocean and land surfaces separately.

Chapter 3

Data and Methodology

3.1 Overview

Global assessments of aerosol direct radiative effects have been performed in the past using passive satellite sensors, including MODIS, MISR, and CERES. For the first time, these satellites made it possible to observe aerosol effects on a global scale. As assessments of direct effects shifted from model-based to increasingly satellite-based, insights gained from these spaceborne radiometers have led to important breakthroughs in our understanding of the role of aerosols in climate. MODIS, MISR, and CERES have helped to fill many gaps in our knowledge, but there are still unanswered questions due to limitations in our observations. Despite their global spatial coverage, passive sensors are often unable to retrieve aerosol properties over bright land surfaces and in the presence of clouds. In this study, we overcome these barriers using a combination of active and passive sensors from the A-Train satellite constellation. Collocated A-Train measurements can provide observational constraints necessary to overcome previous limitations and improve global assessments of aerosol direct radiative effects.

3.2 The A-Train satellite constellation

The A-Train (or Afternoon Train) is a constellation of five satellites that follow a sun-synchronous orbit at an altitude of 690 km. The satellites cross the equator within a few minutes of each other at around 1:30 am/pm local solar time. The benefit of formation flying is that a large number of observations may be collected at the same location and at the same time. The current satellites in the A-Train include Aura, CloudSat, CALIPSO, and Aqua, as shown in Figure 3.1, as well as GCOM-W1 (not pictured). A-Train satellite observations are used to build high-resolution three-dimensional views of earth's atmosphere and surface. Each satellite features complementary

sensors that together improve our scientific understanding of climate processes. Collectively, the sensors aboard the A-Train satellite constellation offer an unprecedented dataset for assessing the climate impact of aerosols. In this study, we assess the direct radiative effects of aerosols using collocated observations from the CloudSat, CALIPSO, and Aqua platforms.

CloudSat has been actively monitoring cloud properties from space since its launch in April 2006. The main sensor aboard CloudSat is the Cloud Profiling Radar (CPR), a 94-GHz nadir-viewing radar that measures the returned backscattered energy, location, and altitude of clouds and precipitation. CloudSat was designed to profile clouds and their physical properties to improve the way in which clouds are parameterized in global models and, therefore, contribute to improved prediction of weather, climate, and cloud-climate feedbacks.

The Cloud-Aerosol Lidar with Orthogonal Polarization (CALIPSO) was launched, along with CloudSat, from a single Delta II rocket at Vandenberg Air Force Base, California. A joint U.S. (NASA) and French (Centre National d'Etudes Spatiales/CNES) venture, CALIPSO features an active dual-wavelength, dual-polarization lidar used to probe the vertical structure of thin clouds and aerosols in the atmosphere. Lidar profiles from the Cloud-Aerosol Lidar with Orthogonal Polarization (CALIOP) instrument are complemented by infrared radiation measurements from the Imaging Infrared Radiometer (IIR). The CALIPSO satellite provides new insight into the role that clouds and atmospheric aerosols play in regulating weather, climate, and air quality.

The Aqua satellite platform performs global measurements of land, ocean, and atmospheric properties. Data are collected from various sensors to allow scientists to assess global changes, identify their anthropogenic and natural causes, and improve model development for long-term forecasting. The Aqua platform has six sensors including the Moderate Resolution Imaging Spectroradiometer (MODIS). By making radiance measurements of the Earth at 36 spectral bands, MODIS provides valuable observations of surface and atmospheric properties and continues to be an invaluable tool for understanding climate processes. The Advanced Microwave Scanning Radiometer Earth Observing System (AMSR-E), also aboard Aqua, measures terrestrial, oceanic, and atmospheric parameters, including sea ice concentration. Collectively, the instruments aboard the

CloudSat, CALIPSO, and Aqua platforms measure the key variables necessary for assessing global aerosol radiative effects.

3.3 CloudSat's 2B-FLXHR-LIDAR

This study seeks to fill in knowledge gaps in our understanding of aerosol-radiation interactions by leveraging actively sensed cloud profile data from CloudSat and the Cloud-Aerosol Lidar and Infrared Pathfinder Satellite Observation (CALIPSO) in combination with the Moderate Resolution Imaging Spectroradiometer (MODIS). There are several updates in the new release of the CloudSat level 2 radiative fluxes and heating rates algorithm (2B-FLXHR-LIDAR) that include an improved representation of supercooled liquid water clouds, thin ice clouds, and surface albedo. The performance of 2B-FLXHR-LIDAR has been evaluated using collocated SW and LW flux observations from the Clouds and the Earth's Radiant Energy System (CERES) (*Kato et al.*, 2010). Flux estimates from 2B-FLXHR-LIDAR are then used to investigate the radiative impacts of aerosols over the pre-anomaly phase of the CloudSat mission (2007–2010). This time period has been selected since, after the April 2011 battery anomaly, only daytime observations are available, and the alignment of CloudSat and CALIPSO footprints is slightly degraded.

3.3.1 Product description

The 2B-FLXHR-LIDAR data product computes vertically-resolved broadband fluxes consistent with observations from a suite of sensors aboard the A-Train constellation. The product utilizes vertical distributions of liquid and ice cloud effective radii and water contents from CloudSat's Level-2 cloud water content product (2B-CWC). These observations are combined with temperature and humidity profiles from the European Centre for Medium-range Weather Forecasts (ECMWF) analyses as well as surface albedo and emissivity data from the International Geosphere-Biosphere Programme (IGBP) global land surface classification (*Henderson et al.*, 2013). Collectively, these data initialize a broadband radiative flux model, known as BUGSrad, to compute vertical profiles of radiative fluxes and heating rates.

BUGSrad is a two-stream, adding-doubling solution to the radiative transfer equation introduced by Ritter and Geleyn (1992). The radiative transfer model assumes a plane-parallel atmosphere over the 1.4×1.8 km CloudSat field of view. Molecular absorption and scattering is computed using the correlated-k method of Fu and Liou (1992). The delta-Eddington approximation is applied over six shortwave (0-4 μm) bands and a constant hemisphere approximation is applied over twelve longwave (>4 μm) bands. The bands are then weighted and combined into broadband estimates of shortwave and longwave fluxes. Finally, the algorithm computes the pressure derivative of net radiative flux to derive vertical heating rates.

$$QR = \frac{g}{c_p} \frac{\partial F^{net}}{\partial p} \quad (2)$$

The resulting fluxes and heating rates are output for each CloudSat footprint at a vertical resolution of 240 m, forming the 2B-FLXHR data product. The 2B-FLXHR-LIDAR data product used in the current study is the result of several improvements to the existing 2B-FLXHR algorithm (Henderson et al., 2013). L'Ecuyer et al. (2008) showed that thin clouds undetected by CloudSat may lead to significant errors in radiative flux estimates. By including coincident lidar observations from CALIPSO and radiance measurements from MODIS, a method was developed to improve constraints on cloud and aerosol properties in radiative flux calculations.

In a special version of 2B-FLXHR-LIDAR known as ERB (Earth Radiation Budget), the radiative transfer model has been modified to simulate solar position at all possible zenith angles to compute radiative fluxes for both daytime and nighttime satellite retrievals so that the resulting fluxes approximate diurnal averages. Future algorithm development plans include Atmospheric Infrared Sounder (AIRS) temperature and humidity sounding retrievals to reduce the dependence on ECMWF analyses. It is noted that the source of temperature and humidity information has a negligible impact on estimates of aerosol DRE since it is derived from flux differences. The key steps in generating the new 2B-FLXHR-LIDAR data product are summarized in the flowchart illustrated in Figure 3.2. Cloud location is determined based on CloudSat's 2B-GEOPROF-LIDAR product. Cloud properties

are obtained using a combination of CloudSat's 2B-CWC-RO, CloudSat's MODIS-based 2B-TAU, and CALIPSO's Version 3 products. Precipitation location and intensity are identified using CloudSat's 2C-PRECIP-COLUMN product, which retrieves cloud and rain liquid water contents and estimates the vertical extent of liquid precipitation in the column.

Aerosol optical depth is determined based on CALIPSO's Aerosol Layer product. CALIPSO's vertical feature mask (VFM) product is used to determine aerosol species type and vertical distribution. Aerosol optical properties, including single scattering albedo and asymmetry parameter, are retrieved for each aerosol layer using an approach similar to the Spectral Radiation-Transport Model for Aerosol Species (SPRINTARS) global transport model (Takemura and Nakajima, 2002). Retrieved aerosol properties from CALIPSO form critical observational inputs for the 2B-FLXHR-LIDAR algorithm. Using this information as inputs to a radiative transfer model, the 2B-FLXHR-LIDAR algorithm computes upwelling and downwelling SW and LW radiative fluxes at 125 vertical levels. The uppermost level is at an altitude of about 25 km above mean sea level and is treated as the top-of-atmosphere. The lowest level is at the surface. The data product has a vertical resolution of 240 m and a horizontal resolution of 1.5 km, as constrained by the maximum resolution provided by CloudSat observations.

The fifth release (R05) 2B-FLXHR-LIDAR data set makes several significant advances over the previous version (R04) described in Henderson et al. 2013. The new algorithm features improved land, snow, and sea ice albedos using spectral measurements from Zatko and Warren, 2015, a more realistic representation of the zenith angle dependence of ocean albedo, an explicit representation of lidar-detected supercooled liquid water clouds, and a more rigorous treatment of thin ice clouds that includes explicit retrievals of ice water content (IWC) and effective radii from the CloudSat 2C-ICE data product (Deng et al., 2013). These improvements incorporate better physical assumptions and yield better agreement relative to validation data sets. As with any remote sensing-based data set, however, a number of limitations remain including retrieval errors and sampling biases that result from the spatial and temporal sampling characteristics of CloudSat and CALIPSO. While CloudSat is more sensitive to optically thick clouds and CALIPSO is better suited at detecting optically thin clouds, it is likely that some cloud features may go undetected by both sensors. CALIPSO may fail to

detect very thin liquid layers ($LWP < 5 \text{ g m}^{-2}$) and may miss layers in clouds below optically thick ice layers above (Christensen et al., 2013). Since CALIPSO lidar may be attenuated by optically thick supercooled liquid layers which prevents the detection of underlying ice layers, CALIPSO may miss mixed-phase clouds over polar regions where supercooled-topped mixed-phase clouds are common (Morrison et al., 2011; Cesana et al., 2012). The influence of these uncertainties on the results will be evaluated through a combination of sensitivity studies and comparisons against independent top-of-atmosphere (TOA) flux data sets.

The R05 dataset comprises 730 million radiative flux profiles from 20,000 CloudSat orbits with near-global coverage (82.5°S to 82.5°N) from July 2006 to April 2011. Aerosol direct radiative effects are only computed if CALIPSO detects an aerosol layer within a given profile in a subset that comprises 286 million profiles, or 39% of all profiles. For quality control, profiles with incomplete or missing input data are screened using the quality control flags supplied with the product. Data are screened based on the following criteria: missing Cloud-Aerosol Lidar with Orthogonal Polarization (CALIOP) observations, missing MODIS observations, or out-of-bounds flux estimates. The specific criteria are described in greater detail in Table 14 of the CloudSat 2B-FLXHR-LIDAR Data Product Documentation (Henderson and L'Ecuyer, 2011). Altogether, these criteria result in less than 0.3% of the data being excluded from the analysis.

Radiative flux profiles from the 2B-FLXHR-LIDAR dataset are gridded at $2.5^\circ \times 2.5^\circ$ spatial resolution. Given the 16-day repeating cycle of the A-Train satellites, observations in the 2B-FLXHR-LIDAR dataset are well-sampled globally. The global sample density is fairly homogeneous with greatest coverage at the poles. On average, the sample density of all profiles in each 2.5° resolution bin is 74,400. After screening for aerosols using CALIPSO, the sample coverage becomes more spatially heterogeneous with an average sample density for aerosol-detected profiles of 24,900. In general, equatorial regions are generally better sampled especially over predominantly cloud-free areas. Since CALIPSO is unable to detect aerosol layers under optically thick clouds, the sample coverage for aerosol-detected profiles is similar to the global distribution of total cloud fraction. The least well-sampled areas are regions where aerosol layers are less frequently observed, such as Greenland and Antarctica. CALIPSO does not detect aerosols as frequently in these locations and

therefore there are fewer satellite observations in which DRE may be computed. Similarly, there are relatively fewer aerosol observations over the southeast Pacific Ocean, central Africa, Himalayas, and Indonesia, resulting from the high frequency and coverage of clouds.

3.4 Algorithm performance

To evaluate the performance of the 2B-FLXHR-LIDAR flux product, estimates of SW and LW fluxes at the TOA are compared with CERES single scanner footprint (SSF) fluxes reported in the CALIPSO, CloudSat, CERES, and MODIS (C3M) product (Kato et al., 2010). The CERES instrument aboard Aqua provides a long-term, continuous data set of high-quality SW and LW fluxes. Since the Aqua satellite orbits closely with CloudSat and therefore views nearly identical atmospheric conditions, the CERES SSF product is a particularly valuable tool for validating 2B-FLXHR-LIDAR fluxes. Figure 3.4 compares TOA albedo in clear-sky and all-sky scenes from CERES with 2B-FLXHR-LIDAR estimates from both the R04 and R05 versions of the algorithm. It is found that the R04 version of 2B-FLXHR-LIDAR exhibits significant clear-sky biases over most land surfaces and most notably over deserts, forests, and tundra. In the new R05 version, corrections to land and ocean surface reflectances have reduced the global mean bias by over 40% in clear-sky scenes, resulting in a TOA albedo offset of just -0.7% . Regionally, these biases in clear-sky albedo have improved by as much as 20% over Greenland and Antarctic ice sheets, 10% over tropical forests, and 5% over deserts.

All-sky biases have also been reduced in R05 through the improved representation of mixed-phase clouds and thin cirrus. In particular, the positive bias over subtropical ocean has been improved from 4 W m^{-2} in R04 to 1 W m^{-2} in R05, while the negative bias over the Southern Ocean has been improved from -6 W m^{-2} to -2 W m^{-2} , primarily due to the explicit detection of supercooled liquid in the new R05 2B-FLXHR-LIDAR algorithm. The spatial structure of albedo in R05 has improved significantly over the entire globe and especially over polar regions where much attention has been given toward better understanding the surface energy budget (Verlinde et al., 2007; Christensen et

al., 2016). Overall, clear-sky and all-sky albedo estimates compare favorably between CERES and R05, with global annual mean differences less than 1%.

Similar comparisons of outgoing longwave radiation (OLR) are shown in Figure 3.5. There are two significant changes in R05 affecting OLR: (1) updating greenhouse gas concentrations to 2010 levels and (2) including explicit retrievals of IWC and effective radius from 2C-ICE. Increasing carbon dioxide concentrations from 330 ppm in R04 to 390 ppm in R05 results in a global reduction in clear-sky OLR of -1.3 W m^{-2} . This reduction in OLR helps to improve the positive bias observed at higher latitudes. The addition of 2C-ICE retrievals in R05 increases all-sky OLR over the tropics, offsetting a negative bias resulting from increased greenhouse gas concentrations in that region. While all-sky OLR biases have increased slightly to 9 W m^{-2} at higher latitudes, biases are similar to R04 elsewhere and even exhibit a slight improvement over the equatorial Pacific.

Scatter plots, including Root-mean-square (RMS) differences between annual mean fluxes at $2.5^\circ \times 2.5^\circ$ spatial resolution from 2B-FLXHR-LIDAR and CERES are shown in Figure 3.6. The RMS differences in clear-sky outgoing shortwave radiation (OSR) are 7.5 W m^{-2} , while those for OLR are 2.8 W m^{-2} . Higher RMS differences in SW fluxes can be attributed to the larger diurnal range in solar insolation (0 to 450 W m^{-2}) compared to that of thermal emission (200 to 450 W m^{-2}). The RMS differences for all-sky OSR and OLR are 8.9 W m^{-2} and 4.9 W m^{-2} , respectively, which improve upon R04 values of 16.5 W m^{-2} and 5.7 W m^{-2} reported in H13. The larger spread in flux values from all-sky scenes compared to clear-sky scenes is attributed to uncertainties in cloud microphysical property retrievals and cloud detection differences between the larger CERES and smaller CloudSat fields of view. Overall, biases in OSR and OLR are less than 4 W m^{-2} in both clear-sky and all-sky scenes. While R05 generally underestimates TOA fluxes compared to CERES, these differences are consistent with anticipated uncertainties in CERES fluxes themselves (Loeb et al., 2012).

It should be noted that uncertainties in any observational quantity derived from an algorithm like 2B-FLXHR-LIDAR may vary with the time and space scales of interest. Furthermore, due to structural errors from the myriad of assumptions required in the calculations, uncertainties on every scale are a sum of random and systematic components (L'Ecuyer et al., 2015). L'Ecuyer et al. (2008)

showed that uncertainties in fluxes derived from the original 2B-FLXHR algorithm decreased on longer time scales and this also holds true for the current 2B-FLXHR-LIDAR product. Table 3.1 compares fluxes from R05 relative to CERES computed over a range of time and spatial scales. While spatial averaging has a negligible impact for the range of scales considered (2.5 to 10°), the RMS differences in SW and LW fluxes decrease systematically with increasing temporal averaging as a result of reduced random errors. The RMS differences in OSR at 2.5° resolution, for example, decrease from 13.8 W m⁻² for monthly averaging to 8.9 W m⁻² for annual averaging. For LW fluxes, though, the change in RMSE from monthly to annual averaging is considerably less than that for SW fluxes. This highlights the importance of considering time-space scale averaging when interpreting 2B-FLXHR-LIDAR analyses of SW and LW fluxes.

While many approaches of varying complexity have been introduced for classifying clouds, we adopt an approach that simply partitions clouds according to phase. This approach not only avoids the use of subjective thresholds but also relates more directly to prognostic fields in numerical models, potentially offering a more direct means of evaluating their representation in models. The new R05 2B-FLXHR-LIDAR algorithm features a robust cloud phase classification, improving upon previous versions that assumed a linear partitioning of liquid and ice water in cloud layers with temperatures between -20°C and 0°C (L'Ecuyer et al., 2008). The R05 2B-FLXHR-LIDAR algorithm explicitly identifies cloud phase (liquid, ice, or mixed) in each layer of a scene using the 2B-CLDCLASS-LIDAR cloud phase classification described in Sassen and Wang (2012). The 2B-CLDCLASS-LIDAR product combines CloudSat radar and CALIPSO lidar measurements to distinguish cloud phase using signal intensity differences between liquid and ice particles. While CloudSat's Cloud Profiling Radar is particularly sensitive to cloud liquid droplets, CALIPSO's CALIOP has a greater sensitivity to smaller ice particles. Together, both radar and lidar measurements improve overall cloud detection and provide information necessary for cloud phase classification in the 2B-CLDCLASS-LIDAR product. In this study, a mixed-phase cloud refers to any contiguous cloud layer in which both liquid and ice phases are identified according to the 2B-CLDCLASS-LIDAR cloud phase classification. If more than one cloud phase is identified in multiple distinct cloud layers, then that scene is classified as a multilayered (ML) cloud system.

Table 3.2 summarizes comparisons of 2B-FLXHR-LIDAR and CERES fluxes categorized by scene type. Biases and RMS differences are reported as percent differences relative to CERES. Overall, clear-sky fluxes exhibit good agreement between 2B-FLXHR-LIDAR and CERES with a net bias and RMSE of less than -0.9% and 2.8% , respectively. Fluxes in cloudy scenes have slightly higher biases and spreads that can be attributed to cloud retrieval and detection differences in CERES and CloudSat/CALIPSO. In particular, the 20 km CERES scanner footprint is considerably larger than CloudSat's cross-track resolution of 1.4 km. Owing to sampling issues discussed previously, cloudy-sky fluxes exhibit better agreement in the longwave than in the shortwave. Scenes with liquid phase clouds have a relatively low RMS of 2.2% for OLR fluxes but a higher RMS of 16.9% for OSR. This may be partially explained by differences in the fields of view of CloudSat and CERES, particularly over spatially heterogeneous clouds such as broken stratocumulus. By comparison, scenes with mixed-phase clouds have RMS differences of 8.4% and 12.7% in OLR and OSR, respectively. Given that the level of agreement in SW and LW fluxes varies by the type of cloud present in a given scene, it is important to consider the scene type when assessing the accuracy of fluxes from 2B-FLXHR-LIDAR.

3.4 Community Earth System Model (CESM)

In general, satellite retrievals of atmospheric properties provide valuable observational constraints for improving global model simulations of climate processes. In an effort to use the 2B-FLXHR-LIDAR dataset to validate model performance, 2B-FLXHR-LIDAR estimates of direct radiative effect are compared against a widely-used global climate model known as the Community Earth System Model (CESM). An improved accuracy in model simulations of DRE will continue to reduce uncertainties and improve global estimates of aerosol radiative effects on future climate. CESM is a fully-coupled general circulation model (GCM) that provides state-of-the-art computer representations of Earth's past, present, and future climate. Maintained by the Climate and Global Dynamics Division (CGD) at the National Center for Atmospheric Research (NCAR), CESM comprises five geophysical component models simultaneously simulating earth's atmosphere, ocean,

land surface, sea ice, and land ice. All five models communicate using a central coupler component in a fully-coupled model environment. The coupling infrastructure of CESM provides the ability to use a single code base in a complete development cycle to optimize global simulations over various model configurations and resolutions (Worley and Craig, 2011).

The present study analyzes model output from a fully coupled CESM1(CAM5) ensemble member (denoted as b.e10.B20TRC5CN.f09_g16.001) simulated at 1° spatial resolution. Simulated estimates of monthly mean DRE are analyzed over the time period of 2000–2005, which represents a subset of the full simulation that runs from 1850 to 2005. Although the specific time periods differ between the model and observations, this difference has a limited effect on the results since interannual variability in DRE is sufficiently small (less than $\pm 0.03 \text{ W m}^{-2}$ between both datasets) compared to discrepancies between observed and simulated DRE. Physical atmospheric processes are represented using Version 5.1 of the Community Atmosphere Model (CAM5). This version of CAM offers several improvements over its predecessor, CAM4, including an enhanced treatment of stratus-radiation-turbulence interactions, shallow convection, and stratiform microphysics. The CAM5 atmospheric model simulation invokes the three-mode prognostic Modal Aerosol Model (MAM) scheme and the Rapid Radiative Transfer Model (RRTMG) radiation scheme, which features a similar set of distinct radiation calculations as those employed in the 2B-FLXHR-LIDAR algorithm (Worley and Craig, 2011).

3.5 Methodology

The 2B-FLXHR-LIDAR dataset computes vertical profiles of radiative flux, but does not explicitly perform calculations of aerosol DRE. To compute DRE, it is necessary to difference the net flux (downwelling minus upwelling) computed with aerosols present from an alternate net flux computed without aerosols present. Since this method employs a radiative transfer model to calculate radiative fluxes, conditions can be simulated for an aerosol-free atmosphere by setting all aerosol inputs to zero. The standard 2B-FLXHR-LIDAR algorithm has been configured to perform these calculations and include the results in the output so that aerosol DRE may be calculated. The 2B-

FLXHR-LIDAR dataset comprises near-global (82 S to 82 N) observations of profiles from July 2006 to April 2011. Data are screened based on the quality control flags included in the dataset that test for the following criteria: high uncertainty or missing cloud water content (CWC), missing 2B-TAU data, missing CALIOP, missing MODIS data mapped to CloudSat profiles (MODIS-AUX), missing AMSR-E data mapped to CloudSat profiles (AMSR-AUX), or out-of-bounds flux observations. The specific criteria are described in greater detail in Table 14 of the CloudSat 2B-FLXHR-LIDAR data product documentation (Henderson and L'Ecuyer 2011). The 2B-FLXHR-LIDAR algorithm accounts for land and ocean reflectance characteristics using surface albedo and emissivity data from the IGBP global surface classification, derived from a suite of observational MODIS products aboard the Terra and Aqua platforms. Land cover classification data are gridded at 2.5° spatial resolution to produce high-quality seasonal and annual global composites of 17 land cover types (Moody et al. 2005). The surface of each 2B-FLXHR-LIDAR footprint is categorized as land or ocean. Since the shortwave albedo of sea ice is more representative of land rather than ocean, we group all pixels detecting land or sea ice in one category. Based on this classification, Earth's surface is 56% open ocean and 44% non-ocean (i.e., land or sea ice) averaged globally.

A special version of 2B-FLXHR-LIDAR has been developed specifically for investigating energy exchanges in the global climate system. In the Earth Radiation Budget (ERB) version of the 2B-FLXHR-LIDAR data product, radiative fluxes are calculated over 12 solar zenith angles to simulate solar position throughout a 24-hour period. The use of artificial solar zenith angles allows radiative fluxes to be for all CloudSat profiles, including profiles during nighttime conditions. Such an approach is advantageous for studying Earth's radiation budget. To reduce data variability caused by the diurnal cycle of solar insolation, a 12-pixel moving average is performed over all profiles within the dataset. Applying this moving average to the 2B-FLXHR-LIDAR dataset maintains results consistent with diurnally-averaged radiative fluxes.

For quality control, all profiles that include bad or missing input data are removed from the dataset. Data are screened based on the following criteria: bad surface bin, high uncertainty in cloud water content (CWC), missing CWC, missing 2B-Tau data product, missing CALIOP, missing MODIS-AUX, missing AMSR-AUX, or out-of-bounds flux observations. Properly screening data is

necessary to ensure high standards of data quality in retrievals of radiative fluxes in the 2B-FLXHR-LIDAR dataset. The criteria are described in greater detail in Table 14 of the CloudSat 2B-FLXHR-LIDAR Data Product Documentation (Henderson and L'Ecuyer, 2011).

Data are available for every CloudSat overpass in which input fields satisfy quality control. The five-year dataset features observations of nearly every location on the planet, including a wide range of environmental variability. The near-global coverage of the A-Train is important because aerosol direct effects largely depend on the environmental conditions in which aerosols reside in the atmosphere, including surface type (i.e. land and ocean) and sky conditions (i.e. clear-sky and cloudy-sky). To gain insight into the environmental factors that influence aerosol direct effects, DRE observations are categorized based on surface type and sky conditions.

3.5.1 Classifying surface types

The magnitude and sign of aerosol direct effects are dependent not only on the optical properties of the aerosol layer, but also the reflectivity of the underlying surface. Bright surfaces reflective in the shortwave serve to enhance atmospheric warming from absorbing aerosols, whereas dark surfaces absorbing in the shortwave serve to enhance cooling from scattering aerosols. As an example, consider satellite imagery of the Earth. As seen from space, oceans are uniformly dark in the visible spectrum. Conversely, land surfaces are often inhomogeneous and can be much more reflective, which can greatly alter the direct radiative effect exerted by aerosols.

Accurate assessment of aerosol direct effects requires knowledge of surface reflectance in the shortwave spectrum. In particular, there are important differences in the shortwave reflectance properties of land and ocean that need to be accounted for in radiation calculations. The 2B-FLXHR-LIDAR algorithm accounts for land and ocean reflectance characteristics using surface albedo and emissivity data from the International Geosphere-Biosphere (IGBP) global surface classification. Global land cover classification is derived from a suite of observational MODIS products aboard the Terra and Aqua platforms. Data are then synthesized to produce a high-quality annual global composite of 17 land cover types (Moody et al., 2005).

In this analysis, all surfaces on Earth are grouped into one of three categories: *land*, *ocean*, or *margin*. The combination of these three categories yields *global* coverage. For seasonal analyses, global surface maps are averaged over seasonal time periods: December to February (DJF), March to May (MAM), June to August (JJA), and September to November (SON). For annual analyses, global surface maps from the IGBP are averaged over the full year. The land-ocean masks used in the current analysis are shown in Figure 3.3. As shown in these maps, profiles that are not consistently (over 90%) land or ocean are assigned to a separate category called *margin*. Surfaces that satisfy the criteria of *margin* include coastlines and seasonally-transient sea ice. Averaged annually, the surface of the earth is classified as 31% land, 52% ocean, and 17% margin. As a result, due to the presence of marginal surfaces the combined area of land and ocean is not representative of global coverage.

3.5.2 Classifying sky types

Since aerosols interact with reflected sunlight from the Earth's surface, it follows that aerosols also interact with reflected sunlight from clouds. The radiative interactions between aerosols and clouds are important to consider in the computation of aerosol direct radiative effects. Cloud type, height, and location are all critical factors that may influence the radiative effect exerted by aerosols. Similar to a bright surface, a bright cloud enhances atmospheric heating from absorbing aerosols. Alternatively, a bright cloud may nullify the cooling imposed otherwise by scattering aerosols. Therefore, knowledge of both cloud and aerosol fields is necessary to accurately compute the radiative impacts of aerosols on climate.

To better understand the role of cloud cover, this analysis makes the distinction between clear-sky or cloudy-sky scenes in satellite overpasses. Clear-sky conditions are assessed if both CloudSat and CALIPSO do not detect clouds or precipitation, whereas cloudy-sky conditions are assessed if either CloudSat or CALIPSO detects a cloud. Cloudy-sky conditions cover a wide range of cloud types, from optically thin to optically thick. Since cirrus clouds are often optically transparent to visible radiation, aerosol direct effects are similar to clear-sky conditions when cirrus clouds are present. Cloudy-sky conditions are categorized by cloud type: *cirrus* or *other clouds*. Cirrus is

identified if CALIPSO detects a single cloud layer above 440 mb. For all profiles in which clouds and/or precipitation are detected by CALIPSO or CloudSat, the scene is labeled as other clouds. A 12-pixel moving average is applied to all profiles in the dataset. If a profile is not consistently (over 80%) clear-sky, cloudy-sky (cirrus), or cloudy-sky (other clouds), it is labeled as *mixed-sky*.

Overall, this research approach has been designed to leverage aerosol measurements from a suite of A-Train sensors. While global models provide excellent aerosol simulations that have advanced our understanding of aerosol processes in climate, there are still remaining questions in the field that may only be addressed through better observations. Improved measurements of aerosol optical properties provide valuable observational constraints for model simulations of aerosol direct effects. Whereas many previous studies have focused entirely on global estimates of DRE, this study also investigates regional variability over areas where aerosols impacts are significant. By discriminating DRE by surface and sky conditions, further insight may be gained into the complex role of aerosols in Earth's radiation budget.

Flux	Resolution	Month	Season	Year
OSR	2.5	-2.4 (13.8)	-2.1 (11.7)	-2.0 (8.9)
	5	-2.4 (13.6)	-2.1 (11.5)	-2.1 (8.7)
	10	-2.4 (13.7)	-2.1 (11.7)	-2.1 (8.9)
OLR	2.5	-3.7 (5.9)	-3.7 (5.4)	-3.7 (4.9)
	5	-3.6 (5.9)	-3.7 (5.4)	-3.6 (4.8)
	10	-3.6 (5.9)	-3.7 (5.3)	-3.6 (4.8)

Table 3.1: The bias and RMSE (in parentheses) of fluxes, in W m^{-2} , from R05 2B-FLXHR-LIDAR relative to CERES averaged over a range of time and spatial scales.

Scene type	OSR		OSR		OSR	
	Bias	RMSD	Bias	RMSD	Bias	RMSD
Liquid phase	5.1	16.9	-1.6	2.2	0.5	4.6
Ice phase	-7.1	14.3	-2.4	4.2	-3.9	5.4
Mixed-phase	7.0	12.7	-7.3	8.4	-1.2	4.3
Multi-layered	0.5	9.7	-1.7	2.6	-0.9	3.2
Clear-sky	-2.2	12.1	-0.6	1.1	-0.9	2.8
All-sky	-2.0	8.9	-1.6	2.1	-1.8	3.2

Table 3.2: Bias and Root-Mean-Square Differences (RMSD) of fluxes, in percent, from 2B-FLXHR-LIDAR relative to CERES for scenes containing a given cloud phase (liquid, ice, mixed-phase, and multilayered).

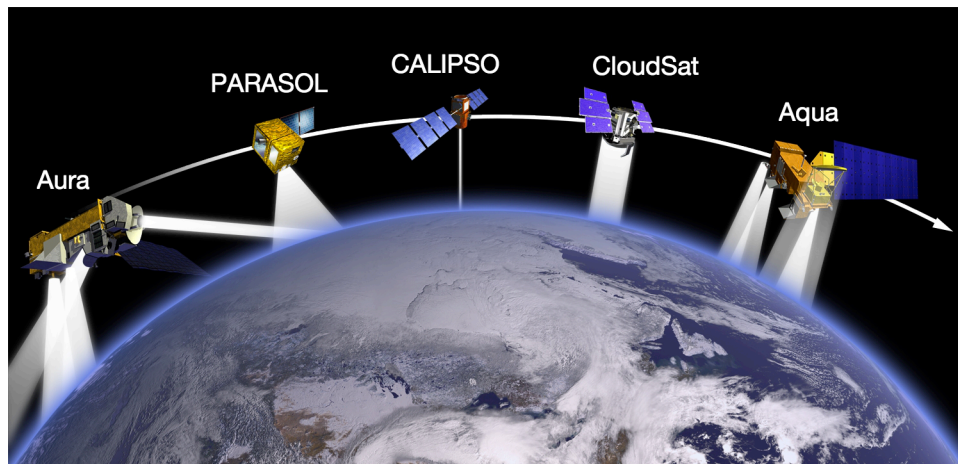


Figure 3.1: NASA's A-Train constellation of satellites monitor Earth's climate using a suite of nearly simultaneous, collocated spaceborne sensors.

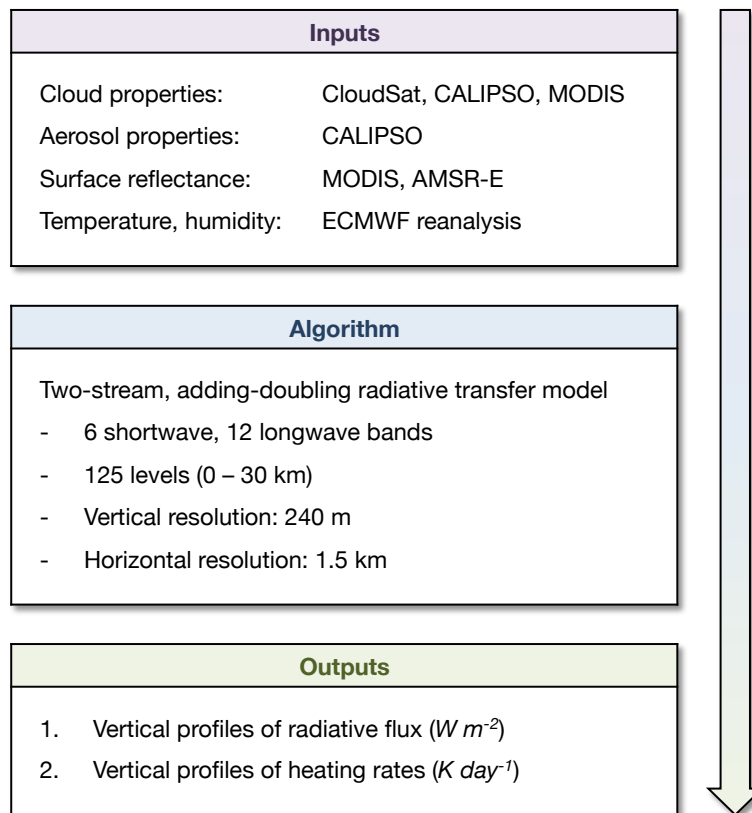


Figure 3.2: A general flowchart of the CloudSat 2B-FLXHR-LIDAR algorithm.

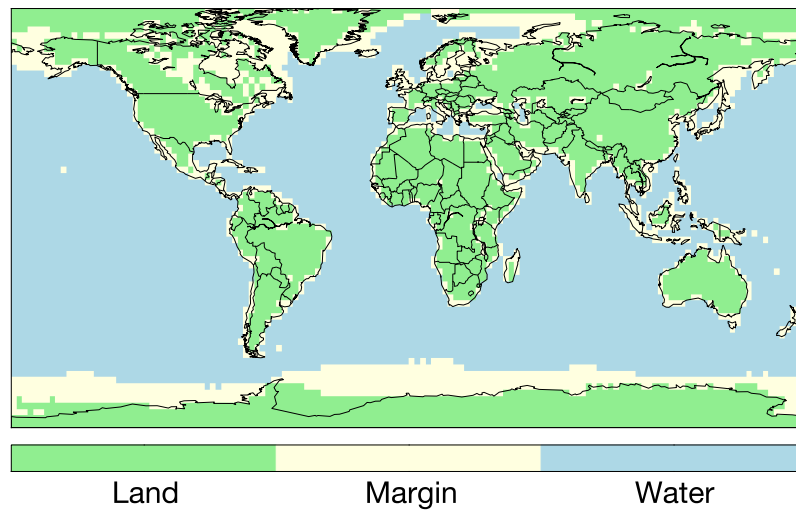


Figure 3.3: Annual mean land-ocean masks used in the 2B-FLXHR-LIDAR dataset are based on surface classifications from the International Geosphere-Biosphere Programme (IGBP).

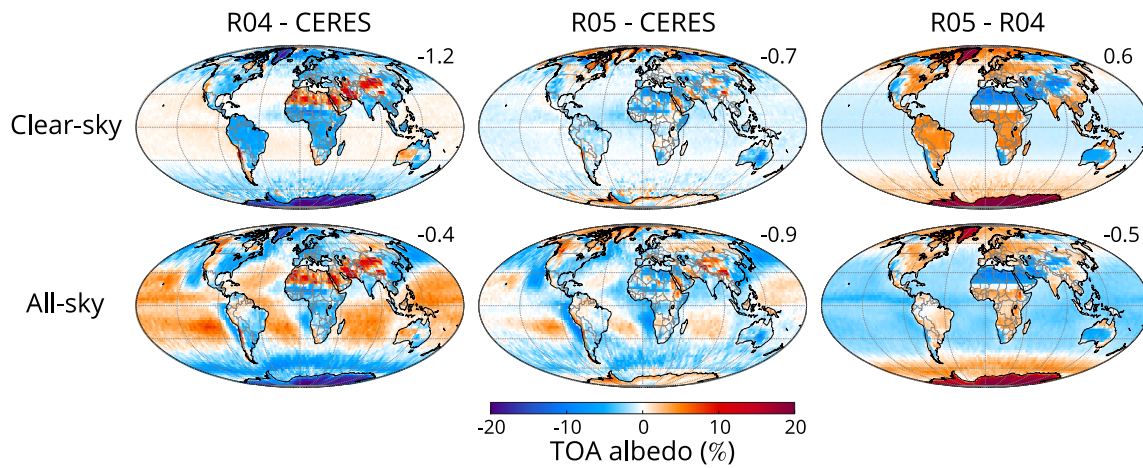


Figure 3.4: Comparisons of annual mean top-of-atmosphere (TOA) albedo from R05 2B-FLXHR-LIDAR, R04 2B-FLXHR-LIDAR, and CERES SSF over 2007–2010. Values displayed in the top right of all maps are area-weighted global averages.

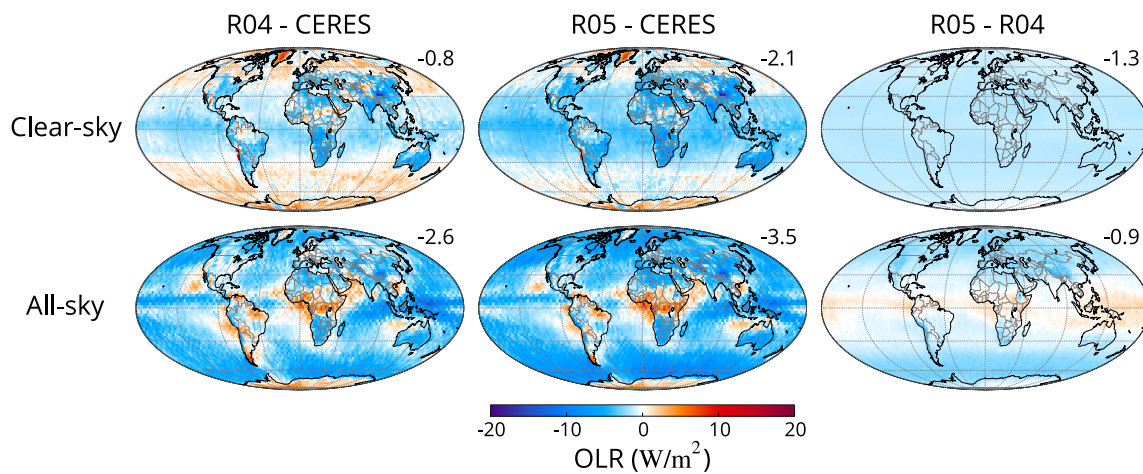


Figure 3.5: Same as Figure 3.4 but for outgoing longwave radiation (OLR).

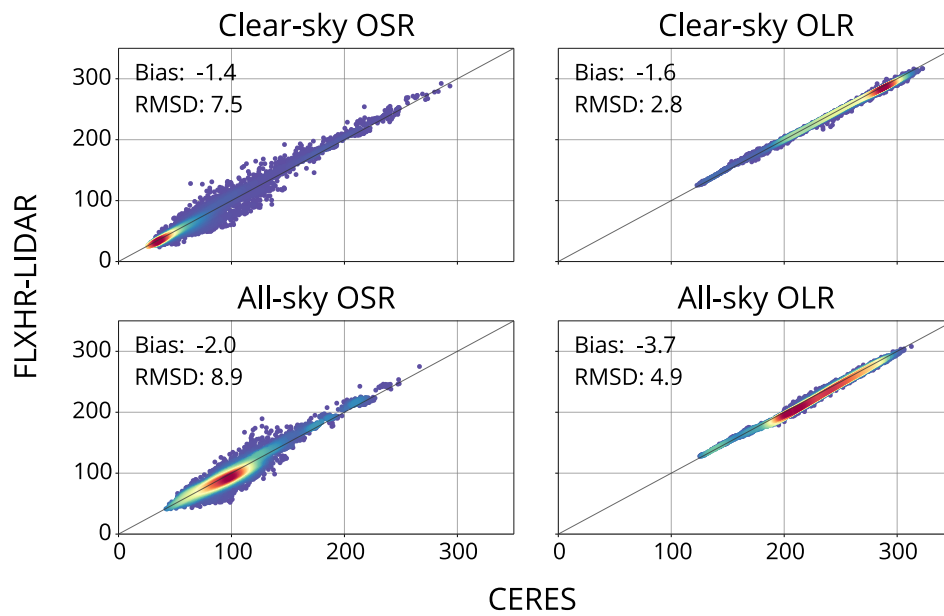


Figure 3.6: Scatterplots of outgoing shortwave (OSR) and longwave radiation (OLR), in W m^{-2} , comparing R05 2B-FLXHR-LIDAR to CERES. Each point represents a $2.5^\circ \times 2.5^\circ$ latitude-longitude grid box of fluxes averaged over 2007–2010.

Chapter 4

The Influence of Cloud Cover on Aerosol Direct Effects

4.1 Introduction

The results presented in this chapter include work published by the author in a peer-reviewed journal (Matus et al., 2015). Accordingly, some of the methodology described in this section will be reintroduced in subsequent chapters in the interest of consistency. Many previous studies have contributed to this analysis and citations to these publications are included within the manuscript text.

Aerosol interactions with solar radiation play a significant yet still uncertain role in climate (Yu et al. 2006). Large uncertainties in global estimates of DRE currently exist as a result of incomplete knowledge of aerosol and environmental characteristics (Anderson et al. 2005; Jaeglé et al. 2011; Satheesh and Krishna Moorthy, 2005). Reducing these uncertainties requires improved understanding of aerosol optical properties (e.g., aerosol optical depth, asymmetry parameter, and single scattering albedo) and the albedo of the underlying surface (Hansen et al. 1997; Myhre et al. 2005). While aerosol DRE may be evaluated at any level of the atmosphere, the two most important levels to consider from a radiative balance perspective are the TOA and surface. Aerosol direct effects at the TOA represent the overall impact of aerosols on global radiative balance, whereas surface direct radiative effects govern the partitioning of these impacts between the atmosphere and ocean. The latter has important implications for the role of aerosols in the climate system since the atmosphere and ocean respond to external forcings on very different time scales. At the TOA, scattering aerosols typically exert a negative DRE, while absorbing aerosols produce a negative DRE over dark surfaces (e.g., ocean) and a positive DRE over bright surfaces (e.g., sea ice and desert) or bright clouds. A positive DRE at the TOA represents an addition of energy to the Earth–atmosphere system (a net warming effect) whereas a negative DRE denotes a loss of energy (a net cooling effect) (Yu et al. 2006). Since both absorbing and scattering aerosols reduce the energy incident at the surface, aerosol DRE at the surface is always negative.

Global climate models, while providing useful benchmarks for global estimates of DRE, have been shown to exhibit deficiencies in their ability to correctly represent the optical properties and relative positions of clouds and aerosols (Schulz et al. 2006; Kay et al. 2012). Quijano et al. (2000) and Penner (2003), for example, demonstrate that models must correctly place overlapping cloud and aerosol layers in the vertical to accurately compute radiative fluxes. Likewise, Chung et al. (2005) show that uncertainty in the modeled direct radiative forcing of anthropogenic aerosols ranges sixfold (from 20.1 to 20.6 W m^{-2}) depending on the relative vertical distributions of aerosols and clouds. Improving the model representation of aerosol radiative effects in cloudy regions is therefore critical for improving global assessments of aerosol climate forcing. It follows that high-quality observations of the relative placement of aerosols and clouds are necessary for validating and effectively constraining climate model simulations of aerosol radiative effects (Chin et al. 2009).

As satellite remote sensing remains the only means of observing the large spatial and temporal variability in aerosol properties, satellite observations have been used extensively to perform global estimates of DRE (Chin et al. 2009; Yu et al. 2006; Bergamo et al. 2008; Di Biagio et al. 2010). However, the passive sensors that lie at the root of many previous studies measure column-averaged properties and have limited capabilities to resolve the vertical distributions of clouds and aerosols. Retrievals of aerosol properties from passive sensors are often impossible or highly biased in the presence of clouds and over bright surfaces, which severely limits our ability to quantify DRE in cloudy skies or over many land areas (Remer et al. 2005; Kaufman et al. 2005). With coverage limited to cloud-free oceans, passive satellite-based estimates of DRE range from -4 to -6 W m^{-2} (Bellouin et al. 2005; Loeb and Manalo-Smith 2005; Yu et al. 2006; Myhre et al. 2007).

Satellite remote sensing of aerosols over cloud and land surfaces, while previously elusive, is now possible using a combination of active and passive sensors (Torres et al. 2007; Omar et al. 2009; de Graaf et al. 2012; Waquet et al. 2009; Patadia et al. 2008). These new measurements are critical since clouds modify the radiative effects of aerosols by altering the underlying surface albedo (Haywood 2003; Myhre et al. 2005). While aerosols typically exert a negative DRE, absorbing aerosols residing over a bright cloud can produce a positive DRE (Chand et al. 2009; Wilcox 2012). The strength of the warming effect from absorbing aerosols is highly sensitive to the reflectance and

coverage of any underlying clouds, highlighting the need for collocated cloud and aerosol measurements (Winker et al. 2010).

This study seeks to address previous observational limitations using new multi-sensor aerosol, cloud, and radiative flux products from the A-Train satellite constellation (L'Ecuyer and Jiang 2010). The dataset uses collocated observations from CloudSat, CALIPSO, MODIS, and AMSR-E sensors, specifically designed to identify the precise location of clouds and aerosols and provide vertically resolved estimates of water contents, cloud particle size, and aerosol optical depth (AOD). This combination of active and passive observations provides the unique opportunity to estimate aerosol radiative effects in historically poorly sampled regimes including those above clouds and over land surfaces. The unprecedented ability of these sensors to resolve the vertical structure of clouds and aerosols thus offers unique insights into the complex role clouds play in modulating aerosol direct effects.

Given recent advances in satellite remote sensing of clouds and aerosols, it is necessary to revisit global assessments of aerosol direct effects. This work is motivated by two expected outcomes. First, the combination of active and passive observations will provide a more complete estimate of global DRE than conventional estimates based exclusively from passive observations. Second, biases in modeled DRE will be largest over regions where cloud fields are poorly simulated (e.g., stratocumulus over the southeastern Pacific). Given that clouds have been shown to exert significant influence on aerosol direct effects, biases in modeled DRE may be larger over regions where cloud cover is poorly simulated in models. Such errors, in turn, have potentially strong implications for the ability of models to simulate anthropogenic aerosol radiative forcing. If clouds impact the radiative effects of all aerosols, then it follows that clouds also impact the radiative forcing of anthropogenic aerosols.

Here we present new estimates of the global distribution of aerosol direct effects, in both clear and cloudy skies, using a novel approach that leverages the strengths of CloudSat and CALIPSO. These new estimates are used to evaluate the simulated representation of aerosol direct effects in the Community Earth System Model (CESM). While the modeled estimate of global, annually averaged DRE agrees well with the new observational estimate, large regional biases exist. These biases likely

result from a combination of errors in aerosol sources, aerosol optical properties, and cloud cover. Assessing the model representation of aerosols has been discussed in greater detail elsewhere (Lamarque et al. 2013; Liu et al. 2012; Neale and Chen 2010). Here, the new capability of A-Train sensors to estimate aerosol radiative effects over all surfaces and in all sky conditions will be used to assess the contribution of cloud cover biases to errors in CESM-simulated aerosol radiative effects.

4.2 Methodology

CloudSat's level 2B radiative fluxes and heating rates with lidar (2B-FLXHR-LIDAR) data product provides observationally constrained radiative transfer calculations of broadband radiative fluxes and heating rates (Henderson et al. 2013). Vertical distributions of liquid and ice cloud effective radii and water contents from CloudSat's level 2B cloud water content product (2B-CWC) are combined with temperature and humidity profiles from the European Centre for Medium-Range Weather Forecasts (ECMWF) analyses as well as surface albedo and emissivity data from the International Geosphere–Biosphere Programme (IGBP) global land surface classification. Collectively, these data initialize a broadband radiative flux model, known as BUGSrad, to compute vertical profiles of radiative fluxes and heating rates.

BUGSrad is a two-stream, adding-doubling solution to the radiative transfer equation introduced by Ritter and Geleyn (1992). The model assumes a plane-parallel atmosphere over the 1.4 km \times 1.8 km CloudSat field of view. Molecular absorption and scattering is computed using the correlated-k method of Fu and Liou (1992). The delta-Eddington approximation is applied over six shortwave bands and a constant-hemisphere approximation is applied over 12 longwave bands. The bands are then weighted and combined into broadband estimates of shortwave and longwave fluxes. Finally, the algorithm computes the pressure derivative of net radiative flux to derive vertical atmospheric heating rates.

The resulting fluxes and heating rates are output for each CloudSat footprint at a vertical resolution of 240 m, forming the standard CloudSat radar-only 2B-FLXHR data product (L'Ecuyer et al. 2008). The 2B-FLXHR-LIDAR data product used in this study builds on the basic 2B-FLXHR

framework to include several refinements that are particularly relevant for evaluating aerosol direct effects (Henderson et al. 2013). By including coincident lidar observations from CALIPSO and radiance measurements from MODIS, the representation of thin cirrus, marine stratocumulus, and aerosols have all been improved in the radiative flux calculations.

Radiative flux calculations are further constrained using vertically resolved satellite observations of cloud, precipitation, and aerosol properties. Cloud location in 2B-FLXHR-LIDAR is determined based on CloudSat's level 2B geometrical profiling with lidar product (2B-GEOPROFlidar) and cloud properties are assigned based on a combination of CloudSat's radar-only 2B-CWC product (2B-CWC-RO), the MODIS-based level 2B cloud optical depth product (2B-TAU), and CALIPSO's version 3 products. Precipitation location and intensity are identified using CloudSat's level 2C precipitation column algorithm (2C-PRECIP-COLUMN) product, which retrieves cloud and rain liquid water contents and estimates the vertical extent of liquid precipitation in the column. CALIPSO lidar backscatter retrievals supply the aerosol information used in the 2B-FLXHR-LIDAR data product. The location and optical depth of aerosols are obtained from CALIPSO's 5-km aerosol layer product, while aerosol types and vertical distribution are retrieved using CALIPSO's vertical feature mask product (Vaughan et al. 2009).

Aerosols are classified by type using the CALIPSO aerosol models, based on a cluster analysis of AERONET measurements as described in Omar et al. (2009). Each aerosol layer is assigned a value of single scattering albedo and asymmetry parameter based on the CALIPSO 532-nm aerosol optical depth and mean radius, using a technique similar to that employed in the Spectral Radiation-Transport Model for Aerosol Species (SPRINTARS) global transport model (Takemura et al. 2002). Table 1 summarizes the mean optical properties of the six CALIPSO aerosol types in the visible band, including the effective radii of fine and coarse modes, single scattering albedo, and asymmetry parameter.

Given that radiative fluxes in 2B-FLXHR-LIDAR are calculated using a radiative transfer model, aerosol-free conditions can be readily simulated by simply setting all aerosol fields to zero. The algorithm performs two independent sets of flux calculations—one with aerosol included and another with aerosol artificially removed—so that DRE may be computed as the difference in net radiative

flux (downwelling minus upwelling) between the two sets of outputs. This approach to quantify aerosol DRE mimics the approach used to compute DRE from climate model simulations, thus providing a more direct means for comparing against model output. As previously noted, this study only considers the shortwave DRE at the top of the atmosphere. To account for the diurnal cycle of solar insolation, the radiative transfer calculations simulate all possible zenith angles in 2-hour increments. The average of the resulting fluxes approximates the diurnal mean but does not account for diurnal variations in cloud cover. Although release 4 of the 2B-FLXHR-LIDAR dataset uses temperature and humidity from ECMWF analyses, it should be noted that the source of temperature and humidity information has a negligible effect on the estimates of aerosol DRE analyzed here since they derive from flux differences.

The 2B-FLXHR-LIDAR dataset comprises 285 million radiative flux profiles with near-global coverage (82.5°S–82.5°N) from July 2006 to April 2011. For quality control, profiles with incomplete or missing input data are removed from the dataset. Data are screened based on the quality control flags included in the dataset that test for the following criteria: high uncertainty or missing cloud water content (CWC), missing 2B-TAU data, missing CALIOP, missing MODIS data mapped to CloudSat profiles (MODIS-AUX), missing AMSR-E data mapped to CloudSat profiles (AMSR-AUX), or out-of-bounds flux observations. The specific criteria are described in greater detail in Table 14 of the CloudSat 2B-FLXHR-LIDAR data product documentation (Henderson and L'Ecuyer, 2011).

2B-FLXHR-LIDAR estimates of DRE are partitioned by surface type and sky conditions to gain insight into the environmental factors that influence aerosol direct effects. Since bright surfaces enhance atmospheric warming from absorbing aerosols while dark surfaces enhance cooling from scattering aerosols, accurate assessment of aerosol direct effects requires knowledge of the underlying surface reflectance. The 2B-FLXHR-LIDAR algorithm accounts for land and ocean reflectance characteristics using surface albedo and emissivity data from the IGBP global surface classification. The IGBP global land cover classification is derived from a suite of observational MODIS products aboard the Terra and Aqua platforms. Land cover data are gridded at 2.5° spatial resolution to produce high-quality seasonal and annual global composites of 17 land cover types

(Moody et al. 2005). The surface of each 2B-FLXHR-LIDAR footprint is categorized as land or ocean. Since the shortwave albedo of sea ice is more representative of land rather than ocean, we group all pixels detecting land or sea ice in one category. Based on this classification, Earth's surface is 56% open ocean and 44% non-ocean (i.e., land or sea ice) averaged globally.

Cloud phase, water content, and relative location to aerosol layers also exert influence on the radiative effects exerted by aerosols. Like a bright land surface, clouds may enhance atmospheric heating from absorbing aerosols or mask the cooling imposed by scattering aerosols (Chand et al. 2012; Soden et al. 2004). In this study, sky conditions are categorized as clear sky or cloudy sky. Clear-sky conditions are assessed if neither CloudSat nor CALIPSO detects cloud or precipitation. If either CloudSat or CALIPSO detects cloud, however, the profile is labeled as cloudy sky. Based on column-integrated cloud optical depth derived from combined CloudSat and CALIPSO observations, cloudy-sky pixels are further classified as thin clouds ($\tau < 1$) or thick clouds ($\tau > 1$). The threshold choice of $\tau > 1$ is arbitrarily chosen to separate optically thin cirrus from thicker convective anvils and liquid or mixed-phase clouds. Since thin clouds are more transparent to visible radiation, aerosol direct effects are often comparable to clear-sky conditions when thin cirrus is present.

Any uncertainties in CALIPSO aerosol retrievals will ultimately influence the 2B-FLXHR-LIDAR estimates of aerosol radiative effects. It is important to note, however, that these uncertainties are likely much smaller than those encountered in individual scenes or limited field experiments resulting from significant reduction of random errors over the large space and time scales analyzed. The global median relative difference between AERONET and CALIPSO AOD, for example, is 25% for AOD greater than 0.1, with differences possibly resulting from cloud contamination, scene inhomogeneity, instrument view angle differences, CALIPSO retrieval errors, and detection limits (Omar et al. 2013). Additional validation studies have revealed a low bias in CALIPSO estimates of AOD with respect to other global measurements and retrievals (Redemann et al. 2012; Schuster et al. 2012). Recent studies have also shown that CALIPSO may suffer from uncertainty in the classification of aerosol types (Omar et al. 2013), can misclassify dense aerosol layers as clouds (Schuster et al. 2012), and may fail to detect aerosols with low AOD, especially in the presence of clouds (Kacenelenbogen et al. 2014).

To assess the uncertainty in simulated fluxes due to errors in CALIPSO aerosol products, Henderson et al. (2013) conducted several sensitivity studies where 1) CALIPSO AOD retrievals were increased and decreased by a factor of 2, a conservative approximation to the error estimates of Kittaka et al. (2011), 2) all non-marine aerosols were changed to smoke, 3) all non-marine aerosols were changed to dust, and 4) all smoke aerosols were changed to dust. Given that the goal here is not to perfectly represent small spatial and temporal variations in aerosol properties but rather to assume characteristics that are reasonably representative of large-scale mean conditions, the variance between these five cases provides conservative bounds on the potential error in simulated fluxes resulting from both retrieval errors and errors in assumed single scattering properties. All uncertainties reported on the subsequent figures derive from the standard deviation of these individual assessments (five perturbed estimates and the original unperturbed estimate), assuming that the error sources are independent and uncorrelated.

4.3 Global aerosol direct effects

Table 2 summarizes estimates of annual-mean DRE from the 2B-FLXHR-LIDAR and CESM1(CAM5) datasets as partitioned by surface (land, ocean, and global) and sky conditions (clear sky, cloudy sky with thin clouds, cloudy sky with thick clouds, and all sky). Note that since both model-based and observation-based estimates of DRE derive from independent calculations with aerosol removed, the all-sky DRE can be reconstructed after this separation as the linear sum of the cloudy-sky DRE weighted by the cloud fraction and the clear-sky DRE weighted by the fraction of clear sky:

$$DRE_{all-sky} = DRE_{cloudy} \times CF + DRE_{clear} \times (1 - CF) \quad (3)$$

The global estimate of all-sky DRE from 2B-FLXHR-LIDAR observations is -1.9 W m^{-2} with an uncertainty range of $\pm 0.6 \text{ W m}^{-2}$. The observed all-sky DRE is 33% stronger over ocean (-2.0 W m^{-2}) than over land (-1.5 W m^{-2}). Since open ocean comprises 56% of all observations, the global

estimate is weighted toward the ocean value. Interestingly, the annual-mean DRE in clear skies is comparable over land and ocean despite significantly greater aerosol emissions from terrestrial sources. This suggests that the reduced contrast between aerosols and the higher albedo of land surfaces offsets the larger aerosol concentrations characteristic of continental regions (Myhre 2009). Over scenes where thin cloud is detected, the observed estimate of global DRE is reported to be -2.0 W m^{-2} . Thin clouds thus weaken the global cooling effect of aerosols by 30%, on average, compared to clear-sky observations. Globally, aerosols over optically thick clouds are reported to have a positive radiative effect of $+0.1 \text{ W m}^{-2}$. Over land, however, aerosols over thick clouds exert a warming effect ($+0.8 \text{ W m}^{-2}$), which offsets the cooling effect over ocean (-0.3 W m^{-2}).

There is good agreement between global estimates of all-sky DRE from 2B-FLXHR-LIDAR observations (-1.9 W m^{-2}) and the CESM1(CAM5) simulation (-1.7 W m^{-2}). Despite this agreement under global all-sky conditions, there are large discrepancies in the estimates of aerosol direct effects over certain surface types and sky conditions. Over land, the observed all-sky DRE is over three times stronger than the CESM-simulated DRE. This inconsistency in aerosol DRE over land is most pronounced in cloudy skies, because of an enhanced warming effect simulated in CESM as compared to 2B-FLXHR-LIDAR observations. This enhanced warming effect, which will be discussed in greater detail later in this section, largely offsets any cooling effect and results in a weaker modeled DRE over land.

Over oceans, however, all-sky DRE estimates from CESM agree well with observations owing to compensating high and low biases in clear and cloudy skies, respectively. These differences are indicative of two important sources of uncertainty that will be illustrated more clearly in the regional analyses that follow. First, there are significant differences in the modeled and observed cloud cover, with CESM indicating 38% of all oceanic scenes being clear as compared to only 29% in the observations. Second, there are significant differences between modeled and observed estimates of clear-sky and cloudy-sky DRE that may suggest uncertainties in aerosol amount, optical properties, or sampling biases introduced by differences in the specific scenes that contribute to cloudy-sky and clear-sky calculations. For example, since clear-sky DRE estimates are very sensitive to the solar zenith angle and aerosol optical properties, systematic biases in the frequency with which darker

surfaces (e.g., tropical ocean) or scenes with higher aerosol loading enter the clear-sky calculations in CESM may cause systematic overestimates of clear-sky DRE relative to the observations, even if the aerosol properties are correctly prescribed in the model.

Global estimates of clear-sky DRE from 2B-FLXHR-LIDAR and CESM1(CAM5) datasets agree within 30%. However, the observed cloudy-sky DRE (-1.4 W m^{-2}) is more than twice as strong as the simulated cloudy-sky DRE (-0.6 W m^{-2}). For estimates of cloudy-sky DRE, the magnitude of the radiative effect is influenced by the optical thickness of the cloud. Once observations are partitioned by cloud optical depth, it is evident that modeled cloudy-sky DRE agrees better with observed DRE in the presence of optically thick clouds. In particular, CESM-simulated cloudy-sky DRE over land is nearly equivalent to the observational estimate in the presence of thick clouds ($+0.8 \text{ W m}^{-2}$). Optically thin clouds, on the other hand, are shown to have aerosol radiative effects that are in better agreement with clear-sky values.

This result is supported by Figure 4.1, which maps the spatial distribution of annual-mean DRE observed in the 2B-FLXHR-LIDAR dataset. Consistent with Table 4.2, aerosol direct effects are separated by sky conditions, including clear sky, cloudy sky (all clouds), cloudy sky (thin clouds), and cloudy sky (thick clouds). Although 2B-FLXHR-LIDAR observations and CESM1(CAM5) simulations compare favorably for estimates of all-sky DRE, their clear-sky and cloudy-sky DRE estimates disagree. Observed clear-sky DRE, shown in Figure 4.1a, is strongest over the North Atlantic and Southeast Asia with values stronger than -10 W m^{-2} over some locations. Although aerosols exert a warming effect regionally over the bright Sahara, a cooling effect predominates globally as evidenced by the negative global estimate of clear-sky DRE (-2.6 W m^{-2}). The uncertainty of the clear-sky DRE estimate is $\pm 0.6 \text{ W m}^{-2}$, which is lower than in cloudy skies. The global pattern of DRE with optically thin clouds is similar to that with clear skies, as shown in Figs. 1a and 1c. Since thin clouds are nearly transparent to shortwave radiation, shortwave aerosol direct effects are not significantly altered compared to clear-sky conditions.

Figure 4.1d reveals a considerably different pattern for aerosol direct effects in the presence of optically thick clouds ($\tau > 1$). Under these conditions, the global estimate of DRE is $+0.1 \text{ W m}^{-2}$ with an uncertainty range of $\pm 1.0 \text{ W m}^{-2}$. Positive aerosol direct effects are observed over known source

regions of absorbing dust aerosols (e.g., northern Africa and western Australia) and absorbing smoke aerosols (e.g., southern Africa and Southeast Asia), where the magnitude of cloudy-sky DRE exceeds $+2 \text{ W m}^{-2}$. Although absorbing aerosols residing over optically thick clouds may exert a net warming effect, it is also possible for above-cloud aerosols to exert a net cooling effect. If the aerosol optical depth is comparable in magnitude to the cloud optical depth, non-absorbing aerosols may enhance the reflection of shortwave radiation. Negative aerosol direct effects are observed over the northeastern Atlantic, southeastern Pacific, and Arabian Sea where relatively high AOD is detected by CALIPSO observations (see Figure 4.2). However, it is worth noting that large uncertainties may exist with DRE observations around cloud edges because of the possible misclassification of dust aerosol as cloud (Omar et al. 2009). Finally, Figure 4.1b shows the global pattern of DRE in the presence of all clouds. Collectively, the maps from Figure 4.1 highlight that aerosol direct effects are spatially heterogeneous and highly sensitive to cloud cover.

Global maps of all-sky DRE and total cloud fraction from 2B-FLXHR-LIDAR and CESM1(CAM5) datasets are compared in Figure 4.3. For consistency with the observationally derived cloud fraction estimates from CloudSat and CALIPSO, CESM-simulated cloud fraction is evaluated using the GCM-Oriented CALIPSO Cloud Product (GOCCP) that simulates what these satellites would observe if flying above an atmosphere similar to that predicted by the model (Chepfer et al. 2010). Both datasets are qualitatively consistent in their representation of aerosol direct effects on a global scale. In both observations and simulations, aerosols exert a cooling effect over darker ocean and a warming effect over brighter deserts. The shortwave radiative effects of aerosols tend to be strongest near the equator as a result of higher solar insolation.

On local scales, however, both the magnitude and pattern of modeled and observed aerosol direct effects are inconsistent. While 2B-FLXHR-LIDAR observes the strongest annual-mean DRE over ocean, CESM1(CAM5) simulates the strongest effects over land. In particular, CESM1(CAM5) significantly overestimates annual-mean DRE over northern Africa and underestimates annual mean DRE over southern Africa, which is likely due to a combination of errors in the strength of aerosol sources and optical properties over the region. This result is consistent with findings from Shindell et al. (2013), who found that models from phase 5 of CMIP (CMIP5), including CESM1(CAM5),

underestimate biomass burning emissions and overestimate absorbing AOD over the Sahara. Despite uncertainties in the aerosol optical properties and optical depth assigned to the satellite observations, even doubling AOD and systematically attributing all aerosols to smoke cannot account for these differences.

In addition to uncertainties in aerosol properties, discrepancies between observed and simulated DRE over ocean also appear to be linked to the global distribution of clouds. Inconsistencies in the simulated pattern of aerosol direct effects are most evident in high pressure, subsidence regions over subtropical ocean. Over these regions, CESM1(CAM5) simulates stronger aerosol direct effects than observed in the 2B-FLXHR-LIDAR dataset. Furthermore, the model simulates a lower cloud fraction compared to observations. Since reduced cloudiness over ocean enhances the cooling effect of scattering aerosols, modeled aerosol direct effects are thus strengthened by an underestimate in marine cloud cover.

While clouds are not the only source of DRE biases, cloud cover almost certainly contributes to model biases over some regions. These cloud cover biases in CESM are evident in the global cloudiness statistics. Although CESM1(CAM5) and 2B-FLXHR-LIDAR capture similar large-scale patterns in cloudiness, there are fewer clouds represented in the model. The global-mean cloud fraction is lower in the model (63%) than in observations (70%), which are based on five years of CloudSat and CALIPSO data. As displayed in Figure 4.3, clouds in the subtropics are especially underrepresented in the CESM simulation. In particular, CESM1(CAM5) greatly underestimates the geographical extent of marine stratocumulus clouds in the southeastern Pacific and southeastern Atlantic compared to satellite observations (Kay et al. 2012). Given the strong radiative effects of marine stratocumulus, which cover about 20% of the globe and have a higher albedo compared to ocean, model biases in marine cloud cover likely affect regional estimates of aerosol radiative forcing (Albrecht 1989; Warren et al. 2007). Qualitatively, Figure 4.3 suggests that aerosol direct effects are sensitive to cloud cover. Especially over ocean, stronger DRE coincide with low cloud fraction and weaker DRE coincide with high cloud fraction. In an effort to quantify this effect, Figure 4.4a expresses the relationship between DRE and cloud fraction over global ocean. All estimates of DRE and cloud fraction are monthly averaged and evaluated at a 2.5° resolution. The trend of weaker DRE

with increasing cloud fraction is consistent in both 2B-FLXHR-LIDAR and CESM1(CAM5). Both datasets show a similar sensitivity of DRE to cloudiness based on the slope of these lines. However, Figure 4.4b indicates that CESM1(CAM5) samples about 10% fewer clouds over global ocean than CloudSat/ CALIPSO observations. In other words, the model is skewed more toward clear-sky values, which results in stronger negative DRE over ocean. These findings are consistent with Figure 4.3 and suggest that model biases in DRE over ocean are driven primarily by errors in cloud cover as opposed to errors in aerosol properties.

4.4 Evidence of the importance of cloud cover

The role of cloud cover in modifying large-scale aerosol radiative effects has received much less attention in the literature than the alternate problem of aerosols modifying cloud radiative effects. Yet a growing body of evidence suggests that global models exhibit large errors in cloud cover over several regions (Bony et al. 2006; Jiang et al. 2012; Kay et al. 2012; Su et al. 2013) and recent studies demonstrate that clouds may have a profound influence on aerosol direct effects (Chung et al. 2005; Chand et al. 2009; Winker et al. 2010). With new vertical structure information provided by active sensors in the A-Train, it is important to revisit this topic to document the potential effects of model cloud biases on simulations of aerosol radiative effects. To investigate these effects, CESM-simulated DRE is evaluated over the southeastern Pacific and southeastern Atlantic. These regions feature semi-permanent marine stratocumulus clouds that are known to exert significant influence on the physics and dynamics of the climate system (Teixeira et al. 2011). The sources of aerosols vary greatly over these regions, allowing the effects of cloud cover on scattering and absorbing aerosols to be contrasted.

4.4.1 Marine aerosols over the SE Pacific Ocean

The southeastern Pacific is known for its wide variability in boundary layer, cloud, and aerosol properties. The region bounded by 35°–5°S, 130°–65°W is adopted to include the full extent of marine stratocumulus clouds along the western coast of South America. The southeastern Pacific is a

relatively clean marine environment characterized by contributions from both natural and anthropogenic aerosols, although anthropogenic aerosols predominate near the coast. Clean marine aerosols, consisting of complex mixtures of constituents from various origins, are composed primarily of sea salt and sulfate particles (Blot et al. 2013). This is consistent with CALIPSO observations from Figure 4.5 that show a dominant aerosol type of “clean marine” consisting of a mixture of sea salt and sulfate. Both sea salt aerosols, produced from the evaporation of sea spray, and sulfate aerosols, produced from the ocean release of dimethyl sulfide (DMS), scatter solar radiation and exert a net cooling effect on climate (see Table 1).

Figure 4.6 compares the spatial distribution of annual-mean DRE and low cloud fraction from the 2B-FLXHR-LIDAR and CESM1(CAM5) datasets. In this study, observed low clouds are identified as those with a cloud top temperature warmer than 273 K. Figure 4.6c shows that observed low clouds from CloudSat/CALIPSO cover an extensive area over the southeastern Pacific. The effect of cloud masking results in weakened aerosol direct radiative effects over ocean (Soden et al. 2004). Consequently, the observed aerosol direct effects are relatively weak and spatially uniform over the ocean, with a regional estimate of $21.9 \pm 0.6 \text{ W m}^{-2}$. In contrast to observations, CESM1(CAM5) simulates a regional estimate of -2.5 W m^{-2} as illustrated in Figure 4.6b. CESM-simulated estimates of DRE exceed -5 W m^{-2} over an isolated area off the coast of Peru. While uncertainties in aerosol source strength cannot be ruled out, deficiencies in the spatial pattern of clouds almost certainly contribute to the excess model DRE over this region.

Cloud cover influences aerosol radiative effects by modifying the albedo of the underlying surface. As shown in Figure 4.6, CESM simulates the strongest aerosol direct effects over areas with the least cloud cover. While the cooling effect of scattering aerosols over the dark ocean can be significant in clear skies, an increase in cloudiness reduces this cooling effect by providing a much brighter background and masking aerosol layers beneath cloud cover. Overall, CESM1(CAM5) simulates less cloud cover over the southeastern Pacific than observed by CloudSat and CALIPSO. Figure 4.6 shows that the meridional extent of low clouds off the coast of Peru is approximately three times greater in satellite observations ($\sim 3000 \text{ km}$) than the CESM simulation ($\sim 1000 \text{ km}$). Furthermore, the simulated low cloud fraction is consistently lower in CESM1(CAM5) (35.9%) than

in 2B-FLXHR-LIDAR observations (44.3%). This result is consistent with findings from Kay et al. (2012), who found that CAM5 simulations underestimate the cloud fraction of marine stratocumulus. This reduction in marine stratocumulus cloud cover enhances the cooling effect exerted by scattering marine aerosols, thereby intensifying simulated aerosol radiative effects.

The effect of cloud cover on aerosol radiative effects is further highlighted in the domain-averaged estimates of the aerosol DRE. As summarized in Table 4.3, the total aerosol direct radiative effect from 2B-FLXHR-LIDAR observations is reported to be -1.9 W m^{-2} . Consistent with Figure 4.6, the radiative effects of aerosols are largely buffered by the presence of an extensive marine stratocumulus deck. Accordingly, observed estimates of clear-sky DRE (-2.1 W m^{-2}) and cloudy-sky DRE (-1.8 W m^{-2}) are comparable. Clouds predominate in the southeastern Pacific as 60% of profiles in this region are cloudy sky and the remaining 40% are clear sky. Cloud cover in the southeastern Pacific Ocean serves an important role in modulating radiative fluxes by diminish the cooling effect of scattering aerosols over open ocean, as reflected in these estimates.

In comparison, the model estimate of the total aerosol direct effect (-2.5 W m^{-2}) is over 30% stronger than observations. This value is influenced by contributions from the simulated clear-sky DRE, which is nearly twice as strong as the observed clear-sky DRE. Furthermore, there is 10% more clear sky simulated in the model than observed by CloudSat and CALIPSO. While both datasets show good agreement in estimates of cloudy-sky DRE, large discrepancies exist in estimates of clear-sky DRE. The spatial coverage of marine stratocumulus in the southeastern Pacific, therefore, strongly influences the net radiative effect of scattering aerosols. Overall, the southeastern Pacific Ocean is a unique region that provides a perfect natural laboratory to investigate the role of cloud cover on aerosol radiative effects. While the predominantly reflective marine aerosols exert a net cooling effect over this region, cloud cover ultimately influences the magnitude of this cooling effect. Marine stratocumulus clouds exert a strong influence in shaping the regional pattern of aerosol direct radiative effects. While satellite observations from CloudSat and CALIPSO identify an expansive cloud deck extending thousands of kilometers offshore in the southeastern Pacific Ocean, CESM1(CAM5) simulates a cloud deck that is much more spatially confined to the coast.

Consequently, the CESM1(CAM5) overestimation of aerosol radiative effects in this region likely results from model biases in cloud cover.

4.4.1 Biomass aerosols over the SE Atlantic Ocean

The southeastern Atlantic features a greater diversity in aerosol sources than the southeastern Pacific. The present study defines the southeastern Atlantic as the region bounded by 25°S–0°, 10°W–30°E and includes the full extent of marine stratocumulus clouds along the western coast of Africa. Biomass burning, a major source of aerosols in southern Africa, is most active during the dry season lasting from July through October (Sakaeda et al. 2011). Over 70% of fires in African savannas are anthropogenic and largely initiated for land clearing and land use change (Sheuyange et al. 2005). In addition to smoke from biomass burning, polluted dust (an external mixture of dust and smoke) is another source of absorbing aerosols over the southeastern Atlantic. Based on CALIPSO observations in Figure 4.7, smoke and polluted dust are the two aerosol types that contribute the most to total AOD in the southeastern Atlantic. Unlike marine aerosols, however, smoke and polluted dust aerosols are strong absorbers of solar radiation (see Table 1). Given the presence of a semi-permanent marine stratocumulus cloud deck over the southeastern Atlantic, aerosol direct effects are therefore sensitive to the relative positions of aerosols and clouds.

Figure 4.8 compares patterns of annual and seasonal mean DRE over the southeastern Atlantic from 2B-FLXHR-LIDAR observations and CESM simulation. The total aerosol direct effect averaged over the region is negative, indicative of a net cooling effect, although aerosols exert a localized warming effect off the coast of Angola. This region of positive DRE is consistent with the fact that elevated aerosols layers, advected by the mean flow, can be found at distances greater than 2000 km from the coast (Anderson et al. 2005). The positive aerosol direct effects off the coast of Angola result from absorbing aerosol layers residing above bright clouds (Chand et al. 2009). While all aerosols exert a cooling effect over cloud-free ocean, only absorbing aerosols overlying clouds may exert a warming effect over ocean. Because of the presence of elevated absorbing aerosol layers

and low-level clouds, the southeastern Atlantic is a region that frequently exhibits positive aerosol direct effects.

The columns of Figure 4.8 illustrate the spatial patterns of observed DRE averaged over December–February (DJF), March–May (MAM), June–August (JJA), and September–November (SON). Since biomass burning in Africa is largely driven by the seasonal migration of the intertropical convergence zone (ITCZ), the magnitude of aerosol direct effects in the southeastern Atlantic varies by season. In DJF the observed aerosol direct effect over the southeastern Atlantic is -2.1 W m^{-2} with an uncertainty of $\pm 0.9 \text{ W m}^{-2}$. During this time, biomass burning is largely confined to northern Africa, while southern Africa experiences its rainy season. Consequently, there is limited production of smoke aerosols from December through May. As biomass burning intensifies during JJA, aerosols exert a stronger cooling effect over central Africa and a warming effect off the coast of Angola. Despite increased localized variability, the regional aerosol direct effect in JJA remains negative (-2.1 W m^{-2}). Aerosols exert the strongest warming effect over ocean during SON, with DRE values exceeding $+4 \text{ W m}^{-2}$. The location where aerosols exert a warming effect over ocean coincides with the location of marine stratocumulus clouds. Since the warming effects largely offset the cooling effects, the observed DRE of -0.2 W m^{-2} in SON is significantly weaker than in other seasons. However, greater emissions of absorbing aerosols during SON contribute to a relatively higher uncertainty in the observed DRE ($\pm 1.4 \text{ W m}^{-2}$).

CESM1(CAM5) performs well in capturing the large-scale feature of aerosol heating off the coast of Angola. Estimates of annual-mean DRE over the southeastern Atlantic compare favorably between 2B-FLXHR-LIDAR (-1.7 W m^{-2}) and CESM1(CAM5) (-1.5 W m^{-2}). Despite this agreement in the annual mean, observations and simulations disagree on the spatial variability and seasonality of aerosol direct effects. Figure 4.8 shows that the model simulates an earlier onset of positive DRE off the coast of Angola. While it is more difficult to separate the relative contributions of uncertainties in aerosol properties from those due to differences in cloud cover, it is clear that the model representation of marine stratocumulus in the southeastern Atlantic is more spatially confined to the coast. This almost certainly contributes to aerosol direct effects that are more spatially confined to the

coast. Moreover, the warming effect of aerosols is considerably stronger in the model than observations.

To further illustrate the role clouds play in modulating aerosol direct effects, Figure 4.9 displays cumulative density functions of observed seasonally averaged DRE, as partitioned by sky conditions. The results illustrate that aerosol direct effects exhibit a seasonal cycle exclusively in cloudy skies. This seasonal cycle in DRE is more pronounced in the presence of thick clouds than thin clouds. Absorbing aerosols over optically thick clouds exert the strongest warming effect during SON, with 10% of observed DRE estimates larger than $+10 \text{ W m}^{-2}$. The cloudy-sky DRE is five times more likely to be positive in SON than MAM. There is also greater variability in the range of cloudy-sky DRE observed during SON. This is consistent with Figure 4.8, which also shows the greatest spatial variability in observed aerosol direct effects in SON. Since low-level clouds intensify the warming effect of absorbing aerosols, changes in the distribution of marine stratocumulus clouds can change the sign of DRE from negative to positive (Chand et al. 2009). Consequently, estimates of aerosol direct effects over the southeastern Atlantic are highly sensitive to the relative positions of absorbing aerosols and marine stratocumulus clouds.

Given that marine stratocumulus clouds significantly influence the strength of aerosol direct effects in the southeastern Atlantic, it is worthwhile to compare the observed and modeled seasonal cycles of DRE and the cloud fraction of low clouds (cloud tops warmer than 273 K). Figure 4.10 plots a time series of the monthly-mean DRE, low cloud fraction, and AOD over the southeastern Atlantic. Both datasets report comparable estimates of the annual-mean DRE with monthly-mean values ranging between -3 and $+1 \text{ W m}^{-2}$. While both datasets show a seasonal cycle in the total aerosol direct effect, observations and simulations disagree on the timing of this cycle. The observed DRE peaks in September, whereas CESM-simulated DRE peaks one month earlier in August. Cloud cover likely contributes to this timing of the seasonal cycle in DRE. Figure 4.10 shows that DRE becomes more positive as low cloud fraction increases during summer at the onset of the biomass burning season. This result is consistent with Chand et al. (2009), who found that the warming effect exerted by absorbing aerosols increases as cloud fraction increases. During JJA, low cloud fraction is consistently higher in CESM1(CAM5) simulation than CloudSat/CALIPSO observations.

Accordingly, simulated aerosol direct effects are more positive in the model during this time period. While these differences in DRE may be attributed to many factors (e.g., aerosol optical depth, aerosol layer height, and aerosol optical properties), cloud cover appears to play a significant role in modulating DRE over subtropical ocean.

The observed and simulated estimates of the annual-mean DRE over the southeastern Atlantic are summarized in Table 4.4. In the 2B-FLXHR-LIDAR observations, the regional estimate of the total aerosol direct effect is -1.7 W m^{-2} . The cloudy-sky DRE (-0.6 W m^{-2}) is five times weaker than the clear-sky DRE (-3.1 W m^{-2}) and is attributed to the warming effect exerted by absorbing aerosols over clouds. Despite good agreement between the datasets in the all-sky DRE estimates, cloudy-sky DRE is negative in observations and positive in the model. Compared to 2B-FLXHR-LIDAR observations, CESM1(CAM5) overestimates the warming effect from aerosols. Shindell et al. (2013) found that CAM5 tends to underestimate emissions of biomass burning aerosols over southern Africa. This suggests that marine cloud cover strongly influences the radiative effects of absorbing aerosols. Since aerosol radiative effects depend on both aerosol type and albedo of the underlying surface, discrepancies between observed and simulated DRE are likely explained in part by differences in low-level cloud cover.

In summary, the two main ingredients for positive DRE over ocean—absorbing aerosols and underlying clouds—must both be present for aerosols to exert a warming effect on climate. The southeastern Atlantic is a unique location in that absorbing biomass burning aerosols often reside above bright marine stratocumulus clouds. The resulting warming effect serves to offset the cooling effect of aerosols over the comparatively darker ocean. However, the magnitude and sign of aerosol direct effects are highly sensitive to the precise relative location of aerosols and clouds. Because of unresolved biases in the model treatment of marine stratocumulus clouds and possibly the amount of biomass burning aerosols, there are uncertainties in modeled aerosol direct effects in the southeastern Atlantic. The ability to accurately simulate DRE over this region therefore requires a more realistic representation of the spatial and temporal variability of clouds in addition to improved representation of aerosol sources and optical properties.

4.5 Chapter summary

It is well documented that the radiative effects of aerosols contribute to uncertainty in future climate predictions. Global assessments of aerosol direct effects remain challenging because of incomplete knowledge of aerosol characteristics on large space and time scales, especially in the presence of clouds and above bright surfaces. While the effects of aerosols on cloud radiative forcing have been extensively studied, the effects of clouds on aerosol radiative forcing have received much less attention, particularly on global scales, as a result of a lack of suitable observations.

While not immune to uncertainties, new multi-sensor observations from the A-Train satellite constellation provide key observational constraints necessary to identify and reduce uncertainties in model simulations of aerosol direct effects, especially those resulting from biases in the spatial and temporal distributions of clouds. CloudSat's new multi-sensor radiative fluxes and heating rates product leverages high-quality vertically resolved cloud and aerosol measurements critical to fill in the gaps in our understanding of aerosol radiative effects. Using this dataset, the present study seeks to improve upon previous efforts to assess the representation of aerosol direct effects in models by providing observational estimates of aerosol direct effects in both clear and cloudy skies. The results provide guidance for evaluating the impact of model cloud biases on simulated aerosol direct effects.

The global annual-mean DRE estimated from the 2B-FLXHR-LIDAR dataset is -1.9 W m^{-2} , a value that is in better agreement with estimates from global models than previous satellite-based techniques. Uncertainty in this global-mean value is $\pm 0.6 \text{ W m}^{-2}$, owing primarily to misclassification of aerosol types (Omar et al. 2013) and uncertainty in aerosol optical properties. The results may also be subject to underestimation of thin aerosol layers, especially in the presence of clouds (Kacenelenbogen et al. 2014), and misclassification of dense aerosol layers as clouds (Schuster et al. 2012). These uncertainties may partially offset one another but are difficult to quantify given current satellite instrumentation. The combination of simultaneous backscatter and extinction measurements from multi-wavelength High Spectral Resolution Lidar (HSRL) and phase function information from polarimeters being developed for the next generation of atmospheric composition satellites offers the potential to significantly reduce many of these sources of uncertainty in the near future.

While CESM1(CAM5) captures many large-scale features in observed aerosol direct effects, several large regional discrepancies exist that appear to be at least partially linked to biases in model cloud cover. An underrepresentation of low-level clouds in the southeastern Pacific, for example, leads to overestimates of the cooling effects of scattering aerosols. Likewise, a poor representation of the seasonal cycle of cloudiness in the southeastern Atlantic causes the model to overestimate the warming effects of absorbing aerosols early in the biomass burning season. These case studies highlight the important role clouds play in modulating aerosol direct effects. While a number of studies have documented the need for improving aerosol sources and optical properties in global models, the impact of cloud biases on aerosol direct radiative effects has not been as widely discussed. Given known uncertainties in model cloud cover and feedbacks, the results presented here suggest that the influence of clouds on aerosol radiative effects may represent an important source of uncertainty in regional climate predictions.

Aerosol type	r		ω	g
	Fine	Coarse		
Marine	---	1.22	0.99	0.54
Dust	0.2	2.84	0.99	0.76
Polluted continental	0.14	3.55	0.96	0.35
Clean continental	---	2.63	1.00	0.74
Polluted dust	0.21	3.16	0.96	0.39
Smoke	0.14	3.73	0.44	0.14

Table 4.1: Optical properties of the six CALIPSO aerosol types in the visible band, including mean radii for both fine and coarse modes, single scattering albedo, and asymmetry parameter.

Dataset	Surface	Clear-sky	Cloudy-sky		All-sky
			Thin ($\tau < 1$)	Thick ($\tau < 1$)	
2B-FLXHR-LIDAR	Land	-2.2 (14)	-1.6 (12)	+0.8 (17)	-1.5 (44)
	Ocean	-2.6 (16)	-2.2 (13)	-0.3 (27)	-2.0 (56)
	Global	-2.6 (31)	-2.0 (25)	+0.1 (44)	-1.9 (100)
CESM1(CAM5)	Land	-2.0 (15)	+0.8 (29)		-0.4 (44)
	Ocean	-3.9 (21)	-1.2 (35)		-2.1 (56)
	Global	-3.4 (36)	-0.6 (64)		-1.7 (100)

Table 4.2: Global estimates of annual mean DRE (W m^{-2}) from 2B-FLXHR-LIDAR and CESM1(CAM5) datasets. The fractional occurrence for each category is shown in parentheses. For this analysis, sea ice is included in the land category.

Dataset	Surface	Clear-sky	Cloudy-sky	All-sky
2B-FLXHR-LIDAR	Land	-1.4 (6)	+0.2 (8)	-0.5 (14)
	Ocean	-2.1 (34)	-2.1 (52)	-2.1 (86)
	Global	-2.1 (40)	-1.8 (60)	-1.9 (100)
CESM1(CAM5)	Land	-2.4 (7)	-0.2 (7)	-1.1 (14)
	Ocean	-4.0 (38)	-1.8 (48)	-2.8 (86)
	Global	-3.8 (45)	-1.6 (55)	-1.7 (100)

Table 4.3: Annual mean DRE (W m^{-2}) over the southeastern Pacific Ocean (35° - 5° S, 130° - 65° W) from 2B-FLXHR-LIDAR and CESM1(CAM5) datasets. The fractional occurrence for each category is shown in parentheses.

Dataset	Surface	Clear-sky		Cloudy-sky		All-sky	
		Mean	σ	Mean	σ	Mean	σ
2B-FLXHR-LIDAR	Land	-3.2 (18)	2.5	-3.2 (18)	2.5	-3.2 (18)	2.5
	Ocean	-2.9 (17)	0.9	-2.9 (17)	0.9	-2.9 (17)	0.9
	Global	-3.1 (35)	1.9	-3.1 (35)	1.9	-3.1 (35)	1.9
CESM1(CAM5)	Land	-3.5 (18)	1.4	-3.5 (18)	1.4	-3.5 (18)	1.4
	Ocean	-5.8 (27)	0.6	-5.8 (27)	0.6	-5.8 (27)	0.6
	Global	-4.9 (45)	1.5	-4.9 (45)	1.5	-4.9 (45)	1.5

Table 4.4: Annual mean DRE (W m^{-2}) over the southeastern Atlantic Ocean (25°S - 0° , 10°W - 30°E) from 2B-FLXHR-LIDAR and CESM1(CAM5) datasets. The fractional occurrence for each category is shown in parentheses. The standard deviations, σ , of the 2.5° -binned estimates are also reported.

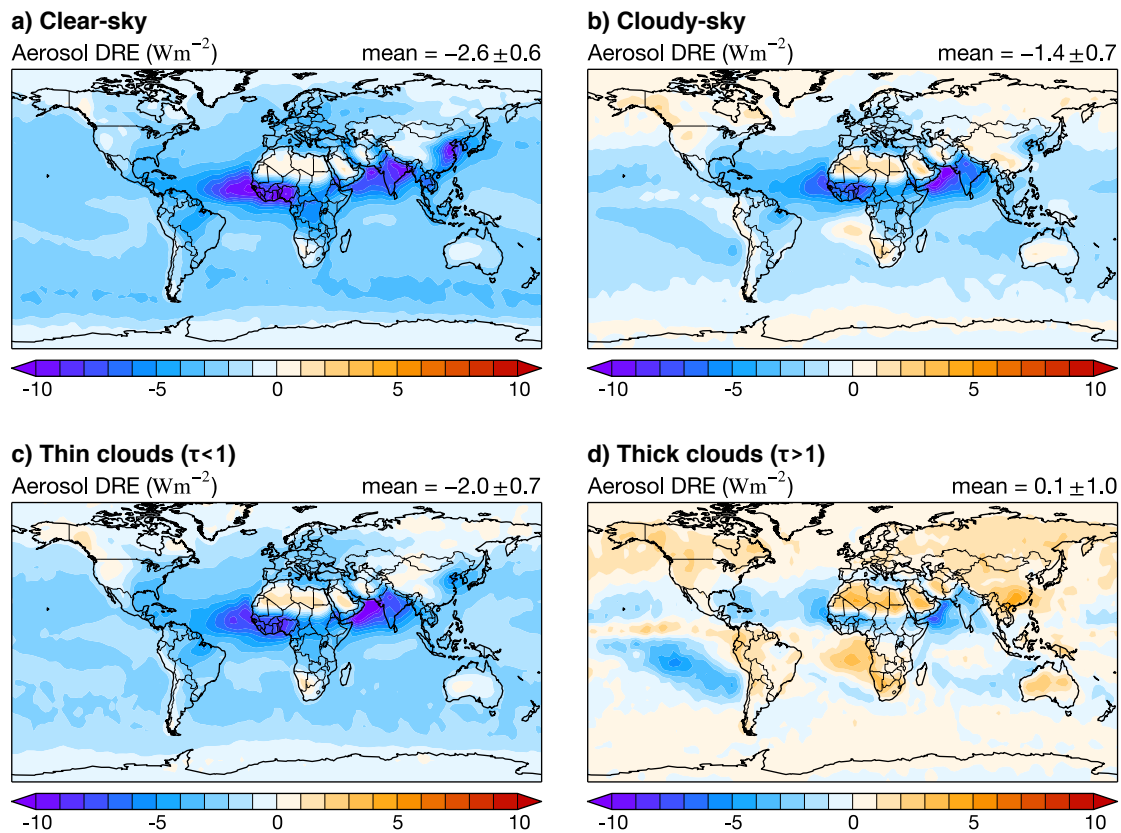


Figure 4.1: Maps of annual mean DRE from 2B-FLXHR-LIDAR, as partitioned by sky conditions. The global mean and uncertainty are displayed in the top-right corner of each panel.

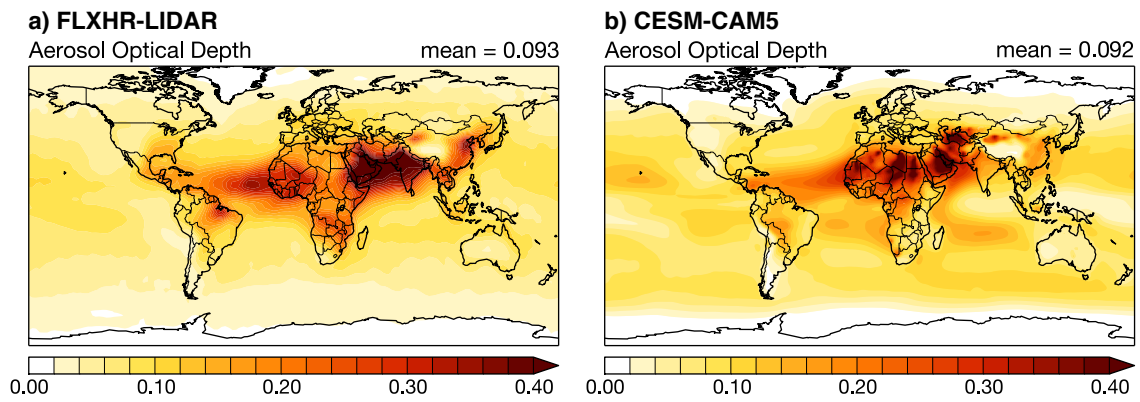


Figure 4.2: Maps of annual mean AOD (a) observed by CALIPSO and (b) simulated in CESM1(CAM5). The global mean is displayed in the top-right corner of each panel.

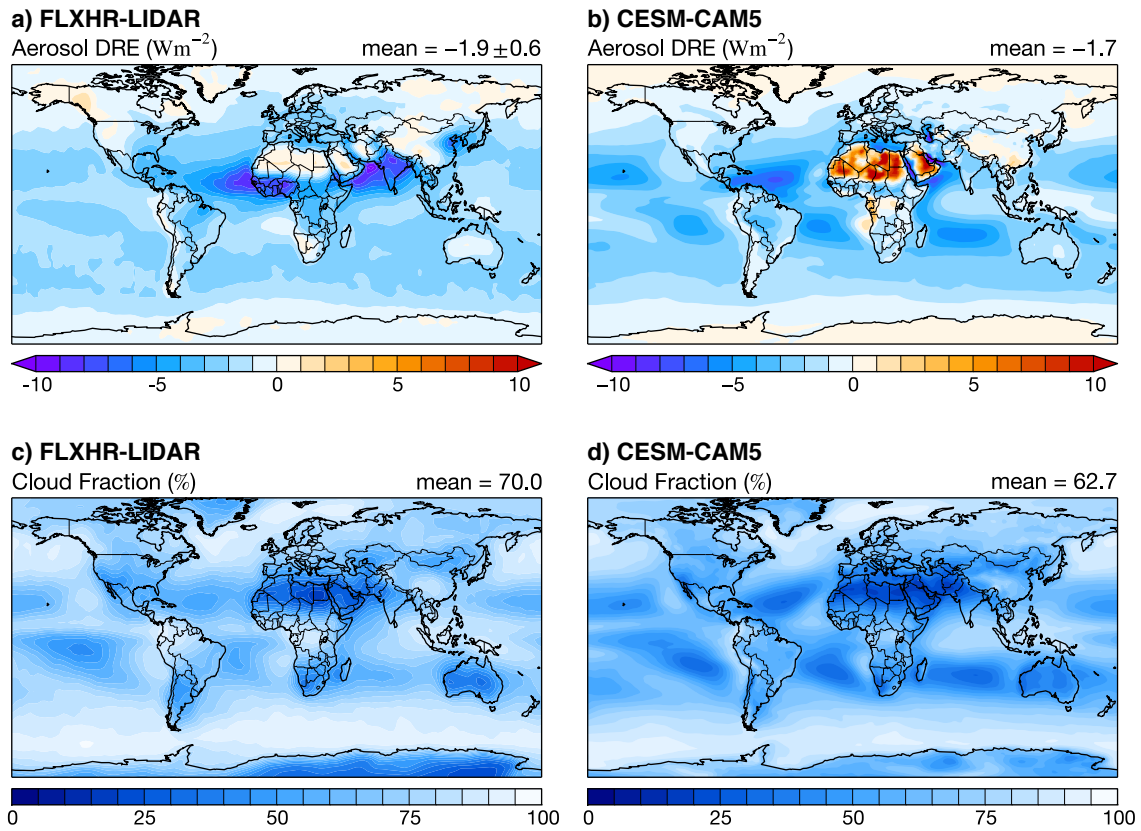


Figure 4.3: Annual mean all-sky DRE and total cloud fraction from (left) 2B-FLXHR-LIDAR and (right) CESM1(CAM5) datasets. Note that brighter shading corresponds to higher cloud fraction. The global mean is displayed in the top-right corner of each panel.

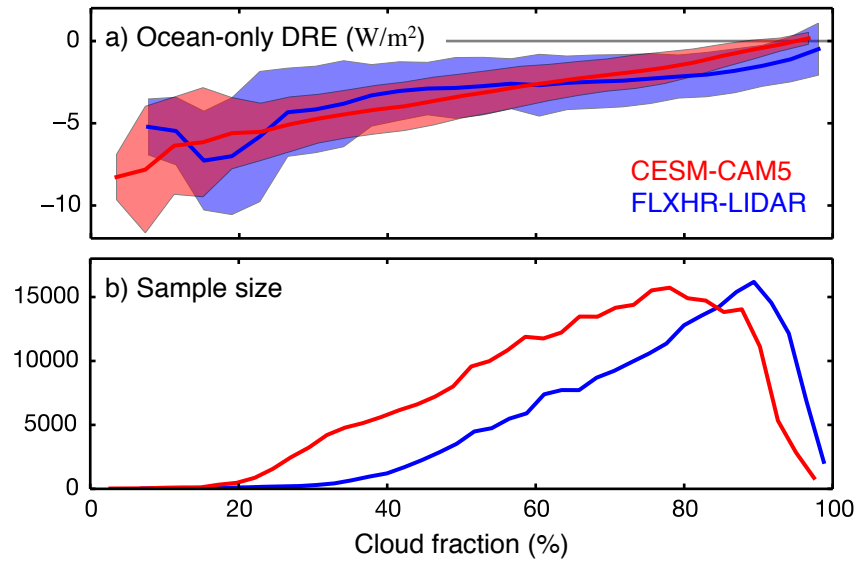


Figure 4.4: Observed and simulated probability density functions of the global (a) ocean-only all-sky DRE and (b) sample counts expressed as a function of cloud fraction. Estimates of monthly mean DRE and cloud fraction are evaluated at 2.5° resolution over a 5-year time period for both 2B-FLXHR-LIDAR (2006-2011) and CESM1(CAM5) (2000-2005).

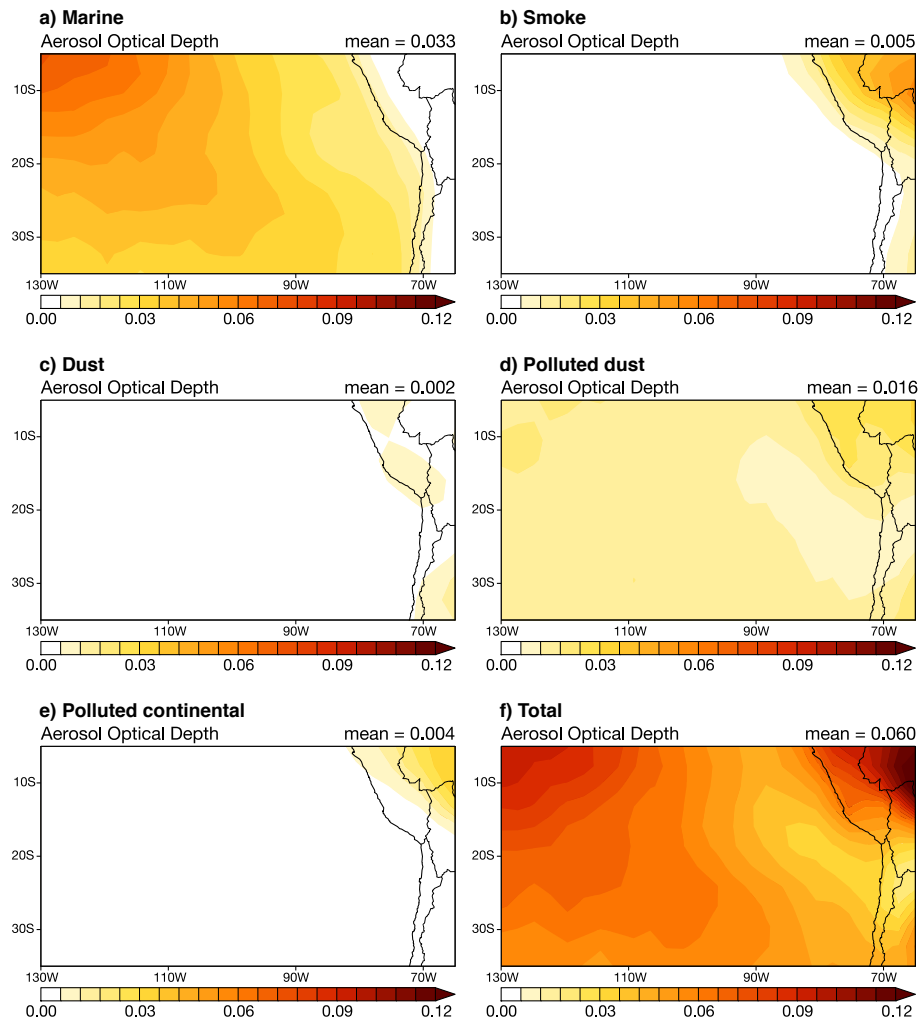


Figure 4.5: Maps of annual mean AOD over the southeastern Pacific Ocean (35°-5°S, 130°-65°W) as separated by CALIPSO aerosol types. The area-weighted mean is displayed in the top-right corner of each panel.

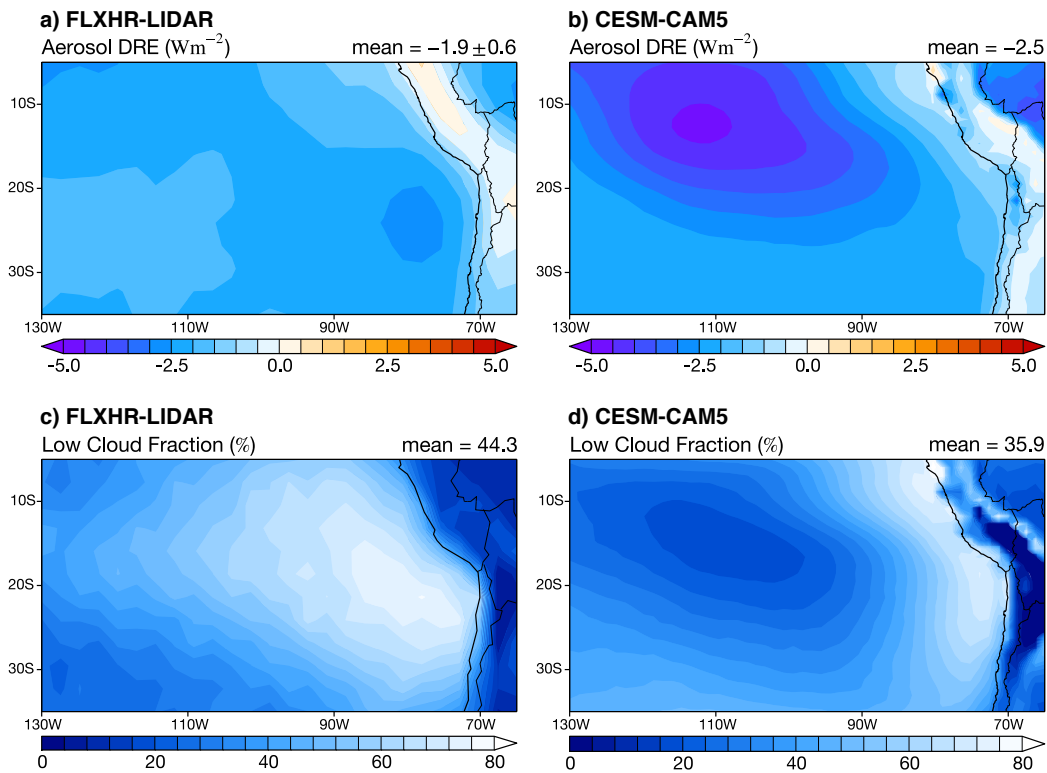


Figure 4.6: Annual mean DRE and low cloud fraction over the southeastern Pacific Ocean (35°-5°S, 130°-65°W) from (left column) 2B-FLXHR-LIDAR and (right column) CESM1(CAM5) datasets. Note that brighter shading corresponds to higher cloud fraction. Low clouds are defined as those with cloud-top temperatures above 0°C. The area-weighted mean is displayed in the top-right corner of each panel.

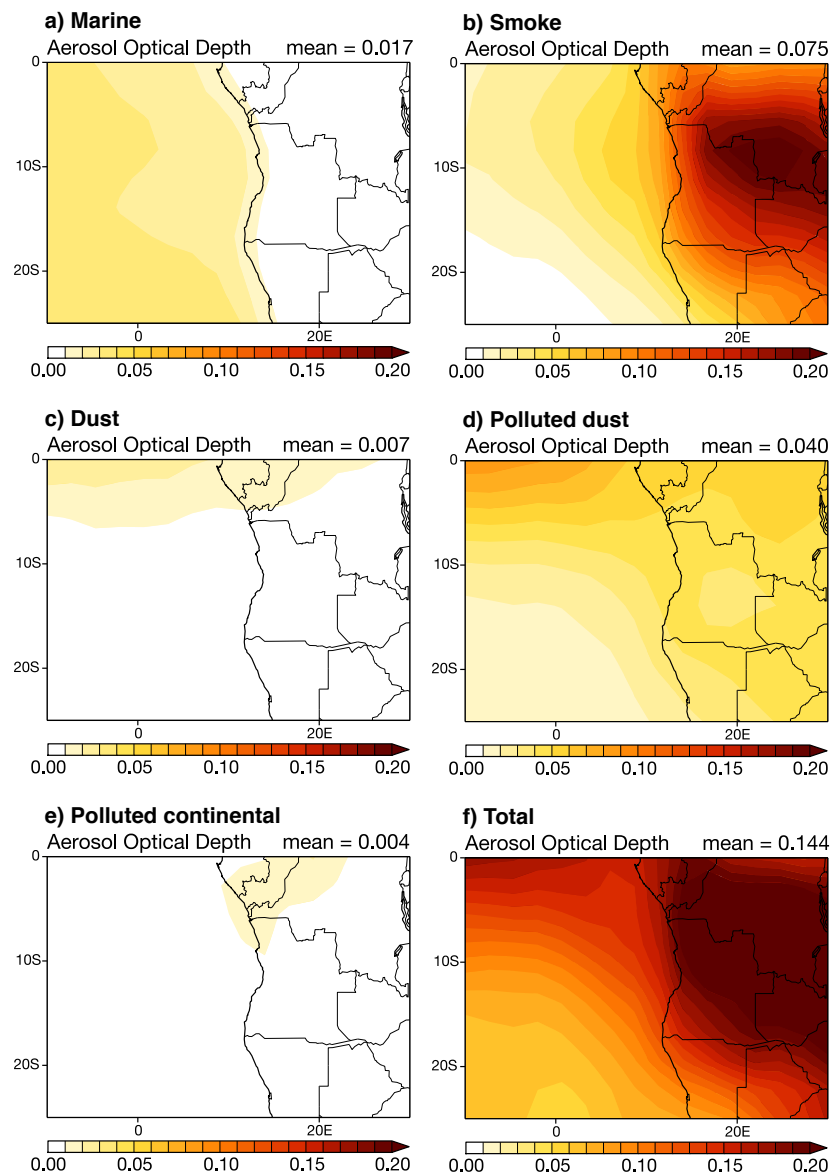


Figure 4.7: Maps of annual mean CALIPSO AOD over the southeastern Atlantic Ocean (25°S - 0° , 10°W - 30°E) as partitioned by CALIPSO aerosol types. The area-weighted mean is displayed in the top-right corner of each panel.

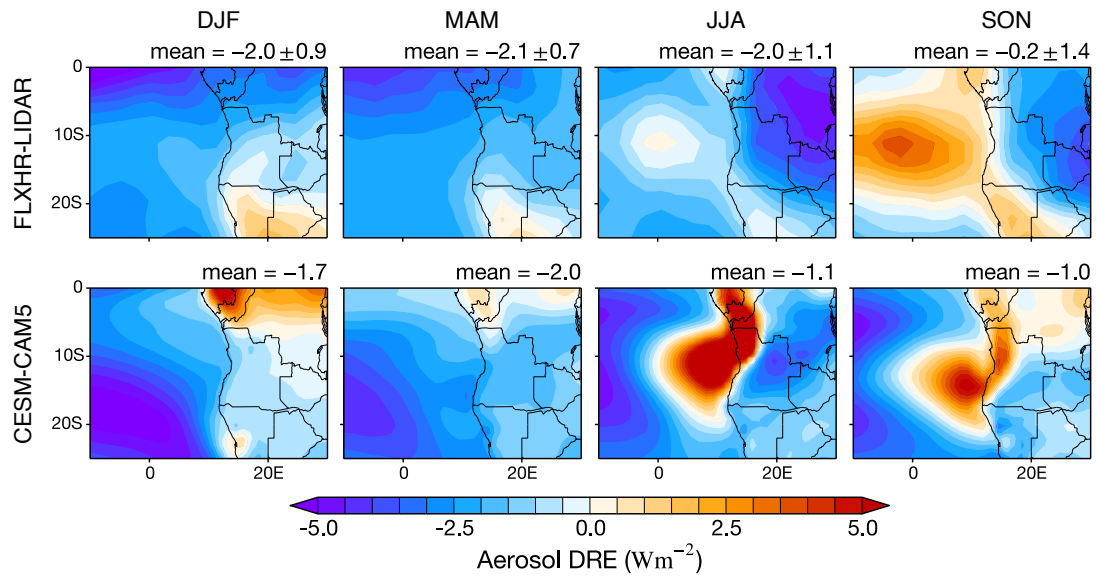


Figure 4.8: Maps of seasonal mean DRE over the southeastern Atlantic Ocean (25°S-0°, 10°W-30°E) from (top) 2B-FLXHR-LIDAR and (bottom) CESM1(CAM5) datasets. The area-weighted mean is displayed in the top-right corner of each panel.

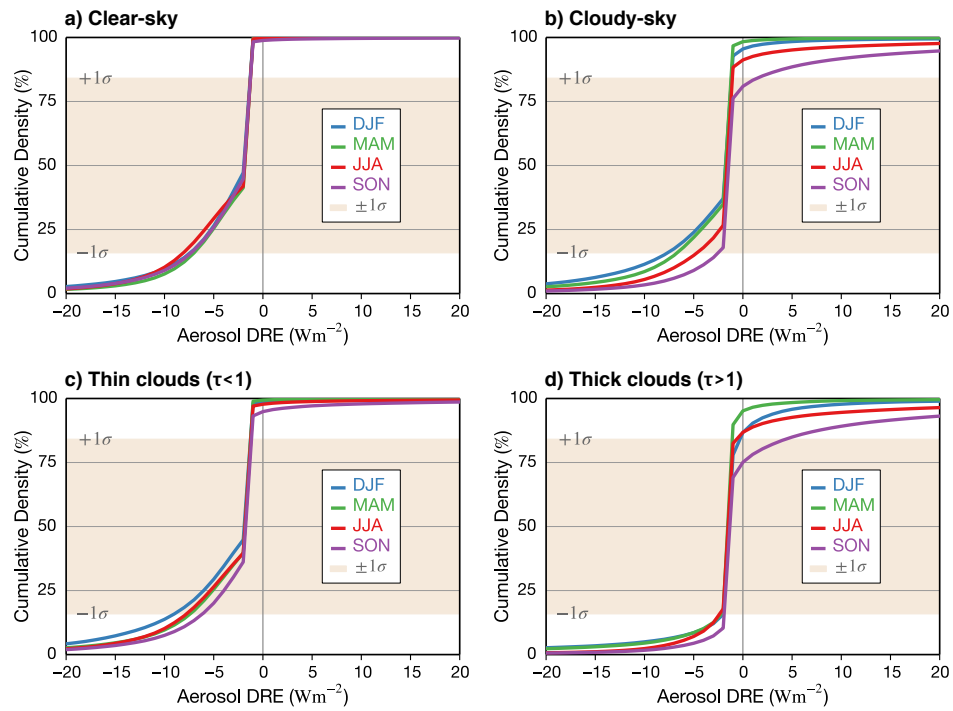


Figure 4.9: Cumulative density functions of seasonal mean DRE in the southeastern Atlantic Ocean (25°S - 0° , 10°W - 30°E) as sorted by sky conditions from the 2B-FLXHR-LIDAR dataset. The beige shading shows the spread within one standard deviation of the median.

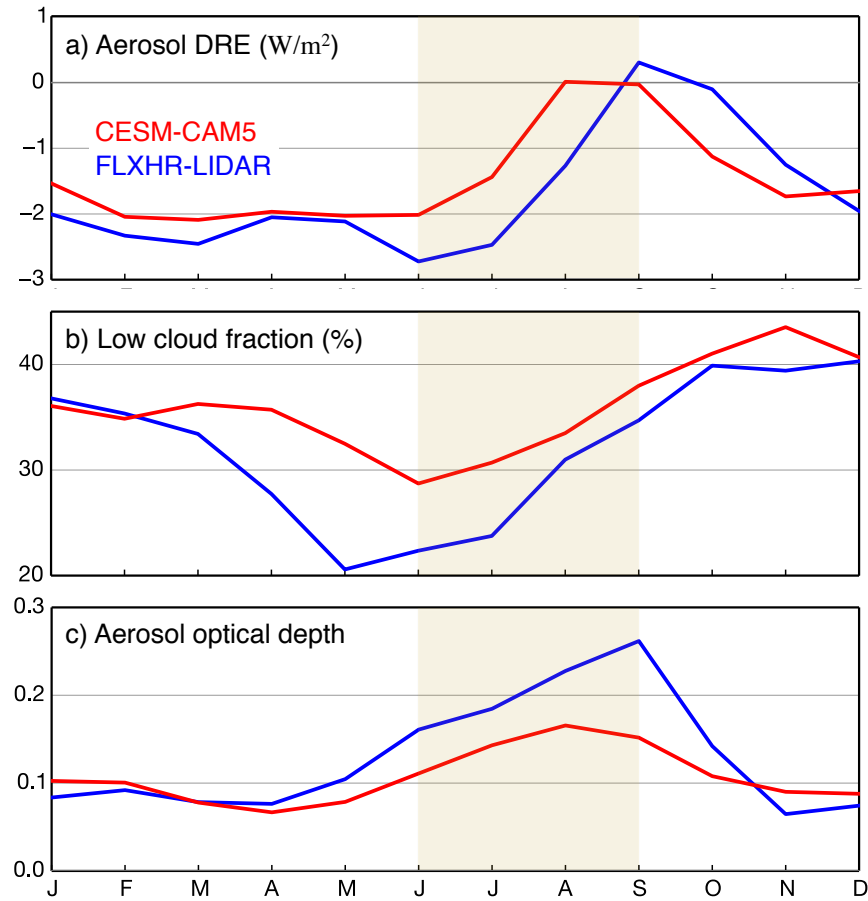


Figure 4.10: Monthly mean (a) all-sky DRE, (b) low cloud fraction, and (c) AOD over the southeastern Atlantic Ocean (25°S-0°, 10°W-30°E) from the 2B-FLXHR-LIDAR (blue) and CESM1(CAM5) (red) datasets. The JJA period is shaded in beige to highlight the onset of the biomass burning season.

Chapter 5

The Self-lofting of Aerosols by Solar Radiative Heating

5.1 Overview

It has been demonstrated in the previous section that some aerosols play an important role in heating the atmosphere through the absorption of solar radiation. Given the importance of radiative heating for modulating instability, circulations, clouds, and precipitation, this section will explore the unique capabilities of new active satellite measurements for assessing the vertical distribution of aerosol radiative heating. In particular, special attention will be given to documenting the annual cycle and radiative impacts of smoke aerosols. Approximately 80% of all biomass burning occurs in the tropics with 440 million hectares of land burned annually, and some of the most extensive fires occur on the African continent (Scholes and Andeae, 2000). This section will test the hypothesis that the radiative heating from African biomass aerosols is sufficiently strong for aerosol layers to be self-lofted in the atmosphere. The southeastern Atlantic Ocean is the perfect natural laboratory to test this hypothesis. The phenomenon of self-lofting has been theorized to exist using radiative transfer modeling (Malone et al., 1986; Radke et al., 1990; Boers et al., 2010), however evidence of self-lofting aerosols over this region has not been comprehensively documented using observations. The 2B-FLXHR-LIDAR dataset is well suited for performing this analysis since aerosol heating rates are evaluated at discrete height levels to provide information on the vertical structure of shortwave heating within the atmospheric column.

The two types of aerosols that absorb visible light are mineral dust and carbonaceous aerosols (Chin et al., 2009). The Sahara desert is the largest source of mineral dust globally and Saharan dust is typically composed of many elements including Si, Al, Ca, Na, K, Ca, and Fe according to aircraft measurements from the Saharan Dust Experiment (SHADE) in the Cape Verde region during September 2000 (Formenti et al., 2003). Mineral dust containing iron in the form of Fe_2O_3 (hematite) is particularly absorbing in the shortwave, as this compound is the most efficient light absorber at visible wavelengths among the minerals found in the Sahara (Sokolik and Toon, 1996). The mass absorption cross section of Saharan dust has been measured at $3.5 \text{ m}^2\text{g}^{-1}$ at 550 nm (Linke et al.,

2006), while Asian dust is considerably less absorbing at $0.009 \text{ m}^2\text{g}^{-1}$ at 550 nm (Clarke et al., 2004). Dust particles are considerably less absorbing than black carbon, although its total absorption can be significant owing to the relatively high abundance of dust particles globally in the troposphere (Sokolik and Toon, 1996). The incomplete combustion of fossil fuels and biomass matter produces carbonaceous aerosols. If combustion is sufficiently hot and has sufficient oxygen no carbon particles are produced; otherwise, carbonaceous aerosols are emitted. Aerosols containing carbon have unique properties that make these particles strong absorbers in the visible spectrum. Carbonaceous aerosols including black carbon, brown carbon, and organic carbon are emitted as a byproduct of burning fossil fuels, solid fuels, and biomass fuels. Organic carbon refers to carbonaceous aerosols containing hydrogen and sometimes oxygen and is weakly absorbing (Bond et al., 2013). Brown carbon refers a complex mixture of organic compounds and is observed to have a visible light absorption of less than $1 \text{ m}^2\text{g}^{-1}$ at 550 nm (Kirchstetter et al., 2004). Black carbon is produced by the incomplete combustion of carbon-based fuels with low levels of oxygen and is a strong absorber in the shortwave with a visible light absorption of at least $5 \text{ m}^2\text{g}^{-1}$ at 550 nm (Bond and Bergstrom, 2006).

Pure black carbon rarely exists in the atmosphere as these particles often mix with other aerosol components in their lifetime. Freshly emitted black carbon aerosols are generally small and hydrophobic; however, the aging of these particles after emission tends to increase their size and hygroscopicity over time. Upon formation, black carbon particles begin as wrinkled graphite layers forming a shell around a hollow interior (Heidenreich et al., 1968). Soon after formation, these graphitic spherules aggregate to form fractal chain-like structures consisting of hundreds of spherules (Medalia and Heckman, 1969). Over time, water vapor and other gas phase species (e.g. sulfuric acid and secondary organic vapor) condense upon the aggregates collapsing the chain-like structures into densely packed clusters (Huang et al., 1994; Ramachandran and Reist, 1995). This aging process changes the optical properties of black carbon that, for freshly emitted particles, is observed to have a mass absorption cross section of $7.5 \pm 1.2 \text{ m}^2\text{g}^{-1}$ at 550 nm and a mass absorption cross section approximately 50% larger for aged particles internally mixed with other aerosol chemical components (Bond et al., 2013). According to global aerosol model simulations, it is predicted that most black carbon becomes mixed with other substances within 1 to 5 days after emission (Jacobson, 2001a). The

timescale for converting hydrophobic black carbon to its hydrophilic form is typically around 1 day (Koch et al., 209b).

A strong motivation behind this study is the fact that black carbon aerosols produced from biomass burning in Africa are observed thousands of kilometers from the western coast of Africa. In fact, the southeast Atlantic is a region where models show significant disagreement in simulations of aerosol radiative forcing according to the AeroCom multi-model inter-comparison study (Shultz et al., 2006). The high uncertainty over this region is attributed to the aerosols emitted from biomass burning. During the biomass burning season of August through October, human-caused fires for agricultural clearing produces large quantities of smoke aerosols over central Africa. These plumes of smoke are transported westward by the prevailing winds over the southeast Atlantic Ocean. This seasonal cycle in biomass burning creates a seasonal cycle in aerosol direct effects, as shown in Figure 5.1. During September when the smoke AOD reaches its peak, the 2B-FLXHR-LIDAR aerosol DRE is observed to flip from negative to positive, suggesting strong absorption from smoke particles over this region. Smoke originating from Africa has even been observed as far away as the Caribbean and North America. The exact mechanism responsible for transporting these aerosols across the Atlantic Ocean is largely unknown. In general, the long-range transport of smoke particles within the boundary layer is not efficient due to the turbulent nature of the atmospheric boundary layer (de Laat et al., 2012). Under favorable meteorological conditions (e.g. strong winds and dry air) smoke aerosols near the surface may be lifted to higher altitudes in the atmosphere. Once lifted out of the atmospheric boundary layer into the troposphere, these aerosols may be transported distances of 1000 km or more (Shindell et al., 2008).

It is hypothesized that radiative heating plays an important role in keeping these aerosols elevated in the atmosphere at heights where they may be transported westward by prevailing winds over the southeast Atlantic Ocean. Aerosol absorption occurs over regions as well. For example, agricultural fires in Indonesia have been shown to produce large amounts of smoke during their biomass burning season. In addition, smoke particles originating from Canadian fires have also been observed over the Greenland ice sheets. Given that aerosols over reflective snow and ice surfaces similarly enhance the absorption of solar radiation, the Arctic is an area of interest that has been investigated extensively in recent years. While much attention has been given toward the radiative heating of aerosols over snow,

less attention has been devoted toward understanding the solar heating of aerosols over clouds. Given the relative scarcity of aerosols over polar regions and higher prevalence of clouds than snow-covered surfaces, the topic of above cloud aerosol (ACA) heating deserves further investigation.

5.2 Methodology

To quantitatively evaluate the ability of aerosol to self-loft by solar heating, this study uses radiative flux data from the 2B-FLXHR-LIDAR dataset to calculate the shortwave heating rates of aerosols. Radiative heating rates are computed at 125 vertical levels using 2B-FLXHR-LIDAR data from 2007-2010. The contribution of radiative heating from smoke aerosols is evaluated using the aerosol type classification from CALIPSO. The shortwave heating rates are used to diagnose the vertical motion using a generalized form of the quasi-geostrophic thermodynamic equation (eq. 6.13a in Holton, 2004):

$$\left(\frac{\partial}{\partial t} + \vec{v}_g \cdot \vec{\nabla} \right) T - \left(\frac{\sigma p}{R_d} \right) \omega = \frac{1}{c_p} \left(\frac{dQ}{dt} \right) \quad (4)$$

where the static stability $\sigma \approx 2.5 \times 10^{-6} \text{ m}^2 \text{ Pa}^{-2} \text{ s}^{-2}$ in the mid-troposphere and temperature T represents the temperature deviation from the basic state (Holton, 2004). Assuming no temperature advection and expanding the diabatic heating term, the quasi-geostrophic thermodynamic equation is simplified as follows:

$$-\left(\frac{\sigma p}{R_d} \right) \omega = \frac{1}{c_p} \left(\frac{c_p dT}{dt} - \frac{1}{\rho} \frac{dp}{dt} \right) \quad (5)$$

As a first-order approximation, it may be assumed that the diabatic heating goes entirely toward changing the environmental temperature without changing atmospheric pressure. This approximation provides an upper bound estimate for the vertical motion resulting from aerosol solar heating. The equation is then separated into aerosol and non-aerosol components. The change in omega (aerosol minus non-aerosol) is therefore described as the following:

$$\Delta\omega \approx \frac{-R_d}{\sigma p} \left(\frac{dT_{aero}}{dt} \right) \quad (6)$$

This simplified form of the quasi-geostrophic omega equation provides a conservative, upper bound estimate of vertical motion due to diabatic heating. It assumes a dry environment with no horizontal advection over long timescales, which are reasonable approximations for the mid-troposphere over the southeastern Atlantic Ocean. This relationship indicates that the temperature increase associated with diabatic heating leads to ascent ($\omega < 0$) of that parcel of air. This computed omega is compared with the coincident estimate of large-scale subsidence obtained from the Modern-Era Retrospective analysis for Research and Applications (MERRA) reanalysis data product (Rienecker et al., 2011) collocated at the same vertical resolution as 2B-FLXHR-LIDAR. If the aerosol-induced omega exceeds the MERRA-reanalysis omega, it can be assumed that the upward vertical motion from aerosols exceeds the downward vertical motion from large-scale subsidence and aerosol self-lofting is considered plausible under these conditions.

5.4 Aerosol heating rates

To demonstrate the importance of aerosol absorption over the southeast Atlantic, it is worthwhile to explore the global distribution of aerosol heating. The three-dimensional global annual distributions of aerosol heating rates and related meteorological fields are shown in Figure 5.2. Figure 5.2a displays the annual mean aerosol shortwave heating rates from 2B-FLXHR-LIDAR. The aerosol type with the strongest overall radiative heating is smoke, shown in Figure 5.2b, which indicates a maximum annual heating rate of 0.2 K/day over south-central Africa. Dust is another aerosol type with a substantial shortwave heating, although the heating from dust is primarily in the northern hemisphere while heating from smoke is primarily in the southern hemisphere. Dust heating rates peak in JJA over northern Africa, whereas smoke heating rates peak in SON over southern Africa. Figure 5.2c shows the annual mean omega vertical velocity from MERRA reanalysis data. Rising air predominates in the tropical troposphere, whereas subsiding air predominates in the subtropical troposphere. Finally, the annual mean planetary boundary layer (PBL) height is displayed in Figure 5.2d, indicating that over

the southeast Atlantic Ocean, the PBL increases from around 600 m at the coast to 1000 m further offshore. This result is important to note since aerosols are known to affect the PBL and be affected by the PBL. It has been theorized that an aerosol layer can lower the PBL height by heating the PBL and cooling the surface, thereby stabilizing the atmospheric layer (Zhou et al., 2017).

To further illustrate the radiative impact of biomass burning over southern Africa, Figure 5.3 shows the September-November smoke heating rates at three height levels. Aerosol heating rates are shown to increase with height in the lower troposphere, similar to the vertical distribution of aerosols over this region. Smoke aerosols are transported by wind westward over the Atlantic Ocean where shortwave heating rates over 1 K/day are observed 3 to 5 km above the surface. The peak shortwave heating over ocean is observed at an altitude of 4 km. At these height levels it is hypothesized that aerosol heating may be sufficiently strong for the aerosol layer to remain elevated despite its location over an area of subsidence. The estimated uncertainty in 2B-FLXHR-LIDAR aerosol heating rate is shown in Figure 5.4. The uncertainty in aerosol heating rate is computed by perturbing radiative fluxes over a range of possible values of single scattering albedo. Based on Figure 5.4, the uncertainty in aerosol heating rate is most significant over tropical regions where smoke and dust emissions are greatest. Figure 5.4 indicates an upper limit on the uncertainty over this region of approximately 0.3 K/day. Therefore, this analysis estimates that the peak aerosol heating over the southeast Atlantic Ocean occurs off the coast of Angola at a height of 4 km and is estimated to be 0.6 ± 0.3 K/day.

Given the sensitivity of radiative fluxes to aerosol optical properties, an accurate assessment of aerosol heating requires aerosol optical properties representative of the particles in the atmosphere. Aerosol properties have been studied extensively in laboratory, field campaign, and modeling efforts, it is quite challenging to extend these properties to all aerosols globally in the atmosphere. The Aerosol Robotic Network (AERONET) observing network is widely recognized as one of the best sources of aerosol measurements with around 200 sites globally and data from AERONET is used to improve the characterization of aerosol properties in 2B-FLXHR-LIDAR. The 2B-FLXHR-LIDAR product has benefited from an improved characterization of aerosol properties in the new Release 05 algorithm. The prescribed values of single scattering albedo for smoke aerosols in 2B-FLXHR-LIDAR are biased low compared to surface measurements obtained from the AERONET aerosol observing network. This low bias in single scattering albedo resulted in excessive aerosol absorption

of shortwave radiation in previous versions of 2B-FLXHR-LIDAR. In addition to the other significant improvements implemented in the Release 05 2B-FLXHR-LIDAR, including a better representation of surface albedo and ice cloud properties, a correction has been made in the algorithm to make the optical properties of smoke more consistent with surface measurements. The analysis of radiative heating rates will be performed using the corrected aerosol properties in the latest release of 2B-FLXHR-LIDAR. These algorithm improvements are expected to improve our understanding of aerosol heating over the southeast Atlantic and elsewhere, as well as quantitatively evaluate the possibility of self-lofting aerosols.

5.4 Potential for self-lofting aerosols

Aerosol layers with a mid-visible single scattering albedo less than 1.0 heat the surrounding air through the absorption of solar radiation (Radke et al., 1990). The lower the single scattering albedo, the greater the potential for solar heating. This solar heating may be enhanced if the aerosol layer resides above a brighter surface (e.g. deserts and ice sheets) or an optically thick cloud. Of all the constituents found in aerosols, black carbon emitted by combustion has the greatest efficiency for absorbing light with a mass absorption cross section exceeding $5 \text{ m}^2\text{g}^{-1}$ at 550 nm (Bond et al., 2013). As previously shown in Figure 5.2, the radiative heating rates of aerosols can reach 0.2 K/day on the annual mean. On an instantaneous basis, however, aerosol heating rates can exceed 1 Kelvin per day. To put this value in context, the mean lower tropospheric cooling rate has been estimated using various observational techniques to be around 1 K/day (Haynes et al., 2012). However, it is still unknown whether the shortwave heating from aerosol absorption is sufficient for self-lofting aerosols in the troposphere. Furthermore, it is not fully understood if there are regions where conditions are favorable for self-lofting on timescales of a month, season, or year. This study will investigate the characteristics of aerosol absorption over the southeast Atlantic using a novel satellite-based approach.

First, this analysis explores if aerosol self-lofting is indeed possible on annual, seasonal, or monthly timescales. To perform this analysis, aerosol vertical velocity is computed using SW heating rates from 2B-FLXHR-LIDAR. The aerosol vertical velocity is compared against the background environmental vertical velocity from MERRA. If the aerosol vertical velocity exceeds the opposing environmental vertical velocity, then aerosol self-lofting is considered plausible. Figure 5.5 shows the

profiles of vertical velocity over the southeast Atlantic Ocean (0°S - 20°S , 10°W - 10°E). Vertical velocity from (blue) MERRA reanalysis, (red) 2B-FLXHR-LIDAR aerosol heating, and (black) the combination of both are shown. Aerosol vertical velocity reaches a maximum at a height of 4 km above sea level. The annual average upward motion is around 2 mb/day, although this increases to nearly 10 mb/day during the peak biomass burning month of September. While the vertical velocity from aerosols is strongest during September, it is still considerably weaker than the predominant subsidence observed over this region. In fact, the aerosol ascent at 4 km is only 50% as strong as the downward motion from subsidence. Overall, the aerosol radiative heating is likely insufficient to keep the aerosol layer aloft on timescales of a month or longer. In summary, aerosols in the southeast Atlantic Ocean are estimated to suppress subsidence by about 10% annually, 20% in SON, and 50% in September.

It is important to note that the regional distribution of heating depends on the seasonal cycle of biomass burning. Figure 5.6 indicates that the areal extent of heating over the southeast Atlantic Ocean varies greatly by time year. On the annual mean, aerosol heating rates greater than 0.05 K/day are found predominantly east of the prime meridian at 0° . During SON, however, the extent of heating expands westward to 15°W . During September the aerosol heating reaches 20°W , which extends more than halfway across the ocean to the eastern coast of Brazil. Consistent with Figure 5.5, aerosol heating peaks during September when biomass burning in south-central Africa reaches a maximum. The upward vertical motion of the aerosol layer can counter as much as half of the subsidence, allowing the aerosols to remain suspended in the atmosphere for a longer period of time. As a result, smoke plumes originating in Africa may be transported for a longer time and a longer distance over the Atlantic Ocean because these aerosols absorb solar radiation.

Aerosol heating rates averaged over September can reach 1 K/day, however, for individual events the instantaneous aerosol heating rates can be much larger. As an example, Figure 5.7 displays a vertical profile over the tropical Atlantic Ocean on September 2, 2009. The satellite overpass shows a particularly interesting scene in which CALIPSO identified a smoke layer residing above cloud deck, according to the 2B-FLXHR-LIDAR-AUX product. The smoke layer is found at an altitude of 4 km and the cloud is 1 km above the ocean surface. In the center panel of Figure 5.7, the shortwave aerosol heating rate is computed using radiative flux calculations from 2B-FLXHR-LIDAR. Here, the heating

rates for the smoke layer reach as high as 10 K/day. In the bottom panel of Figure 5.7, the net aerosol vertical velocity is diagnosed using the 2B-FLXHR-LIDAR aerosol heating rates and subtracting subsidence from MERRA reanalysis data. The smoke layer is estimated to have a vertical ascent of 50 mb/day, although some areas indicate a vertical velocity of up to 100 mb/day. There is further evidence of self-lofting in the next CALIPSO overpass 90 minutes later that shows a smoke aerosol layer at the same altitude (3-5 km) almost certainly from the same smoke plume. Considering the remote location of this observation, it is very likely that this smoke layer also originated from central Africa meaning it had been transported over 1000 km from its source. In this example, an aerosol layer is identified and estimated to have a vertical ascent of 50 mb/day, or approximately 0.5 km/day. Assuming a constant rate of ascent, the aerosol layer may be lifted as much as 1.5 km over 3 days.

It is worthwhile to compare these estimates of aerosol self-lofting with results from previous studies. While there are no satellite-based estimates by which to compare, there are a few model simulations that have investigated this topic. Modeling studies have explored the potential of lifting aerosol layers by solar heating. For optical properties typical of biomass burning, aerosol layers may be lifted by 3-5 km over 3 days. It is estimated in this study that the aerosol layer may be lifted to the tropical tropopause within 3-4 days (Boers et al., 2010). Furthermore, de Laat et al. 2012 used a one-dimensional radiative transfer model to calculate that a smoke plume from the 2009 Australian bushfires could rise 16-18 km over 5 days. This estimate was consistent with observational evidence that the smoke plume had reached at altitude between 15-20 km within 3 days of the fire. On annual and seasonal time scales aerosol ω is about a factor of 10 too weak to overcome subsidence, however there is evidence to support that individual burning episodes could produce aerosol heating rates sufficiently strong for self-lofting aerosol layers.

The ideal conditions for solar heating aerosol layers are the following:

- Optically thick aerosol layer ($\tau > 1$)
- Absorbing aerosol layer ($SSA < 0.9$)
- Large particle size (more absorption but also more sedimentation)
- Dry atmosphere (low humidity)
- Bright underlying surface (cloud, desert, or snow/ice)
- Summer hemisphere at high latitudes (more available solar energy)

Biomass burning in central Africa is an important driver of climate due to its large release of black carbon aerosols into the atmosphere. Around 80% of all biomass burning occurs in the tropics (Scholes and Andeae, 2000) and African fires are responsible for an estimated 30 to 50%, making Africa the single large source of biomass burning each year (Andreae, 1991). However, it is also important to consider fires in extratropical regions. For example, bushfires near Melbourne, Australia (37.8°S, 145.0°E) on 7 February 2009 produced a smoke plume that within 3 days was observed at altitudes between 15 and 20 km and thousands of kilometers from its source. There is observational evidence to suggest that the rise of this smoke plume above 10 km altitude has been attributable to the absorption of solar radiation and subsequent self-lofting (de Laat et al., 2011). This result is consistent with Boers et al., 2010 that found that most absorption of available solar radiation takes place in the summer hemisphere at high latitudes. In a simple modeling exercise, they simulated a biomass aerosol layer with typical optical properties ($SSA = 0.75$, $\tau = 1.75$, $\alpha = 1.50$), as shown in Figure 5.9. If a cross-latitudinal flow of 5 degrees per day is allowed, the aerosol layer doubled in height gain from 3.4 km to 6.8 km altitude due to a combination of isentropic flow and solar heating. Therefore, the poleward transport of aerosols could be an important mechanism for lifting aerosols to higher altitudes (Boers et al., 2010). While fires at higher latitudes are relatively less frequent than in the tropics, high-latitude smoke aerosol layers may have a greater potential for reaching tropopause levels owing to longer days and greater solar absorption.

5.5 Chapter summary

A unique characteristic of the 2B-FLXHR-LIDAR dataset is that retrieved aerosol properties are vertically resolved as opposed to column-integrated as is more common in satellite products. This vertically resolved aerosol information makes it possible to investigate the aerosol radiative impacts not only at the top-of-atmosphere, but also within the atmospheric column at various levels of interest. This is important to consider since at various levels in the atmosphere aerosols modulate energy flows by absorbing solar radiation. This vertically resolved aerosol information also makes it possible to investigate science questions difficult or impossible to address using conventional passive sensors. In particular, aerosol retrievals over bright land and cloudy scenes are now possible by leveraging the active remote sensing capabilities of spaceborne lidar.

As such, this study tests the following hypotheses:

1. Solar-heated aerosol layers may warm the surrounding air sufficiently to overcome large-scale subsidence and remain self-lofted.
2. Aerosol heating and transport over ocean will be greatest over scenes where it is most cloudy.

It has been demonstrated in this study that clouds enhance the solar absorption of overlying biomass burning aerosol layers. The southeast Atlantic Ocean is the perfect natural laboratory for observing these phenomena due to the presence of near persistent marine stratocumulus cloud decks. Aerosol-radiation interactions are especially important over this region because the presence of these low-lying clouds provides a mechanism for heating in an environment dominated by subsidence. The presence of clouds has been shown to boost aerosol absorption by around 50%. Furthermore, this study has presented evidence to support that layers of smoke over the southeast Atlantic Ocean provide sufficient heating to self-loft aerosol layers during intense biomass burning episodes. This finding has important implications for not only for the redistribution of heat and self-stabilizing the atmosphere but also for the long-range transport of aerosol across ocean.

Aerosol type	Lidar ratio at 532 nm	Lidar ratio at 1064 nm
Marine	20	45
Dust	40	55
Polluted continental	70	30
Clean continental	35	30
Polluted dust	65	30
Smoke	70	40

Table 5.1: Each CALIPSO aerosol type is assigned a lidar ratio representing the fraction of extinction to backscatter signal. The lidar ratio is determined based on a cluster analysis of AERONET observations and are used to retrieve extinction profiles for each CALIPSO overpass (Omar et al., 2009).

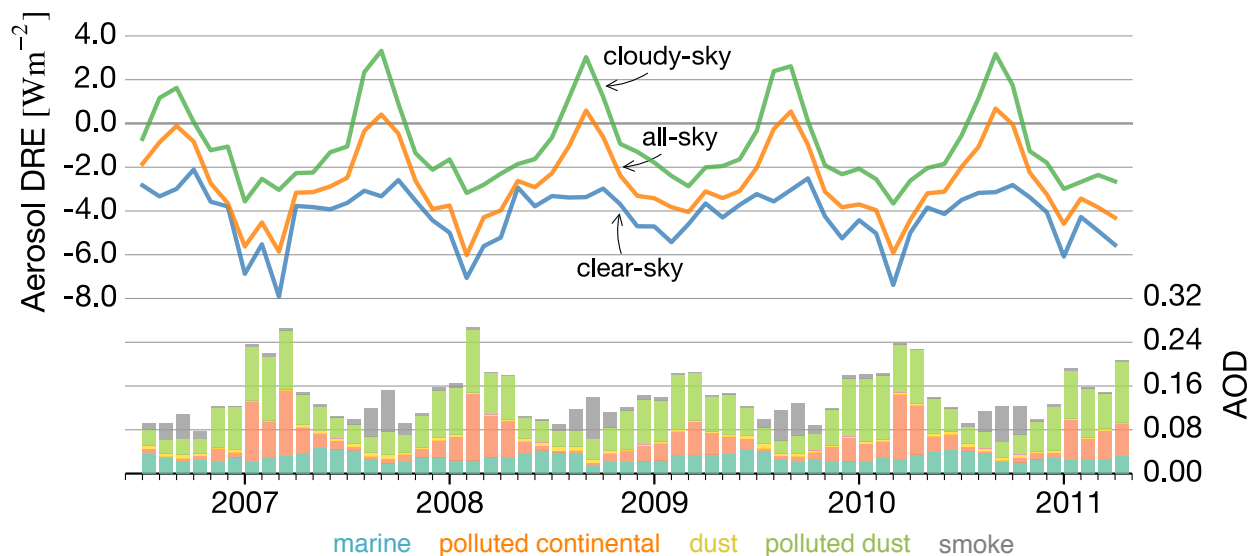


Figure 5.1: Time series of monthly mean (top) 2B-FLXHR-LIDAR DRE and (bottom) CALIPSO-retrieved AOD over the SE Atlantic (0°S - 20°S , 10°W - 10°E) from 2007-2010. The aerosol optical depth is separated by various aerosol types (marine=blue, dust=red, polluted continental=yellow, polluted dust=green, smoke=gray). During September, shown in beige, positive DRE values are coincident with high values of smoke AOD.

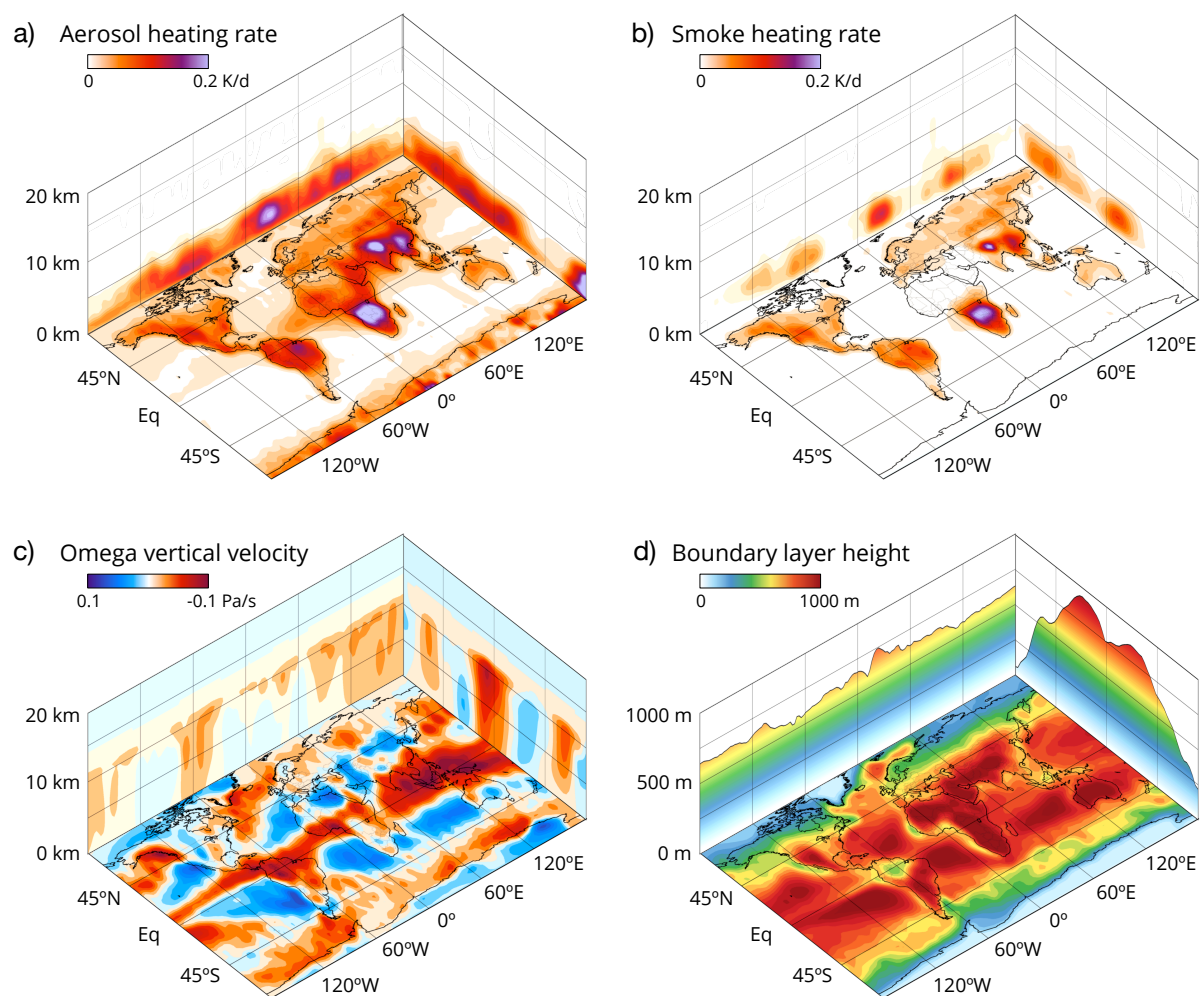


Figure 5.2: A 3D view of annual mean (a) 2B-FLXHR-LIDAR aerosol heating rates, (b) 2B-FLXHR-LIDAR smoke aerosol heating rate, (c) MERRA vertical velocity, and (d) MERRA boundary layer height.

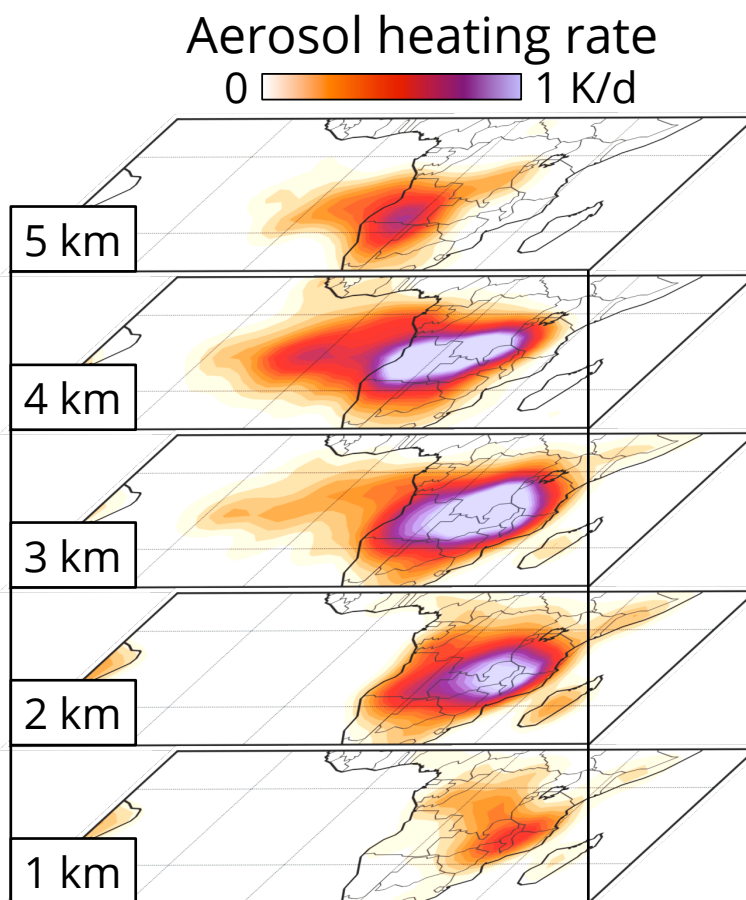


Figure 5.3: A 3D view by height of aerosol shortwave heating rate (in Kelvin per day) during September. Low-lying marine clouds (at an altitude of 1 km) provide the environmental conditions necessary for aerosol solar heating over the Atlantic Ocean.

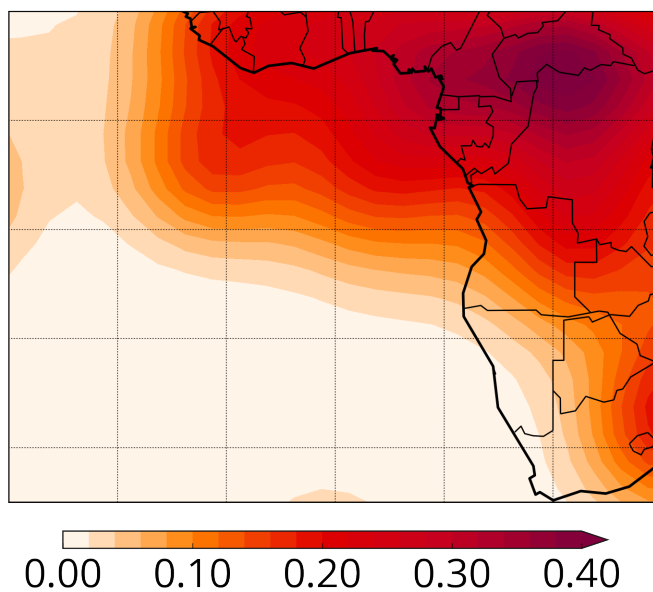


Figure 5.4: Estimated uncertainty in 2B-FLXHR-LIDAR aerosol shortwave heating rate (in K/day). Uncertainty is computed by perturbing radiative fluxes over a range of possible values of single scattering albedo.

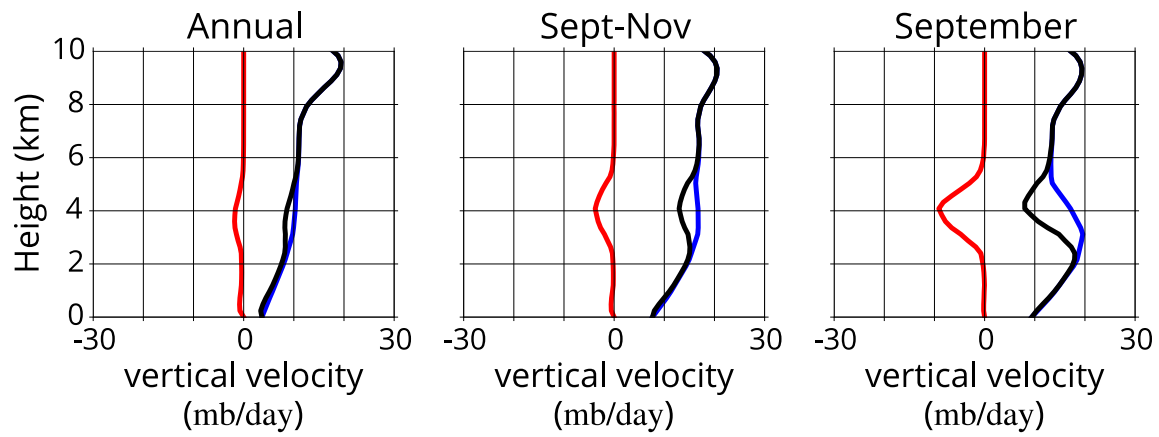


Figure 5.5: Vertical velocity profiles over the southeast Atlantic Ocean (0°S - 20°S , 10°W - 10°E) from (blue) MERRA reanalysis, (red) 2B-FLXHR-LIDAR aerosol heating, and (black) the combination of both. While the vertical velocity from aerosols is strongest during September, it is still considerably weaker than the predominant subsidence observed over this region.

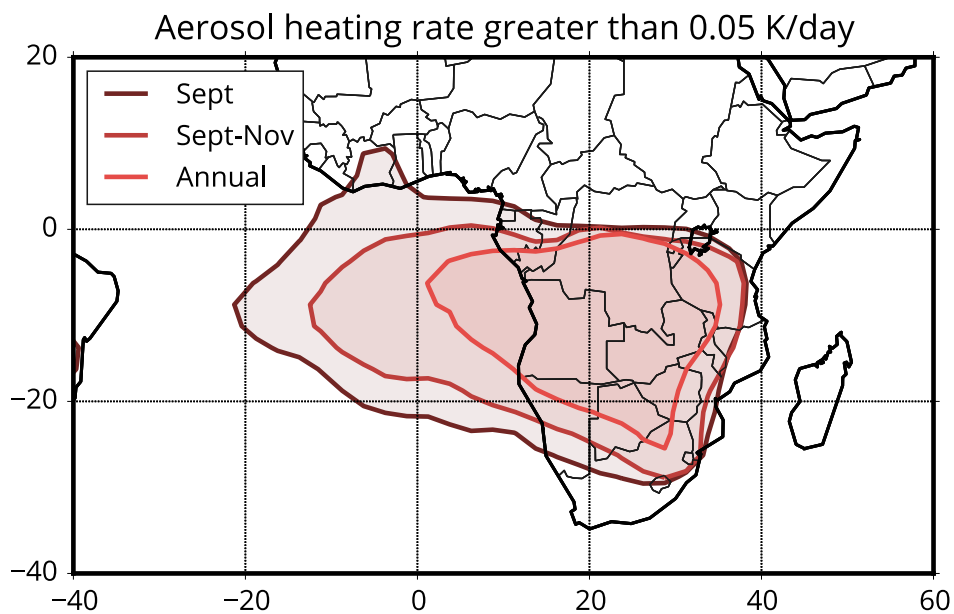


Figure 5.6: Areal extent of aerosol heating rate greater than 0.05 K/day from 2B-FLXHR-LIDAR. The largest extent of heating over the southeast Atlantic Ocean is during September, followed by Sept-Nov, and then on annual timescales.

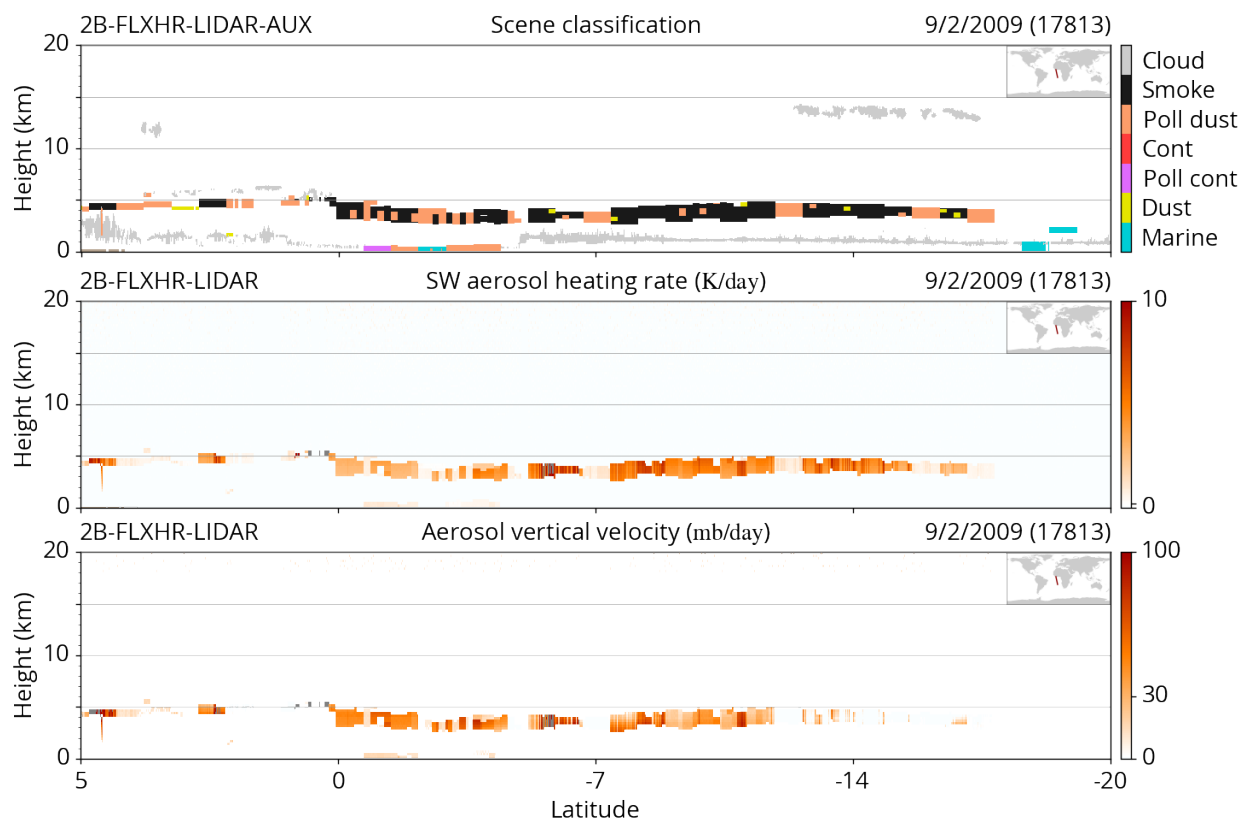


Figure 5.7: Vertical profiles of an A-Train overpass over the tropical Atlantic Ocean (5°N-20°S). The (top) scene classification shows the CloudSat/CALIPSO cloud mask and CALIPSO aerosol types. The (middle) aerosol heating rate from 2B-FLXHR-LIDAR. The (bottom) aerosol vertical velocity from 2B-FLXHR-LIDAR is an estimate of vertical motion of aerosol layer due to diabatic heating.

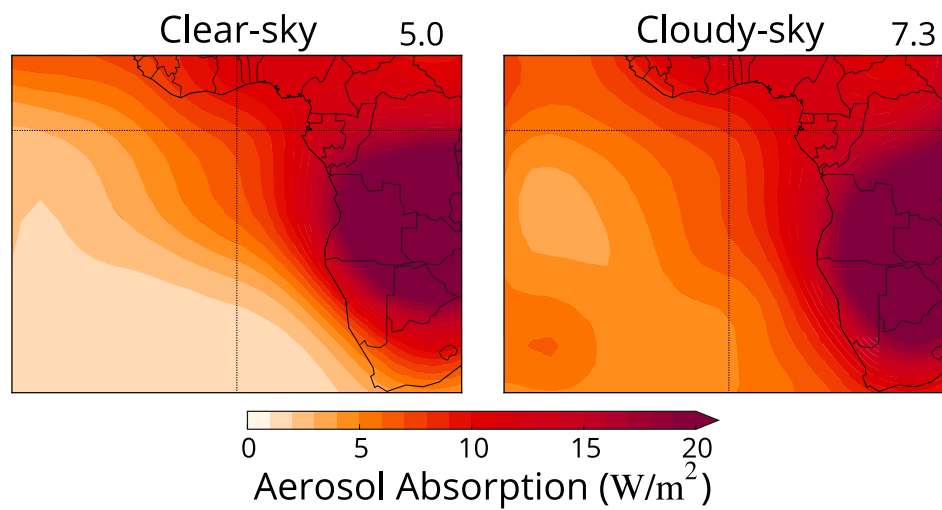


Figure 5.8: Regional maps of the (left) clear-sky and (right) cloudy-sky column-integrated aerosol absorption in SON from 2B-FLXHR-LIDAR. Aerosol absorption is nearly 50% stronger in cloudy scenes because of absorption of reflected solar radiation due to the presence of underlying clouds.

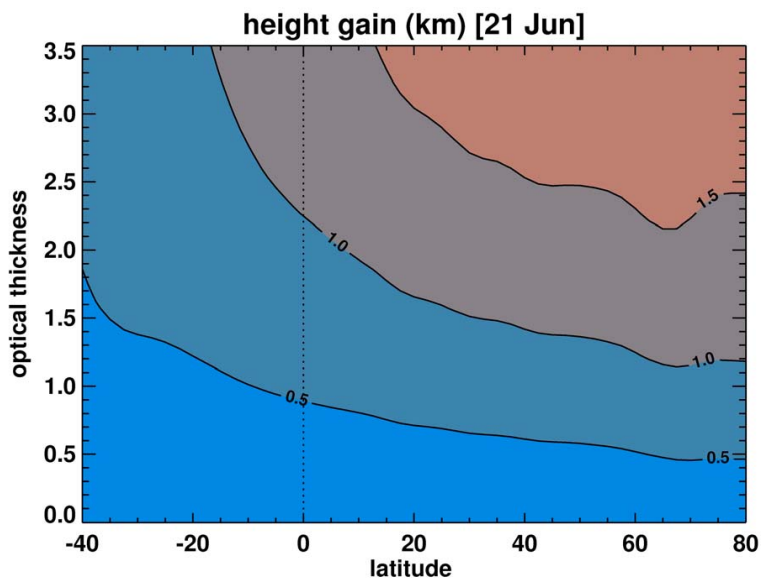


Figure 5.9: (from Boers et al., 2010) Simulated height gain of an aerosol layer in a period of 24 hours due to solar absorption. For an aerosol layer with $SSA = 0.75$, $\alpha = 1.50$.

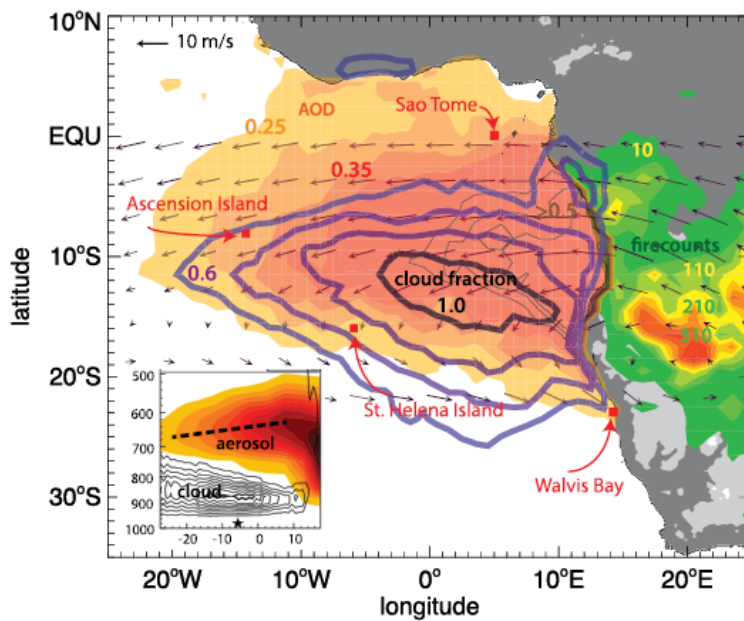


Figure 5.10: (from Zuidema et al., 2016) Biomass burning aerosols from fires over central Africa are transported over marine clouds in the southeast Atlantic Ocean. The aerosol optical depth (warm colors), fire count (green to red), and cloud fraction (contoured in blue) are shown.

Chapter 6

The Contribution of Direct Radiative Forcing by Aerosol Type

6.1 Introduction

To this point this study has discussed methods to quantify, using a new multi-sensor A-Train satellite dataset, the present-day global direct radiative effects and atmospheric heating of all aerosols. However, it is well documented that different aerosol species have different radiative impacts on their environment (Myrhe et al., 2013; Bond et al., 2013). It has also been noted that, due to internal mixing of aerosols, the sum of the total radiative effect is not necessarily the sum of each aerosol type contribution (Ocko et al., 2012). The differences in aerosol optical properties are in part attributed to differences in aerosol sizes. Figure 6.1 illustrates the idealized tri-modal size distribution of aerosols commonly observed in the atmosphere. Tiny aerosols in the nucleation mode (< 0.1 micron) have a negligible influence on radiative fluxes. Large aerosols in the coarse mode (> 1 micron) are more important for interactions in the longwave than in the shortwave. Aerosols in the accumulation mode, however, are comparable in size to wavelengths of visible light and interact strongly with shortwave radiation according to Mie theory. Within the accumulation mode, aerosols are made of many components with each component exhibiting different optical properties. In particular, the single scattering albedo and asymmetry factor of black carbon soot is quite different than other aerosol components (Figure 6.2) and these aerosol optical properties must be properly accounted for to accurately quantify the radiative impacts of aerosols. For example, the global distribution of aerosol direct radiative effect exhibits large regional variability owing to interactions with different aerosol types as shown in Figure 6.3. In this section we present an analysis to separate the contributions from various components of aerosols on the total radiative impact. The partitioning of radiative impacts by aerosol type will provide valuable insight into the role of different aerosol species on the global energy budget in an attempt to tease out the radiative impacts of aerosols from natural and anthropogenic sources. While many studies have investigated the radiative effects of

aerosol types using numerical models, this study attempts to accomplish this task using a novel satellite-based approach.

Previous assessments of aerosol direct radiative forcing are documented in the IPCC AR5. Based on a combination of modeling and observation based studies, the global mean aerosol radiative forcing is estimated to be -0.35 W m^{-2} (-0.85 to $+0.15$) and is the average of the Myhre et al. (2009) observationally-based estimate (-0.3 W m^{-2}) and the Bellouin et al. (2013) model reanalysis estimate (-0.4 W m^{-2}). This estimate is slightly weaker than the previous IPCC AR4 reported value of -0.5 W m^{-2} (-0.90 to $+0.10$) and has been attributed in the IPCC report to a modified sensitivity in black carbon aerosol (Ma et al., 2012). The AeroCom II modeling studies have performed simulations of aerosol distributions in 1850 and 2000 to isolate DRF for individual aerosol types. Over the 1850-2000 period, the AeroCom II global DRF estimate is -0.31 W m^{-2} (-0.58 to -0.11), shown in Figure 6.4, with species breakdown by sulfate aerosol (-0.40 W m^{-2} : -0.60 to -0.20), black carbon from fossil fuel and biofuel ($+0.40 \text{ W m}^{-2}$: $+0.05$ to $+0.8$), primary and secondary organic aerosol (-0.12 W m^{-2} : -0.40 to $+0.10$), biomass burning ($+0.0 \text{ W m}^{-2}$: -0.20 to $+0.20$), nitrate aerosol (-0.11 W m^{-2} : -0.30 to -0.03), mineral dust (-0.10 W m^{-2} : -0.30 to $+0.10$), according to Myhre et al., 2013. However, it should be noted that the speciated breakdown of DRF is less certain than the total estimate due to large uncertainties in pre-industrial and present day aerosol inventories.

This study will present a new global estimate of direct radiative forcing of various aerosol species. This approach evaluates anthropogenic forcing using aerosol direct radiative effect data from 2B-FLXHR-LIDAR and aerosol optical depth (AOD) data from the SPRINTARS global aerosol model. SPRINTARS provides global distributions of pre-industrial (1850) and present-day (2010) AOD for black carbon, organic carbon, sulfate, soil dust, and sea salt. The emission inventories of carbonaceous aerosols originating from biomass burning, biofuel, agricultural activity, and fossil fuels are based on several databases from the Food and Agriculture Organization of the United Nations (FAO), Global Emissions Inventory Activities (GEIA), and energy statistics in each nation (Takemura et al., 2005). Sulfur dioxide emissions are based on the GEIA database with atmospheric chemistry prescribed by the global chemistry model, CHASER. Mineral dust and sea salt emissions

are represented in this simulation using internal model parameters for vegetation, 10-m wind speed, soil moisture, and snow amount (Takemura et al., 2000).

This analysis uses the SPRINTARS model global simulations of present-day and pre-industrial AOD as shown in Figure 6.6. The difference between pre-industrial (1850) to present-day (2010) AOD is computed at 2.5-degree spatial resolution to determine the anthropogenic contributions of black carbon, organic carbon, sulfate, dust, and marine aerosols. As a simplification, sulfate is referred to as pollution and the combination of black carbon and organic carbon are referred to as smoke. This AOD difference map is then multiplied by the radiative kernels of AOD to derive observational estimates of anthropogenic radiative forcing for various aerosol species, using an approach employed in the radiative kernels calculations introduced by Soden et al. (2008). The implicit assumption using this methodology is clouds have not changed between pre-industrial and present-day periods. It is also assumed in this study that DRE varies linearly with AOD. This is a valid assumption on global scales given that the radiative effects of aerosols is relatively small and it is expected that an increase in aerosol loading will result in an increased radiative effect. By convention, therefore, it is assumed in this study that DRE varies linearly with AOD. Finally, global estimates of anthropogenic aerosol radiative forcing are evaluated with previous assessments using global models for comparison.

For reference, the SPRINTARS AOD and CALIPSO AOD are compared in Figure 6.7. For CALIPSO, the pollution category represents the combination of polluted continental and polluted dust aerosol classifications. There are a few disagreements between SPRINTARS and CALIPSO. In particular, CALIPSO appears to underestimate marine AOD especially over the Southern Ocean. This bias in CALIPSO AOD has been documented and is likely attributed to the inability of CALIPSO lidar to detect optically thin aerosol layers near the ocean surface (Dawson et al., 2015). Furthermore, there are differences in the AOD estimates of pollution. While SPRINTARS indicates high pollution AOD over Europe and East Asia, CALIPSO indicates higher values over South Asia and the tropical Atlantic where polluted dust is frequently observed. There is much better agreement between SPRINTARS and CALIPSO for global estimates of the dust and smoke AOD. Overall,

while the comparison of AOD is not a perfect match there is sufficient agreement for this type of analysis to estimate aerosol radiative forcing.

It is anticipated that anthropogenic radiative forcing will have the largest contributions from sulfate aerosols over the U.S., Europe, and East Asia. It is well documented that these regions have produced significant emissions of fossil fuel particulates since the pre-industrial period. Accordingly, we expect the largest radiative forcing to occur over regions with the largest emissions of sulfate aerosols. To highlight a preliminary result from this study, Figure 6.8 shows the annual mean aerosol direct radiative effects separated by CALIPSO aerosol types. Since CALIPSO has the capability to distinguish aerosol layers by various aerosol types, we may assess the contributions of each type to the total radiative impact using the 2B-FLXHR-LIDAR dataset. Marine aerosols exert a net cooling effect of -0.61 W/m^2 and contribute over 40% of the total direct effect. However, smoke aerosols are observed to exert a net positive effect over land surfaces with a global radiative effect of 0.24 W/m^2 . Polluted continental aerosols also exert positive radiative effects, in particular over Greenland and Antarctic ice sheets where absorbing aerosols enhance the absorption of solar radiation. It should be noted that while Figure 6.8 does not directly quantify anthropogenic forcing, the CALIPSO type likely most representative of anthropogenic aerosols is Polluted Continental type (known as pollution in this study) including particles that are relatively small, mainly spherical, and moderately absorbing (Omar et al., 2007).

A distinct advantage of using spaceborne radar and lidar data to assess aerosol radiative forcing is the ability to detect cloud fields in three dimensions. As noted previously, many global climate models have considerable biases in simulating cloud fields and these cloud cover biases have the potential to significantly alter the radiative impacts of aerosols. The 2B-FLXHR-LIDAR dataset features vertically-resolved cloud information from CloudSat and CALIPSO from 2007-2010. These active sensors provide a three dimensional climatology of clouds and aerosols in the atmosphere from 2007-2010. While this time period may not be fully representative of the anthropogenic period, it is assumed in this analysis that global cloud fields have remained the same over the past two centuries. While the spatial patterns of clouds almost certainly vary over time, it is still unknown whether global cloud patterns have changed considerably over the past decade (Zhou et al., 2016).

Furthermore, it is generally assumed that satellite observations outperform numerical model simulations in the representation of global cloud fields.

Overall, the 2B-FLXHR-LIDAR dataset affords the unique opportunity to evaluate global aerosol direct effects for various aerosol species types and under a range of aerosol optical properties. Several regions with unique aerosol characteristics will be investigated in greater detail in this assessment. Three regions will be highlighted, including the eastern USA (polluted continental aerosols), SE Atlantic (biomass burning aerosols), and eastern Asia (polluted dust aerosols). By assessing the radiative properties of aerosols over these regions and comparing against corresponding estimates in global model simulations, we expect to gain a greater understanding of how to improve the representation of aerosol radiative effects and anthropogenic forcing in global climate models.

6.2 Methodology

Aerosol direct radiative forcing may be calculated using one of many techniques. In this analysis, a simple linear-scaling approach is employed to provide a direct means of comparison with other analyses. Here, the aerosol direct radiative forcing (DRF) is defined as the difference in direct radiative effect in present day minus the direct radiative effect in pre-industrial times:

$$DRF = DRE_{pD} - DRE_{pI} \quad (7)$$

It is assumed in this study that the direct radiative effect increases linearly with aerosol optical depth. This assumption is reasonable considering the radiative effects of aerosols are relatively small. Given this approximation, the expression for aerosol direct radiative forcing may be expanded as follows.

$$DRF = \left[\left(\frac{\partial DRE}{\partial AOD} \right) \cdot AOD \right]_{pD} - \left[\left(\frac{\partial DRE}{\partial AOD} \right) \cdot AOD \right]_{pI} \quad (8)$$

It follows that the sensitivity of DRE to AOD is the same in present day as it was in pre-industrial times. When AOD is zero, then the DRE is also zero. This simplifies the equation for computing the direct radiative forcing where the difference in AOD is computed using SPRINTARS model output.

$$DRF = \left(\frac{DRE_{PD}}{AOD_{PD}} \right) \cdot (AOD_{PD} - AOD_{PI}) \quad (9)$$

The change in DRE with respect to AOD is referred to as the radiative kernel, K . The radiative kernel is a measure of radiative feedback and is calculated using satellite-based estimates from CALIPSO.

$$K = \frac{\partial DRE}{\partial AOD} \approx \frac{DRE_{PD}}{AOD_{PD}} \quad (10)$$

From this relationship, the aerosol direct radiative effect is assumed to follow a linear relationship with aerosol optical depth. This linear relationship in aerosol observations will be investigated in greater detail in future analyses. The linear scaling of DRE to AOD is a technique that has been employed in a number of other studies (Wang et al., 2007; Yu et al., 2012) and is a reasonable assumption especially over surfaces of uniform reflectance. For example, this assumption is suitable for describing aerosols residing over open ocean since the ocean surface is always darker than the aerosol layer. Additionally, this assumption works well for describing smoke aerosols over thick clouds since the aerosol layer is always darker than the clouds below. Where this assumption is not suitable is over areas where the aerosol or surface optical properties are highly variable.

6.3 CALIPSO aerosol type classification

In the atmosphere, aerosols are rarely composed entirely of one material. In fact, most particles are composites of different aerosol species. Given the complexity of aerosol speciation over space and time, it is often convenient and necessary to group aerosol layers of similar attributes into aerosol types. In this analysis, aerosol layers are categorized according to the CALIPSO aerosol type classification described in Omar et al., 2009. CALIPSO identifies features using a cloud-aerosol

discrimination (CAD) algorithm. From this feature mask only aerosol features identified with high confidence are classified into aerosol types. The classification scheme is determined using lidar backscatter signal differences in the 532-nm and 1064-nm channels. Aerosols are grouped by observed physical and optical properties based on a cluster analysis of the AERONET dataset from 1993-2002. Based on the cluster analysis, six aerosol types are identified based on the retrieved extinction-to-backscatter ratio of the layer. The six CALIPSO aerosol types are marine, dust, clean continental, polluted continental, polluted dust, and smoke.

6.4 Direct radiative effects by aerosol type

The global map of aerosol direct radiative effect is presented in the previous chapters. These data display the DRE of shortwave radiation at the top-of-atmosphere because this distinction has been recognized by the IPCC reports as the most important for climate. While global results are useful for understanding aerosol-radiation processes as a whole, there is additional information gained by picking apart the data to examine the finer nuances. For example, there is considerable variability in DRE by region. Each region consists of different aerosol types, with different environmental conditions, and different responses to shortwave radiation. As previously presented, Figure 6.2 displays the probability density function (PDF) of DRE for selected regions, computed using the 2B-FLXHR-LIDAR dataset. Broad distributions are representative of large variability in observed DRE values, whereas narrow distributions are representative of relatively small variability. In addition, distributions shifted to the left of the dashed line indicate a strong cooling effect, whereas distributions shifted to the right have a stronger warming effect. For example, the SE Atlantic region has a greater probability of positive DRE values than many other regions, for reasons described in the previous chapter. On the contrary, the SE Pacific has a narrower DRE that is representative of an area with relatively weak aerosol effects. These results highlight that there is considerable variability in aerosol effects by region that is attributed to aerosol speciation differences, a topic that will be explored in greater detail later on in this chapter.

However, the 2B-FLXHR-LIDAR dataset has the capability to perform radiative flux calculations other than just the shortwave effects at the top-of-atmosphere. The algorithm can also estimate other important aspects of the global energy budget, including the direct radiative effects on longwave

radiation and at the surface. Figure 6.5 displays the global shortwave, longwave, and net DRE at the top-of-atmosphere (TOA), surface (BOA), and in-atmosphere absorption (ATM). Aerosol-radiation interactions in the shortwave are significant in large part due to the Mie scattering from particles with sizes similar to the wavelengths of visible light. Since particle sizes are often sub-micron, these aerosols interact with shortwave radiation according to Mie theory. However, larger particles in the so-called coarse mode can also interact with radiation of longer wavelengths. Other studies have noted that radiative effects in the longwave tend to be strongest for large particles (i.e. mineral dust) at high altitudes (Reddy et al., 2005; McCormick et al., 1995). This finding is supported by Figure 6.5, which indicates the strongest longwave effects over desert areas of the Middle East and North Africa. A significant temperature contrast, and hence vertical separation, between the aerosol layer and the surface is necessary for aerosol interactions with longwave radiation. Since most aerosols reside near their emission sources on the Earth's surface, longwave effects are less frequent and relatively weaker than shortwave effects. Overall, the global patterns of DRE on net radiation closely resemble those of shortwave radiation with the largest differences observed over arid desert regions.

It has been demonstrated that there is value in separating radiative effects by shortwave and longwave contributions. In addition, there is value in separating aerosol direct effects by aerosol types. This separation helps to quantify the contribution from different aerosol components for impacting radiative fluxes. Knowledge on the climate impacts of individual species may be particularly valuable for policymakers in regulating the aerosol components that pose adverse effects on climate. The global maps of DRE by aerosol types are shown in Figure 6.8. The CALIPSO aerosol types include marine, dust, polluted continental, clean continental, polluted dust, and smoke. All aerosol observations with a single-type AOD less than 80% are separated in a separate category of mixed aerosols. Marine aerosols are shown to have a global DRE of -0.61 W m^{-2} , representing the largest contribution and nearly half the total DRE of -1.33 W m^{-2} . A significant contribution is from dust with a global DRE of -0.29 W m^{-2} with effects greatest over the tropical Atlantic and Indian Oceans. Dust exerts a warming effect over much of North Africa where the bright desert enhances solar absorption. Pollution aerosols, consisting of a mixture of sulfate, soot, and other aerosols, have a considerable global effect of -0.43 W m^{-2} but locally large impact over Greenland and Antarctica ice sheets where DRE is observed to exceed 5 W m^{-2} . Smoke aerosols are found to have the strongest net warming

effect. With a global DRE of $+0.24 \text{ W m}^{-2}$, smoke with particularly large impacts over Central Africa and Southeast Asia. Given the wide range of radiative impacts from various types of aerosol, this analysis highlights the importance of understanding how different types of aerosol particles play a different role in atmospheric energy exchanges.

6.5 Satellite-based estimates of aerosol direct radiative forcing

There has been much interest in quantifying the direct radiative effect of all aerosols on the global energy budget. But there is also considerable interest in determining the impact of only anthropogenic aerosols known as the direct radiative forcing (DRF). Figure 6.9 shows the global estimates of DRF using combined 2B-FLXHR-LIDAR/SPRINTARS data. The values are computed using a linear scaling of AOD and DRE, with AOD distributions obtained from the SPRINTARS aerosol model for consistency. The global 2B-FLXHR-LIDAR estimate of DRF is -0.21 W m^{-2} . The largest contributions are from pollution (-0.24 W m^{-2}), while smoke aerosols exert a net positive forcing (0.32 W m^{-2}). Pollution, consisting of polluted continental and polluted dust CALIPSO types, is shown to have a cooling effect over Europe and East Asia, while a warming effect over Greenland and Antarctica ice sheets where high surface albedo enhances aerosol absorption. Marine aerosols and dust aerosols are have a sizable contribution to radiative forcing in this analysis. Smoke aerosols, are shown to have a positive forcing with significant warming over Southeast Asia. In the IPCC AR5, the global mean aerosol radiative forcing is estimated to be -0.35 W m^{-2} (-0.85 to $+0.15$) and is the same value as reported in the AeroCom II model intercomparison study. The IPCC AR5 DRF estimate is also the average of the Myhre et al. (2009) observationally based estimate (-0.3 W m^{-2}) and the Bellouin et al. (2013) model reanalysis estimate (-0.4 W m^{-2}). This estimate is slightly weaker than the previous IPCC AR4 value of -0.5 W m^{-2} (-0.90 to $+0.10$) and has been attributed in the IPCC report to a modified sensitivity in black carbon aerosol (Ma et al., 2012). Figure 6.10 compares the global direct forcing estimate from the AEROCOM II and 2B-FLXHR-LIDAR datasets. Overall, while the two datasets show consistent patterns of cooling over most regions, the 2B-FLXHR-LIDAR/SPRINTARS estimate shows stronger warming at high latitudes suggesting enhanced absorption over high albedo surfaces.

This study quantifies, for the first time, satellite-based radiative kernels of aerosol direct radiative effects as shown in Figure 6.10. The radiative kernels represent the sensitivity of DRE in response to a change in AOD for each aerosol type. In other words, the radiative kernels identify which areas would be directly impacted most by a change in the aerosol. The radiative kernels are multiplied by maps of AOD to compute the direct radiative effect for each aerosol type. For example, an increase in marine AOD is expected to decrease outgoing SW fluxes especially over high-latitude oceans. Alternatively, an increase in smoke AOD by 1.0 is expected to increase outgoing SW fluxes by 25 W m^{-2} globally on the annual mean. Mixed aerosols, including multiple distinct layers of smoke and other particles, shows a trend of positive radiative feedback over ocean while a negative feedback over desert surfaces. Radiative kernels in general are valuable tools for assessing the uncertainties in global climate model simulations. In addition, radiative kernels may be used to evaluate the climate impacts of wildfires, dust storms, and volcanic eruptions given knowledge of the distribution of AOD. Observation-based kernels, such as the ones described in this study, may provide benefit to the modeling community to further evaluate the sensitivity of various aerosol types to improve simulations of aerosol radiative impacts.

6.6 Chapter summary

CALIPSO lidar has the unique ability to distinguish aerosol layers by aerosol type using dual channel retrievals. This aerosol typing information is valuable for evaluating the radiative impact of each individual species and potentially useful for policymakers. The unique capability of CALIPSO to identify aerosol types offers a great opportunity to investigate key science questions difficult to address using data from conventional passive sensors. To address unanswered science questions, this study tests the following hypotheses:

1. Anthropogenic aerosol forcing will have the strongest contribution from aerosols classified by CALIPSO as polluted continental.
2. By including aerosols above clouds, our estimate of DRF will be weaker than previous satellite-based estimates.

This study highlights the utility of active remote sensing for understanding how various components of aerosols impact the global energy budget. Using the aerosol type classification from CALIPSO, we have performed global assessments of aerosol type contributions to direct radiative effects as well as direct radiative forcing. While most aerosol types exert a cooling effect on climate, absorbing smoke aerosols are shown to produce a net warming effect that is amplified by the presence of clouds. The 2B-FLXHR-LIDAR/SPRINTARS DRF is estimated to be -0.21 W m^{-2} with the largest contributions from pollution aerosols (-0.24 W m^{-2}) and smoke aerosols (0.32 W m^{-2}). For the first time, satellite-based radiative kernels offer a valuable tool to improve model simulations of aerosol-radiation interactions. Given the high sensitivity of DRE and DRF to cloud cover, results further highlight the importance of correctly representing cloud fields in future analyses of aerosol-radiation interactions. In the future, satellite missions such as the Earth Cloud Aerosol and Radiation Explorer (EarthCARE) and Aerosol-Cloud-Ecosystems (ACE) will provide advanced observations of aerosol necessary to distinguish aerosol typing and refine estimates in aerosol radiative forcing. Improving global estimates of DRF may be made possible in future satellite missions, in particular, using a spaceborne multi-wavelength high-spectral resolution lidar (HSRL) capable of simultaneous backscatter and extinction retrievals for a more refined aerosol classification (Burton et al., 2014).

Global Mean Radiative Forcing ($W m^{-2}$)				
	SAR	TAR	AR4	AR5
Sulphate aerosol	-0.40 (-0.80 to -0.20)	-0.40 (-0.80 to -0.20)	-0.40 (-0.60 to -0.20)	-0.40 (-0.60 to -0.20)
Black carbon aerosol from fossil fuel and biofuel	+0.10 (+0.03 to +0.30)	+0.20 (+0.10 to +0.40)	+0.20 (+0.05 to +0.35)	+0.40 (+0.05 to +0.80)
Primary organic aerosol from fossil fuel and biofuel	Not estimated	-0.10 (-0.30 to -0.03)	-0.05 (0.00 to -0.10)	-0.09 (-0.16 to -0.03)
Biomass burning	-0.20 (-0.60 to -0.07)	-0.20 (-0.60 to -0.07)	+0.03(-0.09 to +0.15)	-0.0 (-0.20 to +0.20)
Secondary organic aerosol	Not estimated	Not estimated	Not estimated	-0.03 (-0.27 to +0.20)
Nitrate	Not estimated	Not estimated	-0.10 (-0.20 to 0.00)	-0.11 (-0.30 to -0.03)
Dust	Not estimated	-0.60 to +0.40	-0.10 (-0.30 to +0.10)	-0.10 (-0.30 to +0.10)
Total	Not estimated	Not estimated	-0.50 (-0.90 to -0.10)	-0.35 (-0.85 to +0.15)

Table 6.1: Global estimates of aerosol direct radiative forcing between 1750 and 2011 of seven aerosol components in the IPCC SAR, TAR, AR4, and AR5 reports (Myhre et al., 2013).

Aerosol type	Direct radiative effect (W m^{-2})	Direct radiative forcing (W m^{-2})
Marine	-0.61	-0.003
Dust	-0.29	0.004
Pollution	-0.43	-0.240
Smoke	0.24	0.032
Total	-1.90	-0.206

Table 6.2: Global estimates of annual mean direct radiative effect (W m^{-2}) and anthropogenic direct radiative forcing (W m^{-2}) separated by four aerosol type classification using 2B-FLXHR-LIDAR. The pollution classification represents the combination of polluted continental and polluted dust subtypes from CALIPSO.

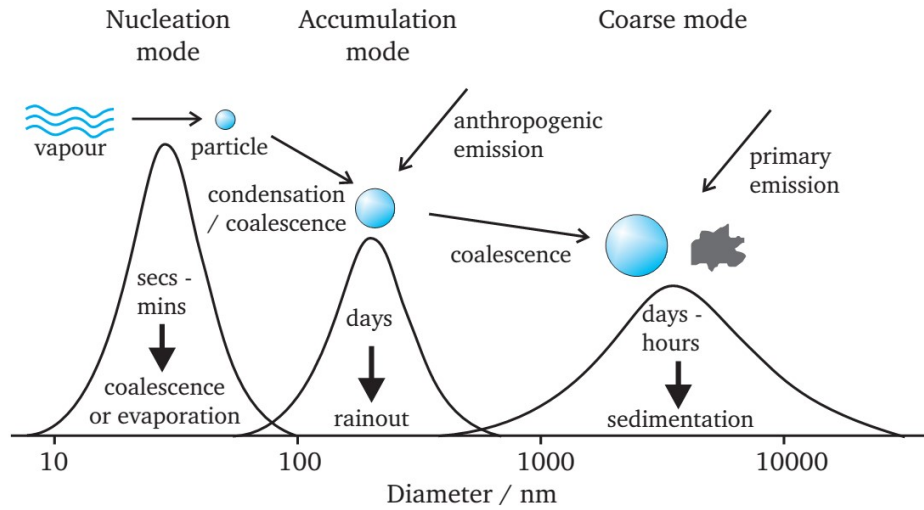


Figure 6.1: Schematic illustrating an idealized size distribution of aerosols. Shortwave effects tend to strongest for aerosols in the accumulation mode, in which particle diameter is comparable to the wavelengths of visible light according to Mie theory. Image courtesy of Jim Davies (LBNL).

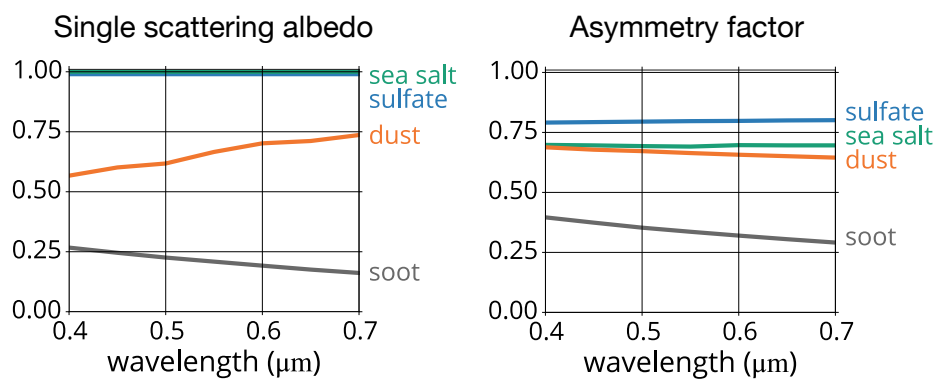


Figure 6.2: Plots of (left) single scattering albedo and (right) asymmetry factor in the shortwave for various aerosol components. The aerosol optical properties are computed according to Mie theory in the Optical Properties of Aerosols and Clouds (OPAC) dataset (Hess et al., 1998).

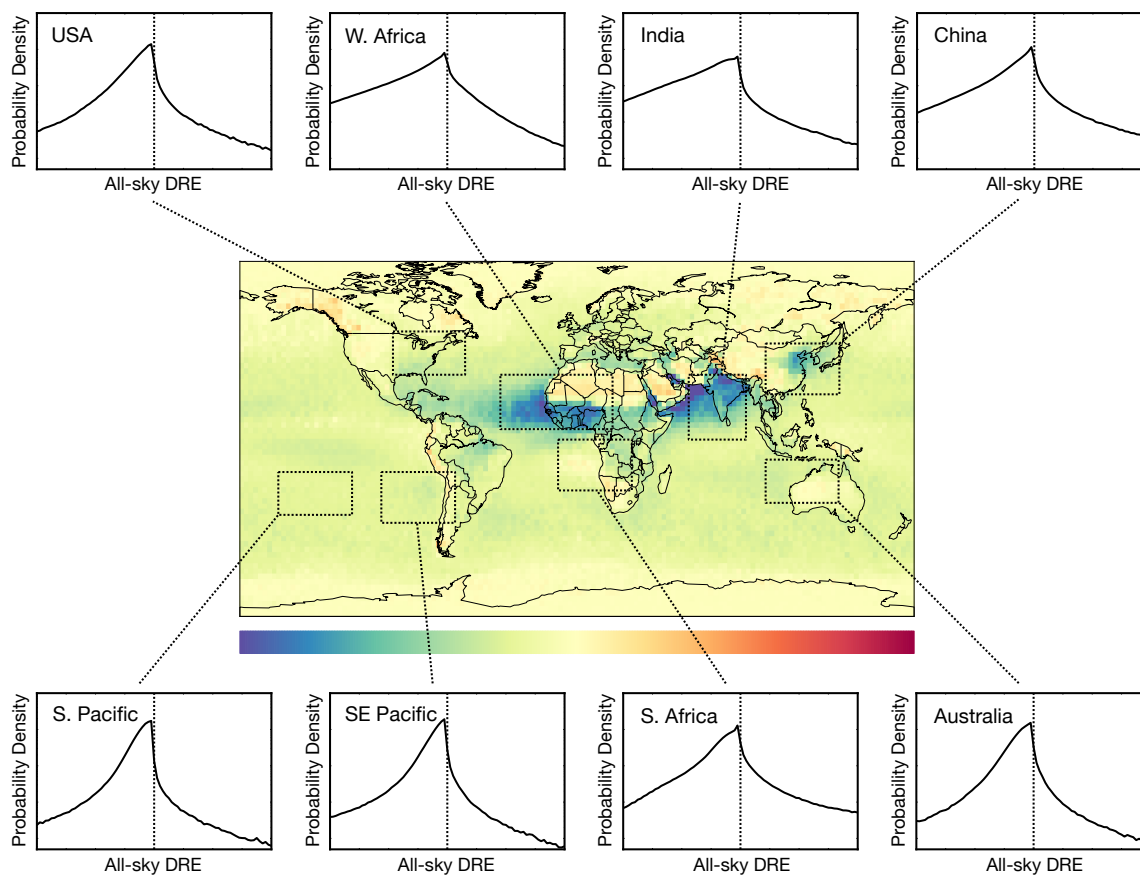


Figure 6.3: Probability density functions of all-sky DRE for selected regions. The shape of each function gives information about the relative likelihood of that value of DRE observed by 2B-FLXHR-LIDAR. A broad distribution indicates a large variability in aerosol radiative effects, whereas a narrow distribution suggests relatively little variability.

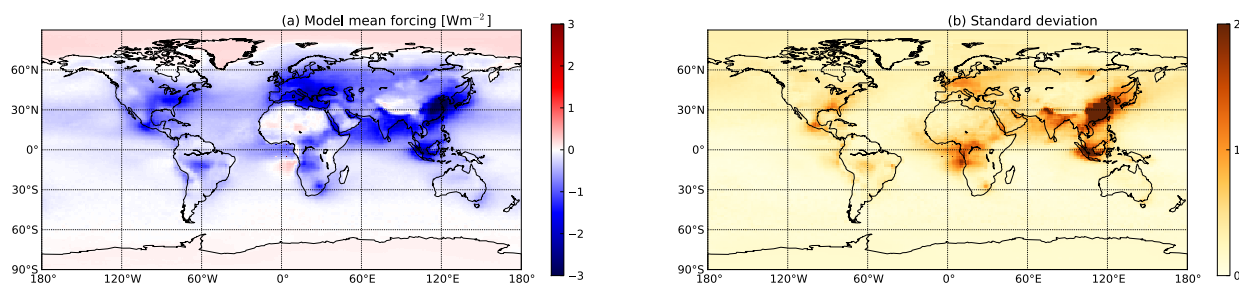


Figure 6.4: (from Myhre et al., 2013) AeroCom II model mean (left) aerosol DRF and (right) standard deviation. AeroCom II is an intercomparison of a large set of global aerosol models including an extensive evaluation against measurements and is used in the best estimate of DRF reported by the IPCC AR5.

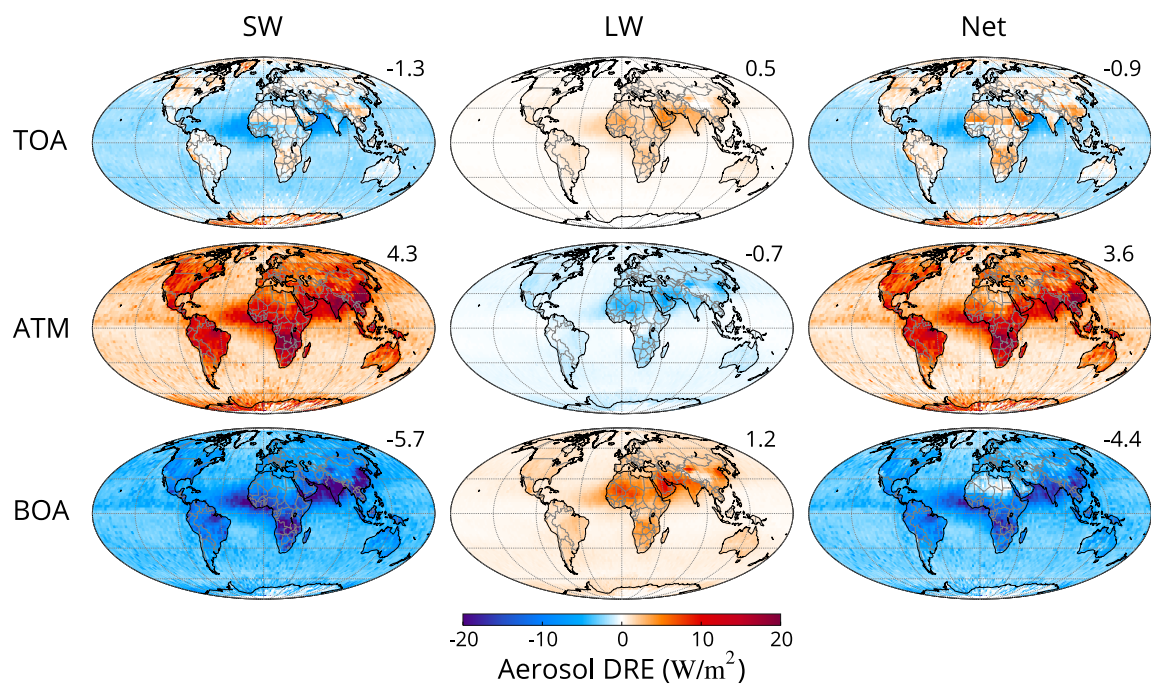


Figure 6.5: Aerosol direct radiative effects of shortwave, longwave, and net radiation are computed using 2B-FLXHR-LIDAR, 2007-2010. Global radiative effects at the top-of-atmosphere (TOA), within the atmospheric column (ATM), and at the bottom-of-atmosphere (BOA) are shown.

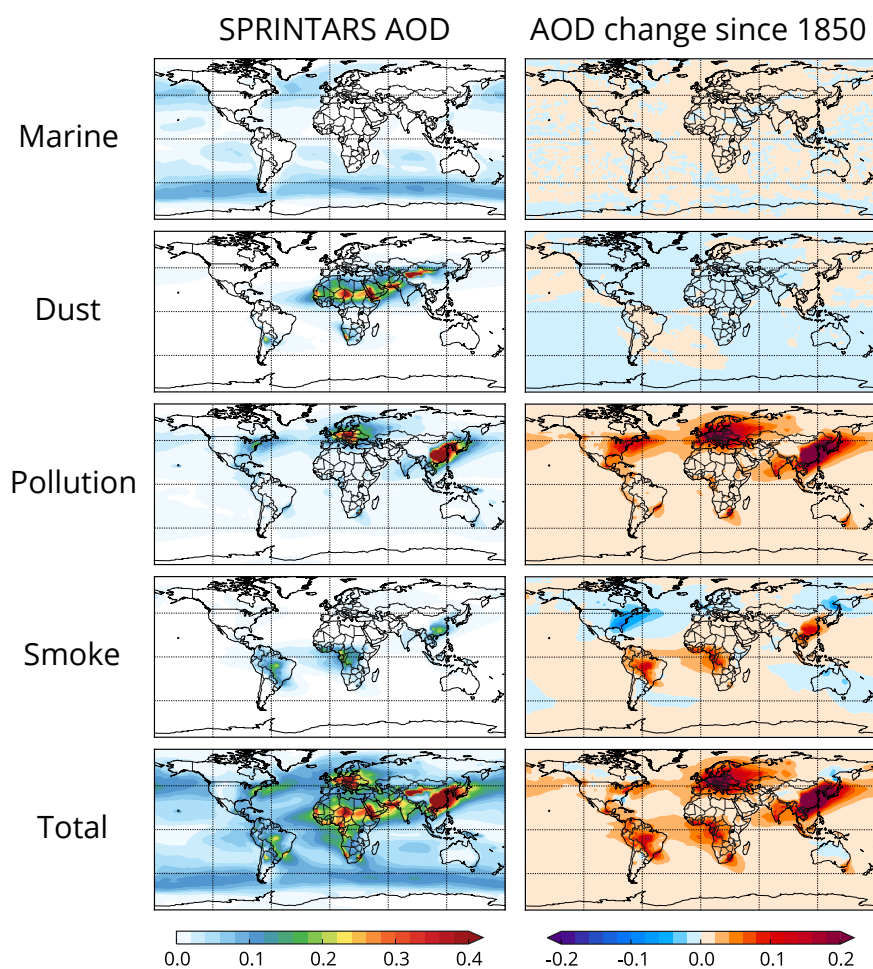


Figure 6.6: SPRINTARS global aerosol model simulations provide global estimates of aerosol optical depth for various aerosol species. The (left) present day AOD and (right) AOD difference maps between pre-industrial and present day AOD are shown. Emissions inventories are based primarily from the Global Emissions Inventory Activities (GEIA) and atmospheric chemistry prescribed by the CHASER model.

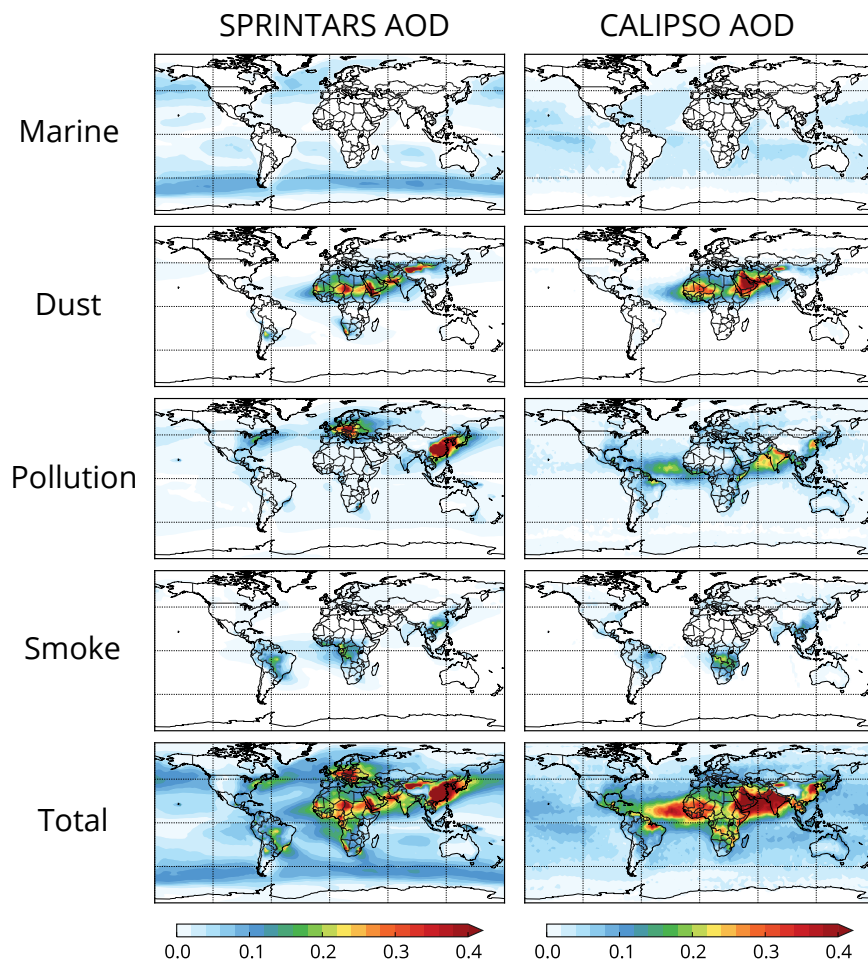


Figure 6.7: Year 2010 estimates of aerosol optical depth from (left) SPRINTARS and (right) CALIPSO shown for comparison. Emissions inventories in SPRINTARS are based primarily from the Global Emissions Inventory Activities (GEIA) and atmospheric chemistry prescribed by the CHASER model. For CALIPSO, the pollution category represents the combination of polluted continental and polluted dust aerosol classifications.

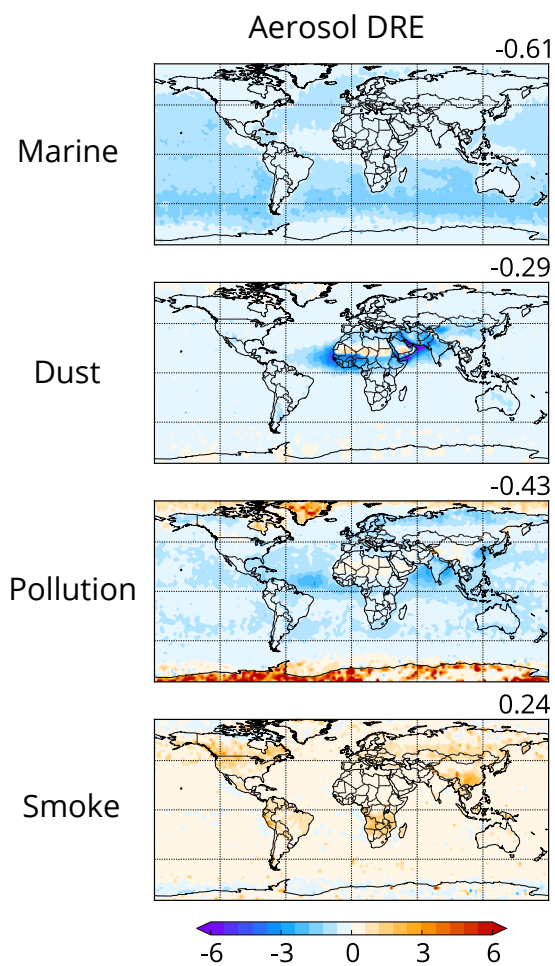


Figure 6.8: Annual mean aerosol direct radiative effects separated by CALIPSO aerosol types. The capability of CALIPSO's dual-frequency lidar to distinguish aerosol layers provides a unique tool for assessing the contributions of each type to the total radiative impact.

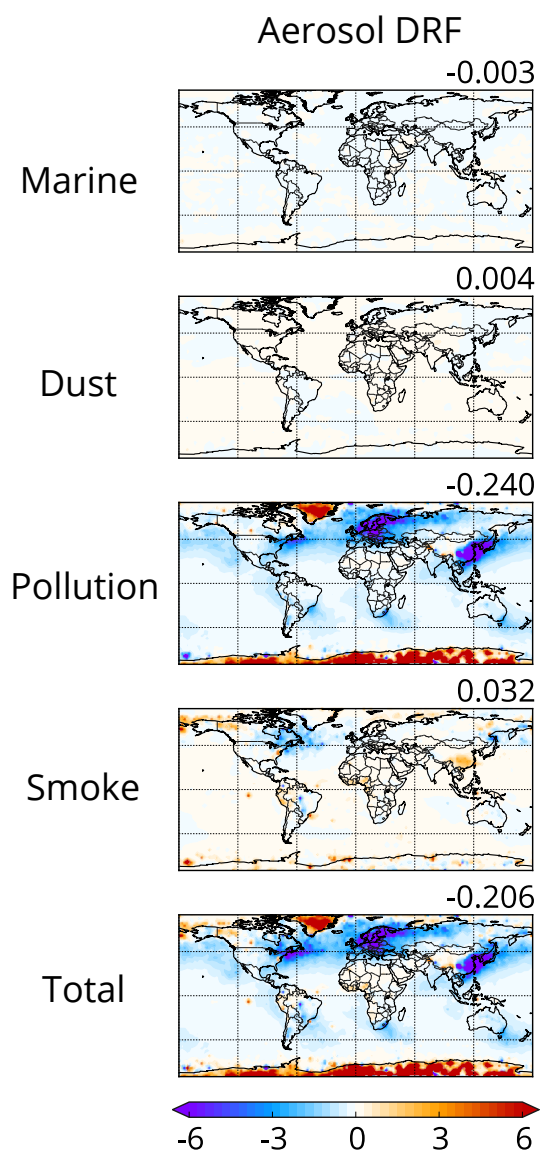


Figure 6.9: Annual mean aerosol direct radiative forcing separated by CALIPSO aerosol types. The direct radiative forcing is computed using observation-based radiative kernels of aerosol optical depth from 2B-FLXHR-LIDAR.

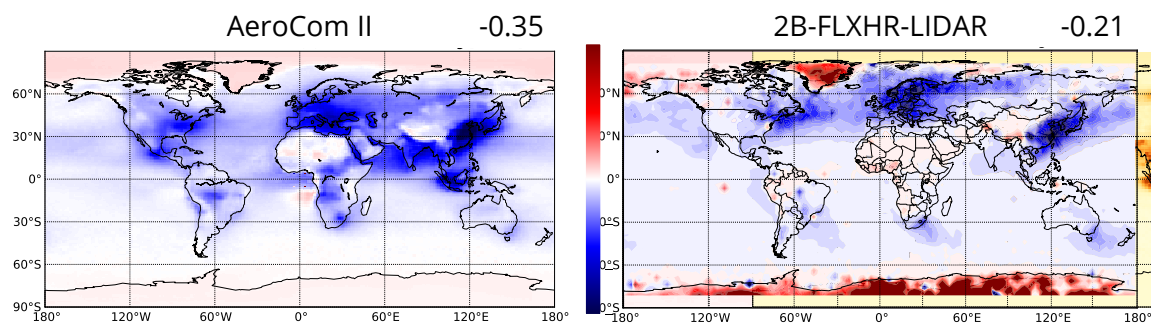


Figure 6.10: Comparison of global estimates of aerosol direct radiative forcing from (left) AeroCom II and (right) 2B-FLXHR-LIDAR. The AeroCom II multi-model intercomparison study of DRF was used to establish a best estimate of aerosol radiative forcing in the IPCC AR5 (Myhre et al., 2013).

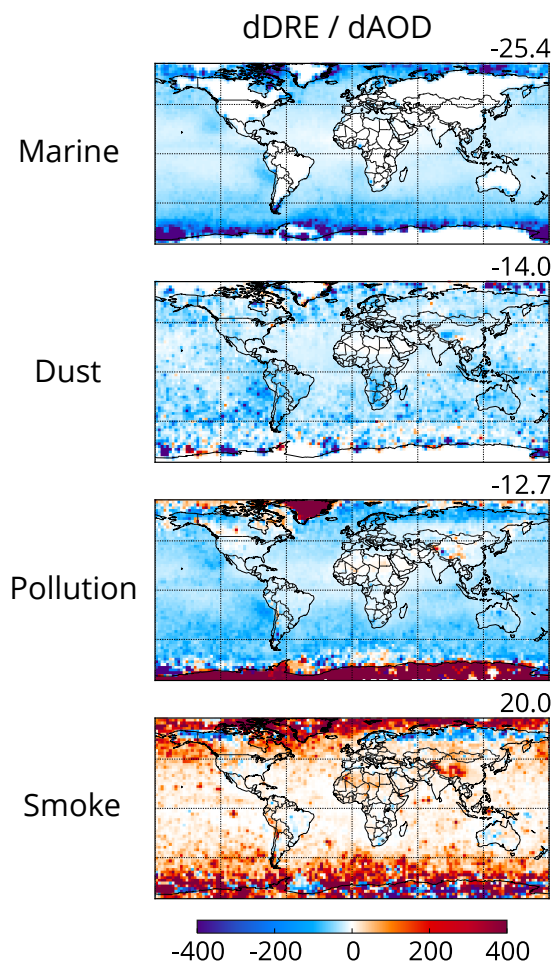


Figure 6.11: Satellite-based radiative kernels representing the sensitivity of outgoing shortwave radiation in response to change in aerosol optical depth. These kernels are computed using radiative fluxes from 2B-FLXHR-LIDAR and AOD from CALIPSO.

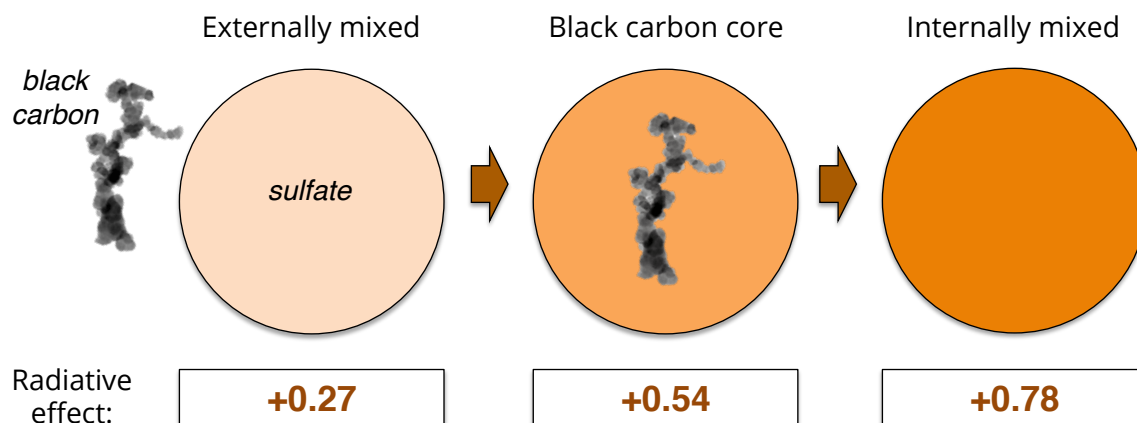


Figure 6.12: (adapted from Jacobson, 2000). Conceptual illustration of the aerosol mixing states of black carbon and their radiative effects in W/m^2 . While our understanding of aerosol mixing states is still incomplete, it is widely believed that an inorganic coating (i.e. sulfate) on black carbon serves to enhance the absorption efficiency of aged soot aerosol.

Chapter 7

Conclusions

7.1 Summary

Atmospheric aerosols impact the global energy budget by scattering and absorbing solar radiation. Despite their significant impact, aerosols remain a significant source of uncertainty in our ability to predict future climate. The key to reducing these uncertainties is improved representation of aerosol radiative processes in global models. Multi-sensor observations from the A-Train satellite constellation provide valuable observational constraints necessary to reduce uncertainties in model simulations of aerosol direct effects. This dissertation discusses recent efforts to quantify aerosol direct effects globally and regionally using CloudSat's new multi-sensor radiative flux and heating rates product (2B-FLXHR-LIDAR). Improving upon previous techniques, this approach leverages the capability of CloudSat and CALIPSO to retrieve vertically-resolved estimates of cloud and aerosol properties critical for accurately evaluating the radiative impacts of aerosols on the global energy budget. Whereas previous satellite-based assessments are typically limited to daytime cloud-free measurements of aerosol properties, the 2B-FLXHR-LIDAR data product has the ability to quantify aerosol direct effects over thick clouds, under thin cirrus, and at night.

Using CloudSat 2B-FLXHR-LIDAR, we estimate the global annual mean aerosol direct effect to be $-1.9 \pm 0.6 \text{ W m}^{-2}$, which is in better agreement with previously published estimates from global models than previous satellite-based estimates. Detailed comparisons against a fully coupled simulation of the Community Earth System Model, however, reveal that this agreement on the global annual mean masks large regional discrepancies between modeled and observed estimates of aerosol direct effects. A series of regional analyses demonstrate that the magnitude and sign of these discrepancies are often related to model biases in the geographic and seasonal distribution of clouds. A low bias in stratocumulus cloud cover over the southeastern Pacific Ocean, for example, leads to an overestimate of the radiative effects of marine aerosols in the region. Likewise, errors in the seasonal cycle of low clouds in the southeastern Atlantic Ocean distort the radiative effects of

biomass burning aerosols from southern Africa. These findings indicate that accurate assessment of aerosol direct effects requires models to correctly represent not only the source, strength, and optical properties of aerosols, but their relative proximity to clouds as well.

The southeastern Atlantic Ocean is a perfect natural laboratory for investigating the absorptive properties of biomass burning aerosols. It is demonstrated using CloudSat 2B-FLXHR-LIDAR that underlying clouds in this region can enhance the solar absorption of carbonaceous aerosols by 50% and even self-loft aerosol layers under certain atmospheric conditions. Aerosol heating is found to peak at 0.6 ± 0.3 K/day at an altitude of 4 km in September when biomass burning aerosols reaches a maximum. The aerosol heating is shown to counter subsidence in this region by 10% on the annual mean, 20% from September-November, and 50% in September. However, for intense fire episodes the solar heating of the aerosol layer is likely sufficient to keep the layer self-lofting in the atmosphere. The presence of marine stratocumulus clouds provides the conditions necessary for biomass aerosols emitted in central Africa to be advected over the Atlantic Ocean where aerosols may be transported over long periods of time and over long distances. Results also show that poleward transport of absorbing aerosols can result in a more rapid ascent of aerosol layers due to enhanced solar heating in the summer hemisphere.

Finally, the ability of CALIPSO to distinguish aerosol layers by type has been leveraged to investigate the radiative impacts of individual aerosol components. Using a novel combined satellite/model approach, the contributions of various aerosols components are evaluated to estimate the direct radiative forcing (DRF) of anthropogenic aerosols. Aerosol DRF is computed using satellite-based radiative kernels that describe the sensitivity of shortwave fluxes in response to changes in aerosol optical depth. The combined 2B-FLXHR-LIDAR/SPRINTAR DRF is estimated to be -0.21 ± 0.05 W m⁻² with the largest contributions from polluted dust and continental aerosols (-0.240 W m⁻²) that is partially offset by a positive forcing from smoke aerosols ($+0.032$ W m⁻²). For the first time, satellite-based radiative kernels offer a tool to improve model simulations of aerosol-radiation interactions. Radiative kernels of aerosol properties also provide a tool for evaluating the radiative impacts of particulate emissions including wildfires, dust storms, and volcanic eruptions.

The results from these analyses provide new benchmarks on the global radiative effects of aerosols on the climate system and offer new insights for improving future assessments.

7.2 Broader impacts

Unlike greenhouse gases that are relatively long-lived and well mixed, aerosols have a short atmospheric lifetime that result in significant spatial and temporal variability (Feichter et al., 2004). Aerosols produced by human activity can produce strong localized impacts over industrialized countries, such as the United States and China. In both regions, aerosol direct effects exhibit a seasonal cycle that peaks in magnitude during summer. Similar seasonal trends are evident in 2B-FLXHR-LIDAR observations and CESM(CAM5) simulations. However, the magnitude of DRE at the top-of-atmosphere and surface is at least 50% weaker during most months in the CESM simulation as compared to 2B-FLXHR-LIDAR observations. As a result, DRE at the top-of-atmosphere is largely inconsistent between the two. Observed and simulated all-sky DRE exhibit differences over China (-2.8 W m^{-2} vs. -0.9 W m^{-2}) and USA (-2.2 W m^{-2} vs. -1.5 W m^{-2}). Over China, stronger DRE exists over urbanized areas in 2B-FLXHR-LIDAR observations but not in CESM simulations. Due to localized urban emissions, anthropogenic aerosols likely account for the stronger aerosol direct effects in observations compared to the model simulation.

7.3 Future work

The research presented in this study is intended to provide an overall assessment of aerosol direct effects using state-of-the-art satellite observations and model simulations. Evaluating aerosol radiative properties has greatly benefited in the past decade from improved technologies and techniques. Despite recent advances in aerosol observing and modeling capabilities, there is still much work to be done to improve characterization of aerosol radiative effects. Aerosols are composed of different components and each component may elicit a different response on climate. Since aerosol species have variable optical properties, it is important to understand the relative contribution from each aerosol type individually. Using the aerosol classification from CALIPSO, we

may evaluate 2B-FLXHR-LIDAR direct effects for various aerosol types, including marine, continental, dust, and smoke. It has been shown that the presence of both scattering and absorbing aerosol types may have competing effects over a given region. For example, over Southeast Asia it is believed that the cooling effect of industrial pollution and the warming effect of biomass burning smoke may partially cancel owing to competing effects. Sorting observed DRE by aerosol type may offer valuable insights into quantifying the contribution of anthropogenic aerosols on global and regional aerosol direct effects.

Evaluating uncertainty in the product and improving parameterizations of aerosol optical properties is a critical aspect of algorithm development. Working with modeling groups to test new parameterizations of aerosol sources and properties will greatly enhance the 2B-FLXHR-LIDAR algorithm. It has been demonstrated that the aerosol optical properties prescribed using the SPRINTARS global transport model strongly influence radiative transfer through the atmosphere. We plan to conduct sensitivity tests of retrieved single scattering albedo and asymmetry parameter and evaluate against in situ measurements from AERONET. There are known sources of uncertainty in the 2B-FLXHR-LIDAR product attributed to the aerosol retrievals from CALIPSO. In particular, the observational capabilities of CALIPSO lidar to distinguish aerosol types are limited. In the future, planned satellite missions (including EarthCARE and ACE) will feature advanced active sensing capabilities, such as high-spectral resolution lidar (HSRL), to achieve simultaneous measurements of scattering and extinction within a given profile. The unprecedented capabilities of spaceborne HSRL will further refine our understanding the taxonomy of aerosol types in the atmosphere and advance our knowledge of how various aerosol types interact with solar and terrestrial radiation.

The 2B-FLXHR-LIDAR algorithm may be improved upon to produce a more robust and realistic representation of the global energy budget. Future algorithm development plans also include using AIRS temperature and humidity sounding retrievals to reduce dependence on ECMWF analyses. However, it is worth noting that the source of temperature and humidity information has a negligible impact on estimates of aerosol DRE since this is derived from flux differences. In addition, the 2B-FLXHR-LIDAR algorithm would benefit from a further refinement of aerosol optical properties, specifically for smoke, dust, and polluted dust aerosols. Knowledge of global humidity fields from

ECMWF could provide the necessary constraints for representing the variable properties of water-coated aerosols. Furthermore, additional sensitivity studies can be performed to further investigate how changes in aerosol properties may affect radiative flux imbalances in future climate scenarios. Improved observational inputs will help advance our understanding of the radiative impact of aerosols. The regional slope of DRE versus AOD is another topic of interest that will be explored in greater detail as this analysis continues in the future.

Appendix

The Role of Cloud Phase in Earth's radiation budget

A.1 Introduction

The results presented in this chapter include work published by the author in a peer-reviewed journal (Matus and L'Ecuyer, 2017). Some of the methodology described in this section has been introduced in previous chapters in the interest of consistency. Many previous studies have contributed to this analysis and citations to these publications are included within the manuscript text.

Water in Earth's atmosphere exists in all three thermodynamic phases—liquid, ice, and vapor—with each phase playing a unique role in Earth's radiation budget. While the radiative effects of water vapor are fairly well understood (Soden and Held, 2006), clouds continue to represent a significant source of uncertainty in our ability to understand present-day energy flows and predict future climate (Randall et al., 2007; Flato et al., 2013). Beyond the need to accurately represent the global distribution of clouds, the radiative effects of clouds on shortwave (SW) and longwave (LW) radiation strongly depend on the cloud phase (Slingo, 1989; Fu and Liou, 1993). Clouds that form at temperatures warmer than 0°C can be assumed to contain only liquid droplets, while those found at temperatures colder than -40°C are generally composed entirely of ice crystals (Pruppacher et al., 1998). At temperatures between -40°C and 0°C, however, clouds may consist entirely of ice crystals, supercooled liquid water droplets, or a mixture of both (known as mixed-phase clouds), complicating estimates of their radiative effects. Simply changing liquid to ice near cloud top can, in turn, dramatically alter cloud albedo and lead to large differences in a cloud's impact on its environment (Forbes and Ahlgrimm, 2014; Kay et al., 2016).

Given their expansive coverage and wide range of radiative properties, mixed-phase clouds impact climate on a global scale. The presence of supercooled liquid in mixed-phase clouds is especially important since liquid water is more opaque to longwave radiation and increases cloud albedo more than ice crystals (Hogan et al., 2003). Supercooled liquid water has been observed globally in the atmosphere (Hogan et al., 2004; Verlinde et al., 2007; Hu et al., 2010) and, in

particular, at higher latitudes where it is a significant driver of radiative fluxes (Cesana et al., 2012; van Tricht et al., 2016). Despite their importance in the global energy budget, however, it has been shown that supercooled liquid water clouds are often underestimated in global climate models (GCMs) (Komurcu et al., 2014; Cesana et al., 2015; McIlhattan et al., 2017). Furthermore, mixed-phase clouds may have an even greater role in a future climate as increasing greenhouse gas concentrations are expected to change not only the spatial coverage of mixed-phase clouds but also their ice-liquid partitioning (Komurcu et al., 2014). An increase in cloud optical depth poleward of 45° appears to be a robust response to warming in GCMs and has been attributed to a transition from ice-dominated to liquid-dominated mixed-phase clouds (Tsushima et al., 2006; Zelinka et al., 2013; Komurcu et al., 2014; McCoy et al., 2015). Given the sensitivity of GCMs to cloud water phase, a more realistic representation of phase partitioning is critical for establishing confidence in such cloud feedback estimates in future climate simulations.

Mixed-phase clouds are often crudely represented in global models that oversimplify the complex microphysical processes that influence transitions between liquid and ice (Prenni et al., 2007). Phase transition mechanisms including nucleation, secondary ice formation, and the Bergeron-Findeisen process remain poorly represented as a result (Atkinson et al., 2013; Murray et al., 2013; Cesana et al., 2015). Constraining these phase transition mechanisms is particularly challenging since the physics and dynamics of mixed-phase clouds are nonlinear (Morrison et al., 2011). McCoy et al. (2015) showed that 19 models from the Coupled Model Intercomparison Project phase 5 are effectively partitioning ice and liquid as a monotonic function of temperature, which is found to contribute a substantial amount of variance in cloud fraction and liquid water path (LWP) in models. Such oversimplifications in cloud-phase partitioning can lead to significant errors when calculating cloud radiative effects in a climate model (Gettelman et al., 2007; Storelvmo et al., 2008). The role of low cloud feedback over the Southern Ocean, for example, is a significant source of bias and disagreement among global climate models (Bony et al., 2006; Vial et al., 2013). It is critical that the representation of cloud phase is correctly simulated in climate models in order to adequately understand energy flows in the atmosphere both globally and regionally. Despite the climatic importance of mixed-phase clouds over the Southern Ocean, localized high-quality observations of

these clouds are sparse and infrequent which limits the information available for evaluating and improving model parameterizations.

In fact, our understanding of the global impacts of mixed-phase clouds in general is limited due to sparse observations. Research aircraft and ship-based instrumentation can measure supercooled droplets on regional scales but fail to adequately characterize their microphysical properties on global scales. Satellite-based remote sensing methods provide the necessary coverage for continuous monitoring of mixed-phase clouds on larger scales (Miller et al., 2014). Since supercooled liquid tends to reside near cloud top, there is a distinct advantage to viewing mixed-phase clouds from above using satellite (Rauber and Tokay, 1991). However, while conventional passive sensors provide information about the presence of liquid water near cloud top, they often lack critical information about cloud composition below this liquid layer in optically thick or multilayered clouds. Recent studies investigating the global radiative effects of mixed-phase clouds have noted that this failure to observe the vertical distribution of cloud optical properties remains one of the largest uncertainties in quantifying cloud radiative effects on global scales (Randall et al., 2007; Hogan et al., 2004; Hu et al., 2010).

This study addresses these limitations by leveraging actively sensed cloud profile data from CloudSat and the Cloud-Aerosol Lidar and Infrared Pathfinder Satellite Observation (CALIPSO) in combination with the Moderate Resolution Imaging Spectroradiometer (MODIS). Section A.2 describes updates in the new release of the CloudSat level 2 radiative fluxes and heating rates algorithm (2B-FLXHR-LIDAR) that include an improved representation of supercooled liquid water clouds, thin ice clouds, and surface albedo. In section A.3, the performance of 2B-FLXHR-LIDAR is evaluated using collocated SW and LW flux observations from the Clouds and the Earth's Radiant Energy System (CERES) (Kato et al., 2010). Flux estimates from 2B-FLXHR-LIDAR are then used to investigate the radiative impacts of clouds over the pre-anomaly phase of the CloudSat mission (2007–2010). This time period has been selected since, after the April 2011 battery anomaly, only daytime observations are available, and the alignment of CloudSat and CALIPSO footprints is slightly degraded. Section A.4 quantifies global cloud radiative effects and the relative contributions from liquid, ice, or mixed-phase clouds. Mixed-phase cloud radiative effects, in particular, are

highlighted in sections A.5 and A.6 that documents the seasonal and regional patterns of mixed-phase clouds and assesses their implications for global heat transport. A discussion of key points from this paper is provided in section A.7.

A.2 New updates to 2B-FLXHR-LIDAR

The 2B-FLXHR-LIDAR algorithm estimates vertically resolved fluxes and heating rates consistent with retrieved cloud properties from CloudSat, CALIPSO, and MODIS (L'Ecuyer et al., 2008; Henderson et al., 2013). Algorithm inputs include CloudSat retrievals of liquid and ice water contents and effective radii, temperature and humidity profiles from European Centre for Medium-Range Weather Forecasts analyses, and seasonally varying surface albedo and emissivities using land surface classification data provided by the International Geosphere-Biosphere Programme. Snow and ice cover are identified using collocated passive microwave observations from Advanced Microwave Scanning Radiometer–EOS provided by the National Snow and Ice Data Center. These inputs initialize broadband radiative flux calculations in a two-stream, plane-parallel, adding-doubling radiative transfer model (Ritter and Geleyn, 1992) to compute fluxes in 6 shortwave and 12 longwave bands. Resulting fluxes are output for each CloudSat footprint at a vertical resolution of 240 m.

The fifth release (R05) 2B-FLXHR-LIDAR data set makes several significant advances over the previous version (R04) described in Henderson et al. (2013, hereafter H13). The new algorithm features improved land, snow, and sea ice albedos using spectral measurements from Zatko and Warren (2015), a more realistic representation of the zenith angle dependence of ocean albedo, an explicit representation of lidar-detected supercooled liquid water clouds, and a more rigorous treatment of thin ice clouds that includes explicit retrievals of ice water content (IWC) and effective radii from the CloudSat 2C-ICE data product (Deng et al., 2013). These improvements incorporate better physical assumptions and yield better agreement relative to validation data sets. As with any remote sensing-based data set, however, a number of limitations remain including retrieval errors and sampling biases that result from the spatial and temporal sampling characteristics of CloudSat and CALIPSO. While CloudSat is more sensitive to optically thick clouds and CALIPSO is better suited

at detecting optically thin clouds, it is likely that some cloud features may go undetected by both sensors. CALIPSO may fail to detect very thin liquid layers ($LWP < 5 \text{ g m}^{-2}$) and may miss layers in clouds below optically thick ice layers above (Christensen et al., 2013). Since CALIPSO lidar may be attenuated by optically thick supercooled liquid layers which prevents the detection of underlying ice layers, CALIPSO may miss mixed-phase clouds over polar regions where supercooled-topped mixed-phase clouds are common (Morrison et al., 2011; Cesana et al., 2012). The influence of these uncertainties on the results will be evaluated through a combination of sensitivity studies and comparisons against independent top-of-atmosphere (TOA) flux data sets in section 3.

A.3 Algorithm performance

To evaluate the performance of the 2B-FLXHR-LIDAR flux product, estimates of SW and LW fluxes at the TOA are compared with CERES single scanner footprint (SSF) fluxes reported in the CALIPSO, CloudSat, CERES, and MODIS (C3M) product (Kato et al., 2010). The CERES instrument aboard Aqua provides a long-term, continuous data set of high-quality SW and LW fluxes. Since the Aqua satellite orbits closely with CloudSat and therefore views nearly identical atmospheric conditions, the CERES SSF product is a particularly valuable tool for validating 2B-FLXHR-LIDAR fluxes. As previously shown, Figure 3.1 compares TOA albedo in clear-sky and all-sky scenes from CERES with 2B-FLXHR-LIDAR estimates from both the R04 and R05 versions of the algorithm. It is found that the R04 version of 2B-FLXHR-LIDAR exhibits significant clear-sky biases over most land surfaces and most notably over deserts, forests, and tundra. In the new R05 version, corrections to land and ocean surface reflectances have reduced the global mean bias by over 40% in clear-sky scenes, resulting in a TOA albedo offset of just -0.7%. Regionally, these biases in clear-sky albedo have been improved in the 2B-FLXHR-LIDAR product by as much as 20% over Greenland and Antarctic ice sheets, 10% over tropical forests, and 5% over deserts.

All-sky biases have also been reduced in R05 through the improved representation of mixed-phase clouds and thin cirrus. In particular, the positive bias over subtropical ocean has been improved from 4 W m^{-2} in R04 to 1 W m^{-2} in R05, while the negative bias over the Southern Ocean has been

improved from -6 W m^{-2} to -2 W m^{-2} , primarily due to the explicit detection of supercooled liquid in the new R05 2B-FLXHR-LIDAR algorithm. The spatial structure of albedo in R05 has improved significantly over the entire globe and especially over polar regions where much attention has been given toward better understanding the surface energy budget (Verlinde et al., 2007; Christensen et al., 2016). Overall, clear-sky and all-sky albedo estimates compare favorably between CERES and R05, with global annual mean differences less than 1%.

Similar comparisons of outgoing longwave radiation (OLR) are shown in Figure 3.2. There are two significant changes in R05 affecting OLR: (1) updating greenhouse gas concentrations to 2010 levels and (2) including explicit retrievals of IWC and effective radius from 2C-ICE. Increasing carbon dioxide concentrations from 330 ppm in R04 to 390 ppm in R05 results in a global reduction in clear-sky OLR of -1.3 W m^{-2} . This reduction in OLR helps to improve the positive bias observed at higher latitudes. The addition of 2C-ICE retrievals in R05 increases all-sky OLR over the tropics, offsetting a negative bias resulting from increased greenhouse gas concentrations in that region. While all-sky OLR biases have increased slightly to 9 W m^{-2} at higher latitudes, biases are similar to R04 elsewhere and even exhibit a slight improvement over the equatorial Pacific.

Root-mean-square (RMS) differences between annual mean fluxes at $2.5^\circ \times 2.5^\circ$ spatial resolution from 2B-FLXHR-LIDAR and CERES are shown in Figure 3. The RMS differences in clear-sky outgoing shortwave radiation (OSR) are 7.5 W m^{-2} , while those for OLR are 2.8 W m^{-2} . Higher RMS differences in SW fluxes can be attributed to the larger diurnal range in solar insolation (0 to 450 W m^{-2}) compared to that of thermal emission (200 to 450 W m^{-2}). The RMS differences for all-sky OSR and OLR are 8.9 W m^{-2} and 4.9 W m^{-2} , respectively, which improve upon R04 values of 16.5 W m^{-2} and 5.7 W m^{-2} reported in H13. The larger spread in flux values from all-sky scenes compared to clear-sky scenes is attributed to uncertainties in cloud microphysical property retrievals and cloud detection differences between the larger CERES and smaller CloudSat fields of view. Overall, biases in OSR and OLR are less than 4 W m^{-2} in both clear-sky and all-sky scenes. While R05 generally underestimates TOA fluxes compared to CERES, these differences are consistent with anticipated uncertainties in CERES fluxes themselves (Loeb et al., 2012).

It should be noted that uncertainties in any observational quantity derived from an algorithm like 2B-FLXHR-LIDAR may vary with the time and space scales of interest. Furthermore, due to structural errors from the myriad of assumptions required in the calculations, uncertainties on every scale are a sum of random and systematic components (L'Ecuyer et al., 2015). L'Ecuyer et al. (2008) showed that uncertainties in fluxes derived from the original 2B-FLXHR algorithm decreased on longer time scales and this also holds true for the current 2B-FLXHR-LIDAR product. Table 3.1 compares fluxes from R05 relative to CERES computed over a range of time and spatial scales. While spatial averaging has a negligible impact for the range of scales considered (2.5° to 10°), the RMS differences in SW and LW fluxes decrease systematically with increasing temporal averaging as a result of reduced random errors. The RMS differences in OSR at 2.5° resolution, for example, decrease from 13.8 W m^{-2} for monthly averaging to 8.9 W m^{-2} for annual averaging. For LW fluxes, though, the change in RMSE from monthly to annual averaging is considerably less than that for SW fluxes. This highlights the importance of considering time-space scale averaging when interpreting 2B-FLXHR-LIDAR analyses of SW and LW fluxes.

While many approaches of varying complexity have been introduced for classifying clouds, we adopt an approach that simply partitions clouds according to phase. This approach not only avoids the use of subjective thresholds but also relates more directly to prognostic fields in numerical models, potentially offering a more direct means of evaluating their representation in models. The new R05 2B-FLXHR-LIDAR algorithm features a robust cloud phase classification, improving upon previous versions that assumed a linear partitioning of liquid and ice water in cloud layers with temperatures between -20°C and 0°C (L'Ecuyer et al., 2008). The R05 2B-FLXHR-LIDAR algorithm explicitly identifies cloud phase (liquid, ice, or mixed) in each layer of a scene using the 2B-CLDCLASS-LIDAR cloud phase classification described in Sassen and Wang (2012). The 2B-CLDCLASS-LIDAR product combines CloudSat radar and CALIPSO lidar measurements to distinguish cloud phase using signal intensity differences between liquid and ice particles. While CloudSat's Cloud Profiling Radar is particularly sensitive to cloud liquid droplets, CALIPSO's CALIOP has a greater sensitivity to smaller ice particles. Together, both radar and lidar measurements improve overall cloud detection and provide information necessary for cloud phase

classification in the 2B-CLDCLASS-LIDAR product. In this study, a mixed-phase cloud refers to any contiguous cloud layer in which both liquid and ice phases are identified according to the 2B-CLDCLASS-LIDAR cloud phase classification. If more than one cloud phase is identified in multiple distinct cloud layers, then that scene is classified as a multilayered (ML) cloud system.

Table 3.2 summarizes comparisons of 2B-FLXHR-LIDAR and CERES fluxes categorized by scene type. Biases and RMS differences are reported as percent differences relative to CERES. Overall, clear-sky fluxes exhibit good agreement between 2B-FLXHR-LIDAR and CERES with a net bias and RMSE of less than -0.9% and 2.8% , respectively. Fluxes in cloudy scenes have slightly higher biases and spreads that can be attributed to cloud retrieval and detection differences in CERES and CloudSat/CALIPSO. In particular, the 20 km CERES scanner footprint is considerably larger than CloudSat's cross-track resolution of 1.4 km. Owing to sampling issues discussed previously, cloudy-sky fluxes exhibit better agreement in the LW than in the SW. Scenes with liquid phase clouds have a relatively low RMS of 2.2% for OLR fluxes but a higher RMS of 16.9% for OSR. This may be partially explained by differences in the fields of view of CloudSat and CERES, particularly over spatially heterogeneous clouds such as broken stratocumulus. By comparison, scenes with mixed-phase clouds have RMS differences of 8.4% and 12.7% in OLR and OSR, respectively. Given that the level of agreement in SW and LW fluxes varies by the type of cloud present in a given scene, it is important to consider the scene type when assessing the accuracy of fluxes from 2B-FLXHR-LIDAR.

A.4 Global cloud radiative effects

The radiative impact of clouds depends not only on their geographic location but also on their composition. Figure 4 displays the annual mean frequencies of occurrence of liquid, ice, and mixed-phase clouds from CloudSat/CALIPSO observations over 2007–2010. Cloud occurrence is computed as the fractional coverage of each 2B-CLDCLASS-LIDAR cloud phase gridded at $2.5^\circ \times 2.5^\circ$ spatial resolution. A crude estimate of the diurnal variability in cloud occurrence provided in Figure 4 (right column) displays the day-night differences in cloud fraction obtained by differencing the A-Train

1:30 P.M. and 1:30 A.M. overpasses. It should be noted that CALIPSO may detect fewer weakly scattering clouds during daytime than at night due to higher solar background noise (Chepfer et al., 2013), although this is not expected to affect the detection of optically thick liquid-containing clouds. While the twice-daily sampling of the A-Train does not provide complete sampling of diurnal variations in cloud cover, this comparison of daytime and nighttime overpasses suggests that mixed-phase clouds exhibit much weaker diurnal variations than other cloud types.

Mixed-phase clouds are considerably less common than those consisting entirely of ice or liquid water. Clouds identified as mixed-phase are observed globally in 7.7% of CloudSat/CALIPSO profiles and account for about one tenth of the total global cloud fraction of 73%. While frequently observed at higher latitudes in both hemispheres, these clouds are most prevalent over the Southern Ocean. Unlike pure liquid or ice clouds that exhibit distinct patterns of diurnal variation, mixed-phase clouds generally occur with equal frequency during daytime and nighttime overpasses. The only exception is over the Greenland and Antarctic ice sheets where mixed-phase clouds are observed twice as frequently during the day than at night. This result, however, is due to the extreme temperature differences between day and night in the Arctic, where the Sun is present for 6 months in summer and absent for 6 months during polar night. At high latitudes, mixed-phase clouds are less common during winter months as colder temperatures limit the presence of supercooled liquid water. The impact of clouds on radiative fluxes is commonly quantified in a metric known as cloud radiative effect (CRE):

$$CRE = (F^\downarrow - F^\uparrow)_{all-sky} - (F^\downarrow - F^\uparrow)_{clear-sky} \quad (11)$$

where F^\downarrow and F^\uparrow are downwelling and upwelling fluxes, respectively, and subscripts denote all-sky and clear-sky conditions. Figure 5 displays global maps of SW, LW, and net CRE at the TOA based on four years (2007–2010) of R05 2B-FLXHR-LIDAR estimates. While it is well known that cloud phase significantly influences the radiative effects of clouds, the spatial patterns of CRE do not necessarily follow those of cloud phase. On the annual mean, clouds cool the planet by 17.1 W m^{-2} by reflecting 44.2 W m^{-2} of SW radiation and retaining 27.1 W m^{-2} in the LW. These results are

comparable to the CERES estimate of -18.2 W m^{-2} reported in Allan (2011) but somewhat less negative than the -24.2 W m^{-2} estimate from the International Satellite Cloud Climatology Project data sets (Zhang et al., 2004). While these differences in CRE estimates may be due to differences in detecting clouds and assigning optical properties, it should also be noted that CRE is computed as the difference between two sets of large numbers that can introduce significant uncertainty in the resulting estimates.

The strongest SW effects occur over the Intertropical Convergence Zone (ITCZ) where the greatest contributions are from multilayered cloud systems, as previously identified by Lü et al. (2015). Shortwave CRE is also strong over the eastern subtropical ocean where liquid clouds reflect in excess of -80 W m^{-2} on the annual mean. Longwave effects are equally strong over the ITCZ with large contributions from both multilayered and ice clouds, resulting in a near cancellation of LW and SW CRE over the tropical west Pacific, as noted previously by Kiehl et al. (1994). Radiative effects in the LW are particularly strong for ice clouds over the tropics. Globally, ice clouds exert a positive net radiative effect of 3.5 W m^{-2} , whereas liquid (-11.8 W m^{-2}), mixed-phase (-3.4 W m^{-2}), and multilayered clouds (-5.4 W m^{-2}) all induce net negative radiative effects. As a result, clouds exert a net cooling effect over much of the planet, except over polar ice sheets and equatorial Africa where LW heating dominates SW cooling. On the global annual mean, liquid phase clouds are found to contribute nearly 70% of the net radiative effect and, as a result, represent the single largest source of cooling in Earth's energy budget.

Cloud effects at the surface can be stronger than those at the TOA due to the additional contribution of absorption. Figure 6 shows the global distributions of CRE at the surface (SFC) for each cloud phase. Overall, clouds reduce surface fluxes by 24.9 W m^{-2} on the global annual mean by reducing SW fluxes by 51.1 W m^{-2} and increasing LW fluxes by 26.2 W m^{-2} . Cloud interactions with solar radiation are therefore 16% stronger at the surface than the TOA. Since clouds generally absorb less radiation in the SW than LW, the spatial patterns of SW CRE are similar at the TOA and surface. LW CRE, however, exhibits a substantially different spatial pattern at the surface. Larger radiative effects tend to be observed at higher latitudes for all cloud phases. The largest contribution to LW CRE is from liquid clouds that have a radiative impact of 8.6 W m^{-2} at the surface. For all cloud

types, though, the negative SW effects dominate over the positive LW effects resulting in a negative net CRE at the surface.

The difference between CRE at the TOA and surface provides an estimate of the cloud impact on atmospheric (ATM) heating, representing the amount of radiative energy gained within the atmospheric column. The global distributions of ATM CRE for liquid, ice, mixed-phase, and multilayered clouds are displayed in Figure 7. Results show that most clouds slightly enhance SW heating. Liquid and ice clouds exhibit comparable SW absorption on the global average, even though ice clouds absorb nearly exclusively over land surfaces. In the LW, liquid phase clouds exert a negative ATM CRE meaning they cool the atmospheric column. By comparison, clouds containing ice crystals tend to warm the atmosphere in equatorial regions and cool the atmosphere at higher latitudes. Overall, clouds are found to heat the atmosphere by 7.8 W m^{-2} on the global annual mean. The largest contribution to this heating is from ice clouds contributing over 70% of the total heating.

Table 3 summarizes the 2B-FLXHR-LIDAR estimates of TOA, SFC, and ATM CRE. The upper panel documents the global mean CRE for each cloud phase, while the lower panel displays the CRE differences between Northern Hemisphere (NH) and Southern Hemisphere (SH). The most striking result is that liquid clouds exert a radiative effect at the TOA that is 7 W m^{-2} stronger in the SH owing to their higher frequency particularly over the Southern Ocean. Other cloud phases exhibit negligible hemispheric differences. This implies that the observed similarity between the NH and SH radiation budgets (Wild et al., 2014; Stephens and L'Ecuyer, 2015) is primarily a result of a near cancelation of the effects of increased land mass in NH and increased low cloud fraction in the SH.

A.5 Effects of mixed-phase clouds

A.5.1 Global distribution

Figure 4 shows that cloud occurrence and cloud radiative effects vary greatly by latitude. This is particularly true for mixed-phase clouds. The distribution of mixed-phase clouds and their radiative effects vary not only by region but also by season. Figure 8 presents zonal annual mean cloud fraction (top), TOA CRE (middle), and surface CRE (bottom). The left column distinguishes the

relative contributions from each cloud phase (liquid, ice, mixed phase, and multilayered), while the right column displays the seasonal averages from mixed-phase clouds only. CloudSat/CALIPSO observations indicate that clouds are most frequently observed over the Southern Ocean around 60°S. Mixed-phase clouds are also most common in this region with an observed annual mean frequency of 23%. This region features unique cloud processes due to its relative remoteness from anthropogenic and natural continental aerosol sources (McCoy et al., 2015). During the southern hemisphere summer (December–February (DJF)) the occurrence of mixed-phase clouds exceeds 28% over the Southern Ocean and the TOA and surface CRE over this region reach peak values of -34 W m^{-2} and -28 W m^{-2} , respectively. By contrast, mixed-phase clouds over the Southern Ocean are observed less frequently during the southern hemisphere winter (June–August (JJA)) when the radiative effects at the TOA and surface are positive due to the presence of sea ice over this region. Seasonal variability is also observed in the Northern Hemisphere but to a lesser degree compared to the Southern Hemisphere.

The seasonal variability of mixed-phase cloud radiative effects is further illustrated in Figure 9, which shows the seasonal and annual mean TOA CRE of mixed-phase clouds from R05 2B-FLXHR-LIDAR over 2007–2010. Comparable maps of CRE at the surface are displayed in Figure 10. The annual mean net TOA CRE from mixed-phase clouds is -3.4 W m^{-2} (-8.1 W m^{-2} from SW and 4.7 W m^{-2} from LW). The largest SW effects are observed in the summer hemisphere which strongly influences the global distribution of net CRE. In DJF, the net CRE from mixed-phase clouds exceeds -20 W m^{-2} over the Southern Ocean. However, in JJA there is a stronger signal from the Northern Hemisphere ITCZ in the LW CRE which partially offsets some of the SW CRE in the Northern Hemisphere. The net CRE from mixed-phase clouds in JJA is -2.3 W m^{-2} , as a result, which is over 40% weaker than in DJF. Over bright surfaces the greenhouse effect of mixed-phase clouds predominates over the albedo effect to yield a positive net mixed-phase CRE over the Southern Ocean.

A.5.2 Implications for heat transport

The significance of zonal and seasonal variations in mixed-phase cloud occurrence becomes evident in Table 4 that summarizes how their impacts on energy are partitioned between the atmosphere and ocean. The contributions of mixed-phase clouds to net heat fluxes at the top of atmosphere, surface, and in atmosphere in each latitude zone are computed by weighting the mean CRE by appropriate areas of each band. The results are expressed in units of terawatts (TW or 10^{12} W) and represent the net contribution of mixed-phase clouds to energy imbalances at each latitude. These heat fluxes modify equator-to-pole temperature gradients that drive atmospheric circulations so the TOA, ATM, and SFC panels of Table 4 represent the impact of mixed-phase clouds on net, atmospheric, and oceanic heat transports, respectively. A positive (negative) heat flux denotes a net gain (loss) of energy in the relevant region.

The top panel of Table 4 demonstrates that on the annual mean mixed-phase clouds enhance net poleward heat transport in both hemispheres by cooling high latitudes ($40\text{--}60^\circ$) more effectively than lower latitudes relative to clear-sky conditions. This effect is strongest in the Southern Hemisphere where mixed-phase clouds cool the Southern Ocean 4 times more than the equator, resulting in a stronger poleward circulation in local summer months. In winter the impact of mixed-phase clouds reverses owing to their warming influence at high latitudes when solar insolation is weaker and implying that mixed-phase clouds moderate poleward heat transport in local winter. Similar but muted effects are observed in the Northern Hemisphere where the seasonal amplitude of net CRE is about half that over the Southern Ocean. This integrated top-of-atmosphere perspective, however, masks important competing impacts of mixed-phase clouds on atmospheric and oceanic heat transport. Within the atmosphere, mixed-phase clouds exert a decidedly positive heat flux in the tropics and a negative heat flux poleward of 60° in all seasons. This augments existing energy imbalances and implies that mixed-phase clouds significantly enhance the atmospheric heat transport from tropics to poles. These impacts are particularly strong in the summer hemisphere as shown in the center panel of Table 4.

The implied enhancement of atmospheric poleward heat transport is partially compensated by an opposite effect in the ocean surface. The stronger reduction of heat fluxes into the tropical oceans relative to higher latitudes especially during the winter months partially reduces the natural zonal gradient in sea surface temperature relative to clear conditions. When coupled with known ocean circulation patterns, this suggests that mixed-phase clouds reduce poleward heat transport in the oceans but, in contrast to the atmospheric heat transport, these effects are maximum in the winter hemisphere. It will be demonstrated below that these offsetting effects of mixed-phase clouds find their origins in differences in the distribution of precipitating and non-precipitating mixed-phase clouds between the tropics and higher latitudes.

A.6 Mixed-phase cloud regimes

It is important to note that the definition adopted here for mixed-phase clouds is comprehensive and includes all clouds in which both phases exist. The sensors aboard CloudSat and CALIPSO are sensitive to a wide range of mixed-phase clouds, from the traditional definition of non-precipitating mixed-phase clouds consisting of a liquid layer at the top and ice precipitating from below to stratiform and convective precipitation that consist of snow aloft, rain at low levels, and varying mixtures of liquid and ice cloud water throughout. The 2B-FLXHR-LIDAR product has the unique capability to quantify the contributions of each of these types of mixed-phase clouds to global CRE, as shown in Figure 11 (left column). Precipitating or non-precipitating scenes are identified for each profile using CloudSat's 2C-PRECIP-COLUMN, which performs retrievals of precipitation occurrence and intensity based on near-surface radar reflectivity and estimates of path-integrated attenuation (Haynes et al., 2009). Non-precipitating mixed-phase clouds account for over 65% of the total radiative impact at the TOA. The impact of non-precipitating clouds is considerably greater at higher latitudes and about twice as strong in the Southern Hemisphere than the Northern Hemisphere. At the surface, however, precipitating clouds have larger radiative effects than non-precipitating mixed-phase clouds in the tropics. Poleward of 70°, however, precipitating clouds have a negligible radiative effect, while non-precipitating clouds exert a warming effect in excess of 2 W m^{-2} .

Vertically resolved measurements from CloudSat and CALIPSO also have the capability to distinguish stratiform mixed-phase clouds from their more convective counterparts whose origins can be traced to more turbulent mixing in stronger updrafts. While the majority of mixed-phase clouds at higher latitudes are non-convective in nature, tropical mixed-phase clouds are predominantly associated with convection. Figure 11 (right column) shows the partitioning of mixed-phase cloud radiative effects by their contributions from convective and non-convective regimes. Convective clouds are defined in this study as those identified by the 2B-CLDCLASS-LIDAR dataset as nimbostratus or deep convection cloud type classifications, while all other clouds are identified as non-convective. Based on these criteria, the global annual mean radiative effect of convective mixed-phase clouds at TOA is -0.9 W m^{-2} or 28% of the total. Similar to precipitating mixed-phase clouds, however, convective clouds exert a greater radiative effect at the surface than the TOA. Convective mixed-phase CRE at the surface is -2.7 W m^{-2} and accounts for 59% of the total. It follows that mixed-phase clouds observed in the tropics are primarily convective systems that are raining, whereas those nearer the poles are generally non-convective and non-precipitating.

A.7 Summary

The partitioning of water between its liquid and ice phases plays an important yet not fully understood role in the global energy budget. Mixed-phase clouds are of particular interest given their strong and variable impact on the TOA and surface energy budget at higher latitudes. While previous studies have assessed the radiative effects from mixed-phase clouds, a lack of adequate observations of cloud vertical structure may limit the fidelity of these estimates. We present a new assessment of the global radiative effect of mixed-phase clouds using the fifth release CloudSat fluxes and heating rates (R05 2B-FLXHR-LIDAR) product. The R05 2B-FLXHR-LIDAR product, which combines collocated CloudSat, CALIPSO, and MODIS observations to compute vertically resolved profiles of shortwave and longwave radiative fluxes, features an improved representation of cloud phase over previous versions. Our approach employs a relatively straightforward classification of cloud profiles into liquid, ice, mixed-phase, and multilayered scenes using CloudSat and CALIPSO observations.

The combination of CloudSat and CALIPSO provides vertically resolved cloud measurements critical to filling in existing gaps in cloud partitioning and better constraining global estimates of cloud radiative effects. Simply partitioning these observations by cloud phase avoids some of the inherent ambiguity associated with more complicated cloud classifications, relates more closely to the raw observations, and can more easily be compared to prognostic fields in models.

While this study documents global estimates of cloud radiative effect for all water phases, mixed-phase clouds are of particular interest. Mixed-phase clouds are observed most frequently at higher latitudes, where they are efficient at reflecting solar radiation back to space and exert a negative radiative effect at the TOA. At the surface, however, the strongest mixed-phase CRE is from precipitating convective clouds in the tropics where SW cooling dominates LW heating. Over ice-covered surfaces such as Greenland and West Antarctica where SW effects are small, LW heating from non-precipitating mixed-phase clouds dominates resulting in a strong positive net radiative effect at the surface. Mixed-phase clouds are found to exert a global net cloud radiative effect of -3.4 W m^{-2} , with contributions of -8.1 W m^{-2} and 4.7 W m^{-2} in the SW and LW, respectively. Interestingly, mixed-phase clouds contribute over 20% of the total cloud radiative effect despite making up only 10% of the total cloud occurrence. When compared with the effects of liquid clouds (-11.8 W m^{-2}), ice clouds (3.5 W m^{-2}), and multilayered clouds with distinct layers of liquid and ice (-5.4 W m^{-2}), these results confirm that accurate representation of mixed-phase clouds is essential for quantifying cloud feedbacks in future climate scenarios. This is particularly apparent over the Southern Ocean, where mixed-phase clouds are found to account for more than 35% of the net reduction of absorbed SW radiation at the surface in the local summer. Recent modeling studies have suggested that this can have important implications for atmospheric and oceanic circulations on global scales (Komurcu et al., 2014; Cesana et al., 2015).

This is illustrated conceptually in Figure 12 that presents a schematic showing the locations where mixed-phase clouds occur and their influence on large-scale circulations. The annual occurrences of mixed-phase clouds (purple), liquid only clouds (red), and ice only clouds (blue) are computed globally at 480 m vertical resolution based on the 2B-CLDCLASS-LIDAR cloud phase classification data from 2007 to 2010. For illustrative purposes, gray outlines indicate the boundaries

of idealized cloud structures and the canonical atmospheric flow patterns from the Hadley, Ferrel, and Polar cells are indicated by black arrows for context (Wallace and Hobbs, 2006). Areas of rising air loosely coincide with regions of increased cloudiness, especially convective mixed-phase clouds. As previously shown in Figure 4, mixed-phase cloud systems are indeed most frequent over the tropics and upper mid-latitudes. Multilayered clouds are also quite common over these regions and, most notably in the tropics, where high cirrus is often observed above liquid or mixed-phase convective cloud systems. In regions of large-scale subsidence, liquid clouds dominate but mixed-phase clouds are frequently observed at polar latitudes.

Results from this study provide key observational benchmarks that can be used to improve climate model simulations of cloud radiative effects. It is important to note, however, that several important sources of uncertainty remain in these estimates. Most notably, it remains difficult to accurately partition water between its liquid and ice phases in layers where they coexist. Diurnal sampling limitations and assumed surface reflection characteristics may also influence the results. The approximate magnitude of these uncertainties has been quantified, to the extent possible, through cloud regime-specific comparisons against CERES TOA fluxes in Table 2. These comparisons suggest that the resulting uncertainties in the annual mean radiative effects of mixed-phase clouds presented here are 10–15%.

Overall, mixed-phase clouds are found to heat the tropical atmosphere by increasing the greenhouse effect and cool the polar atmosphere by enhancing longwave emission to the surface. This suggests that mixed-phase clouds increase the equator-to-pole temperature gradient and act to reinforce large-scale poleward atmospheric heat transport. The opposite is true in the oceans where convective mixed-phase clouds cool the tropical ocean, but non-precipitating non-convective mixed-phase clouds slightly warm the surface in the Arctic and Antarctic. This weakens the equator-to-pole temperature gradient in the ocean and, when combined with ocean circulation patterns, likely reduces oceanic poleward heat transport in the annual mean. These results support recent modeling studies that have demonstrated the importance of cloud phase partitioning for accurately representing large-scale atmospheric and oceanic circulations (Kay et al., 2016; Storelvmo et al., 2008).

		TOA CRE			SFC CRE			ATM CRE		
		SW	LW	Net	SW	LW	Net	SW	LW	Net
Global	Liquid	-14.6	2.8	-11.8	-16.5	8.6	-8.0	1.9	-5.8	-3.9
	Ice	-5.8	9.3	3.5	-7.5	5.3	-2.2	1.7	4.1	5.7
	Mixed	-8.1	4.7	-3.4	-9.1	4.3	-4.8	0.9	0.4	1.4
	ML	-15.7	10.3	-5.4	-18.0	8.1	-9.9	2.4	2.2	4.5
	Total	-44.2	27.1	-17.1	-51.1	26.2	-24.9	6.9	0.9	7.8
NH-SH	Liquid	7.0	-1.2	5.8	7.0	-4.5	2.5	-0.2	3.4	3.3
	Ice	-0.6	1.7	1.1	-1.9	1.1	-0.8	1.3	0.5	1.9
	Mixed	0.9	0.2	1.1	0.6	-0.6	0.1	0.3	0.7	1.0
	ML	0.5	0.3	0.8	-0.3	-0.6	-0.9	0.9	0.9	1.7
	Total	7.8	1.0	8.8	5.4	-4.5	0.9	2.4	5.5	7.8

Table A.1: Summary of phase-separated global mean cloud radiative effects (top) and differences between the northern and southern hemispheres (bottom), in W m^{-2} . Both SW and LW effects from liquid, ice, mixed-phase, and multilayered clouds are computed at the top of atmosphere (TOA), surface (SFC), and within the atmospheric column (ATM). All data presented are from 2B-FLXHR-LIDAR, 2007–2010.

Heat flux from mixed-phase clouds (TW)

		Jan	Feb	Mar	Apr	May	Jun	Jul	Aug	Sep	Oct	Nov	Dec	Ann		
TOA	80N	38	23	-35	-118	-305	-401	-298	-225	-91	46	69	49	-104	80N	
	40N	34	-106	-328	-510	-585	-546	-424	-302	-206	-98	18	80	-248	40N	
	Eq	-65	-164	-169	-249	-261	-251	-240	-194	-150	-92	-40	-21	-158	Eq	
	Eq	-113	-119	-118	-126	-165	-191	-236	-286	-205	-135	-120	-80	-121	Eq	
	40S	-225	-234	-152	-97	-49	-35	-46	-68	-81	-141	-165	-159	-171	40S	
	80S	-287	-253	-144	-73	-9	29	-14	-89	-224	-307	-351	-328	-492	80S	
	80S	-1073	-820	-464	-139	74	165	94	-102	-470	-840	-1156	-1168	-153	80S	
	80S	-524	-429	-149	4	51	45	33	16	-37	-121	-290	-436	-153	80S	
ATM	80N	-129	-139	-100	-106	-147	-68	-23	-38	-149	-257	-204	-148	-126	80N	
	40N	-229	-179	-101	0	134	256	278	233	98	-62	-175	-212	3	40N	
	Eq	38	78	142	203	263	305	299	278	250	186	131	94	189	Eq	
	Eq	211	193	239	314	414	490	567	628	573	455	338	269	391	Eq	
	40S	513	522	447	357	228	162	145	138	189	253	339	425	310	40S	
	80S	266	278	226	204	163	123	90	90	137	192	276	274	193	80S	
	80S	33	13	-85	-157	-205	-222	-247	-235	-197	-131	-53	29	-121	80S	
	80S	-189	-210	-231	-215	-161	-135	-112	-112	-120	-132	-163	-167	-162	80S	
SFC	80N	166	162	65	-12	-159	-333	-275	-187	58	303	272	197	22	80N	
	40N	262	73	-228	-510	-718	-801	-702	-535	-304	-35	193	292	-251	40N	
	Eq	-103	-242	-311	-453	-524	-556	-540	-473	-400	-278	-171	-115	-347	Eq	
	Eq	-324	-312	-357	-440	-579	-680	-803	-914	-778	-590	-458	-349	-549	Eq	
	40S	-739	-756	-599	-454	-277	-197	-192	-207	-271	-394	-504	-584	-431	40S	
	80S	-553	-531	-370	-277	-173	-94	-105	-179	-361	-498	-627	-602	-364	80S	
	80S	-1107	-833	-379	18	279	387	341	133	-273	-709	-1103	-1197	-370	80S	
	80S	-335	-220	82	219	212	180	145	128	83	11	-127	-268	9	80S	

Table A.2: Monthly mean heat flux from mixed-phase clouds, binned in 20° latitude bands from 80°S to 80°N. Heat flux, reported in units of Terawatts (TW or 10¹² W), is computed at the top of atmosphere (TOA), surface (SFC), and in atmosphere (ATM). A positive (negative) heat flux represents a net gain (loss) of energy at a given atmospheric level. All data are from R05 2B-FLXHR-LIDAR, 2007–2010.

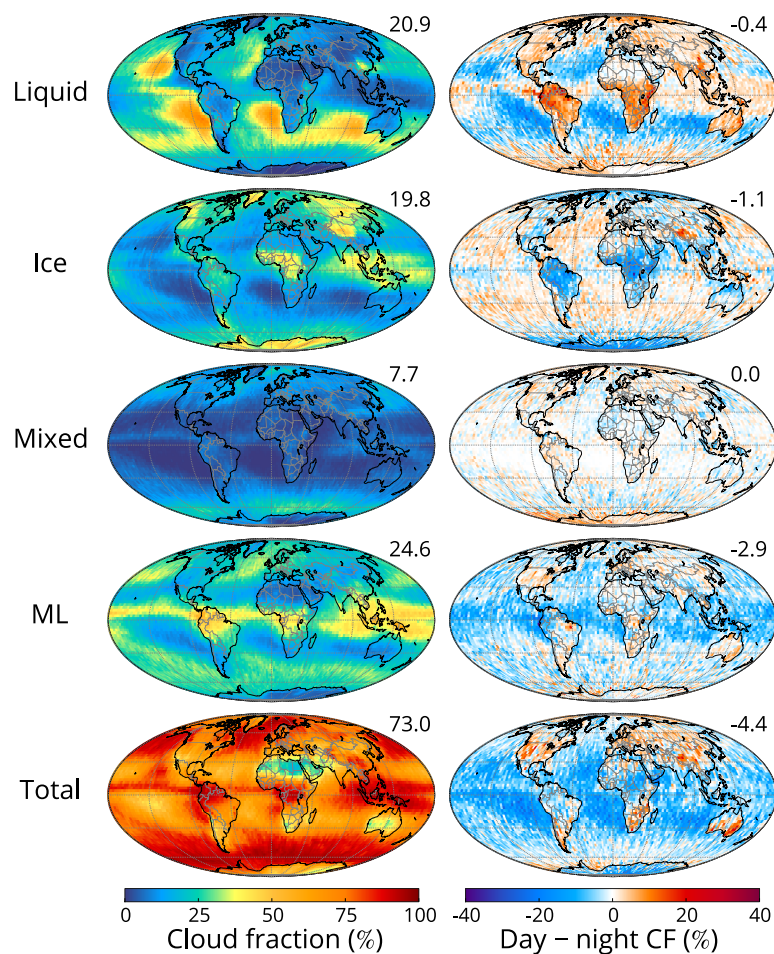


Figure A.1: (left column) CloudSat/CALIPSO cloud occurrence according to water phase and (right column) the daytime minus nighttime difference in cloud occurrence. Cloud phase is determined based on the 2B-CLDCLASS-LIDAR cloud phase classification. Mixed-phase clouds are defined as single-layer clouds containing multiple phases, whereas multilayered (ML) clouds are assigned if CALIPSO detects cloud layers of more than one phase within a given profile. All data are $2.5^\circ \times 2.5^\circ$ gridded annual averages from 2007 to 2010.

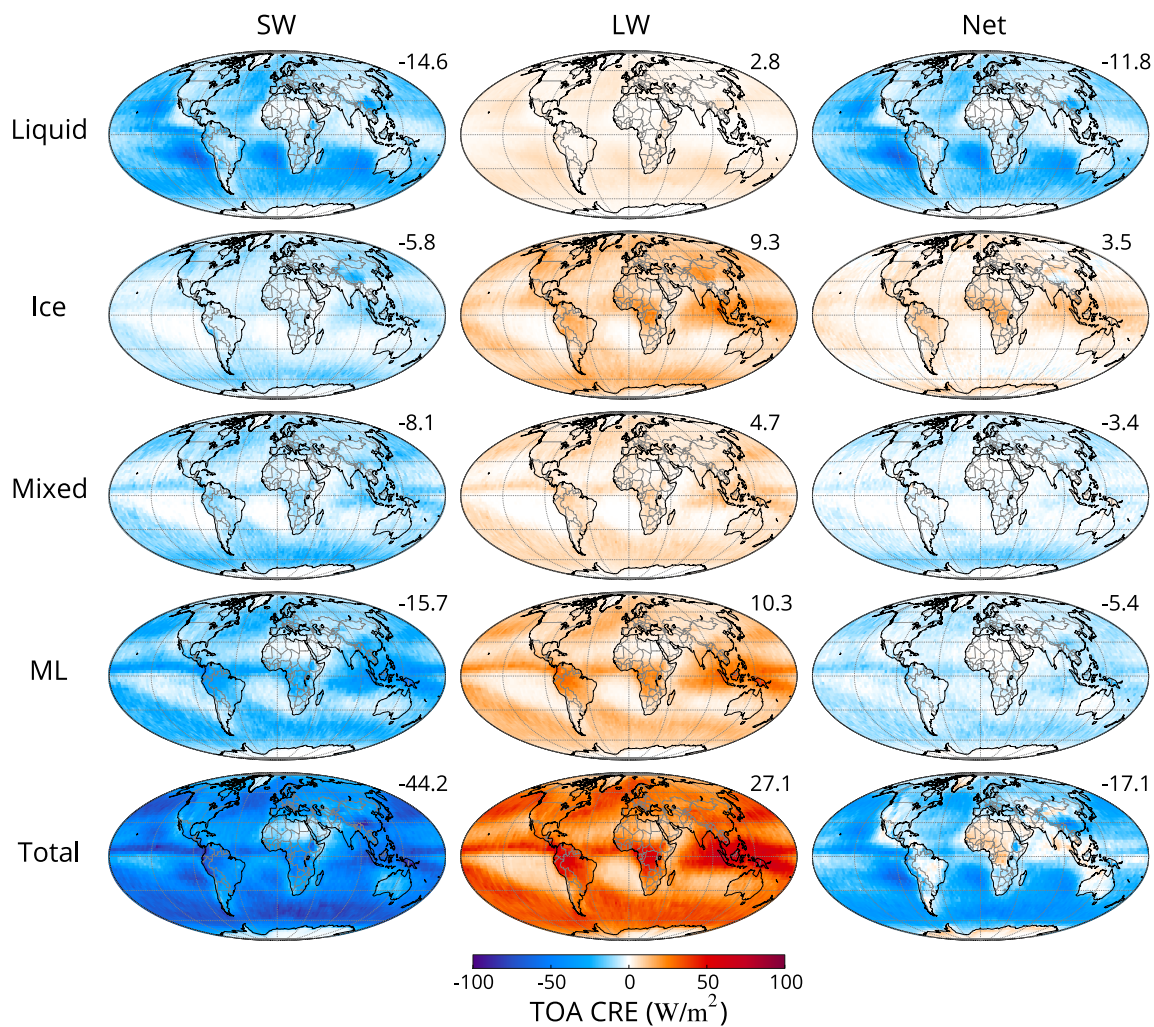


Figure A.2: Annual average shortwave, longwave, and net cloud radiative effects at the top of atmosphere (TOA). Radiative effects are separated by water phase (liquid, ice, mixed, and multilayered) using R05 2B-FLXHR-LIDAR, 2007–2010.

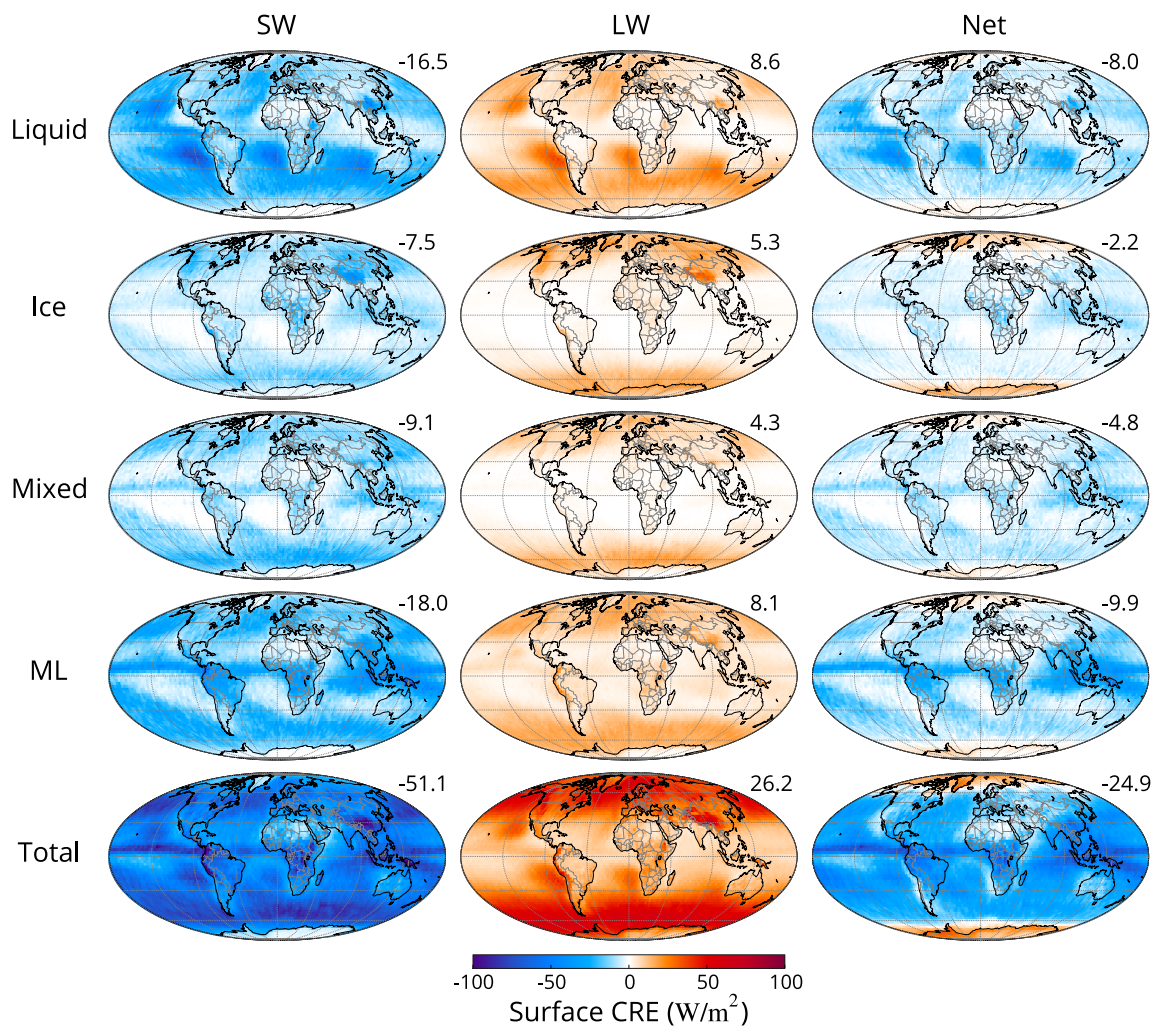


Figure A.3: Same as Figure 5 but for CRE at the surface.

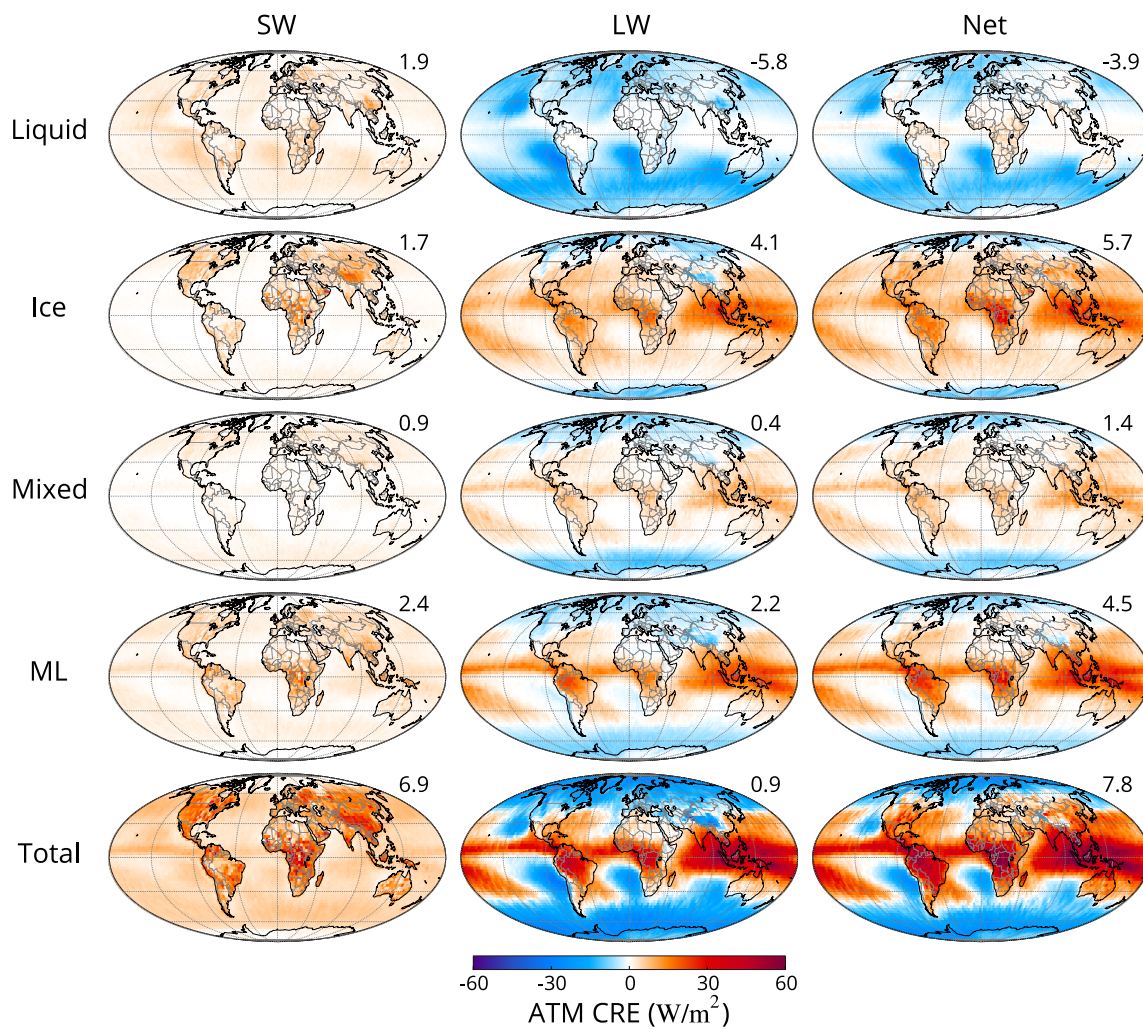


Figure A.4: Same as Figure 5 but for cloud radiative effects in the atmosphere (ATM), defined as the difference between TOA CRE and surface CRE.

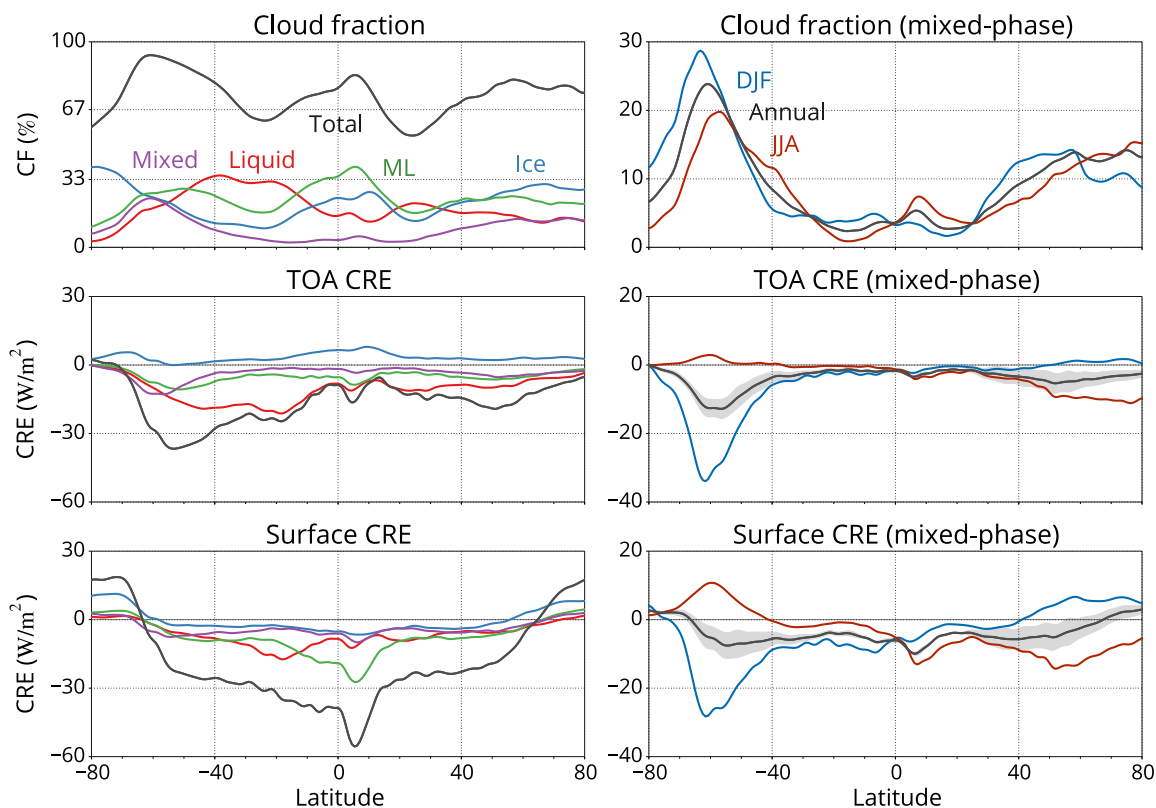


Figure A.5: (top row) Zonal mean cloud fraction, (middle row) top of atmosphere cloud radiative effect, and (bottom row) surface cloud radiative effect using CloudSat/CALIPSO observations from 2007 to 2010. The left column distinguishes clouds by water phase (liquid, ice, mixed phase, and multilayered), while the right column separates mixed-phase clouds by season: December–February (DJF) and June–August (JJA). Mixed-phase clouds are defined as single-layer clouds containing multiple phases, whereas multilayered clouds are assigned to scenes with multiple discrete cloud layers of different phases. Gray shading indicates the estimated range of uncertainty in mixed-phase cloud radiative effects, computed in 2B-FLXHR-LIDAR as the flux perturbation under a scenario in which all supercooled liquid is converted to ice.

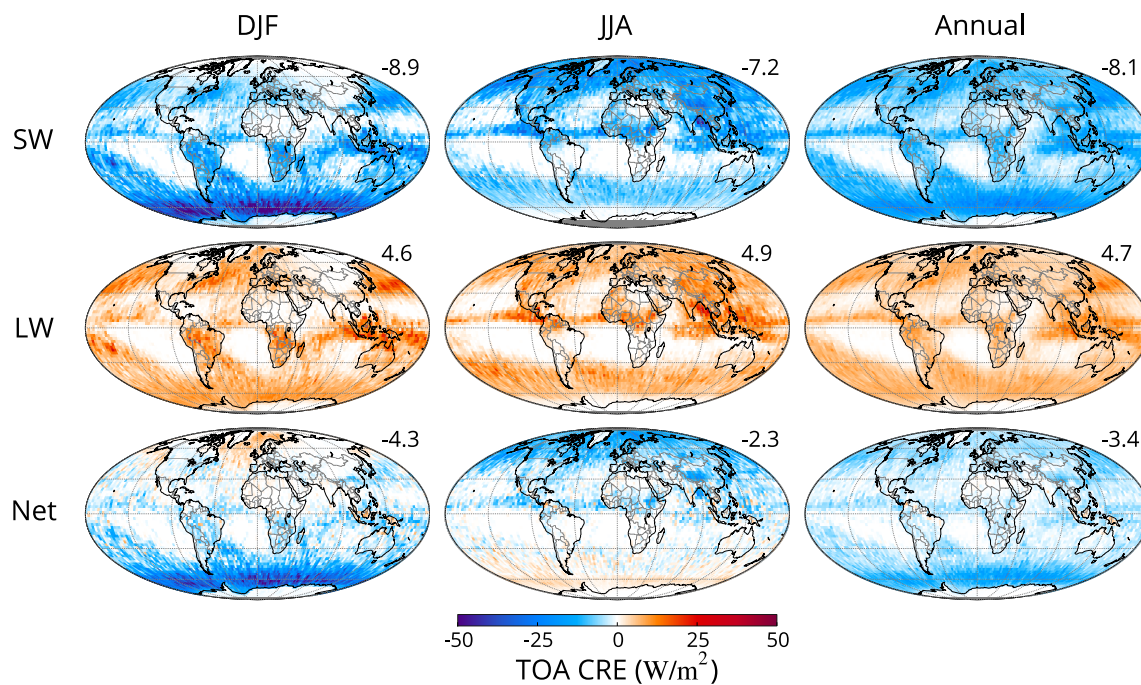


Figure A.6: Seasonal and annual mean radiative effect of mixed-phase clouds at the TOA. Seasons are defined as December–February (DJF) and June–August (JJA). All data are from R05 2B-FLXHR-LIDAR, 2007–2010.

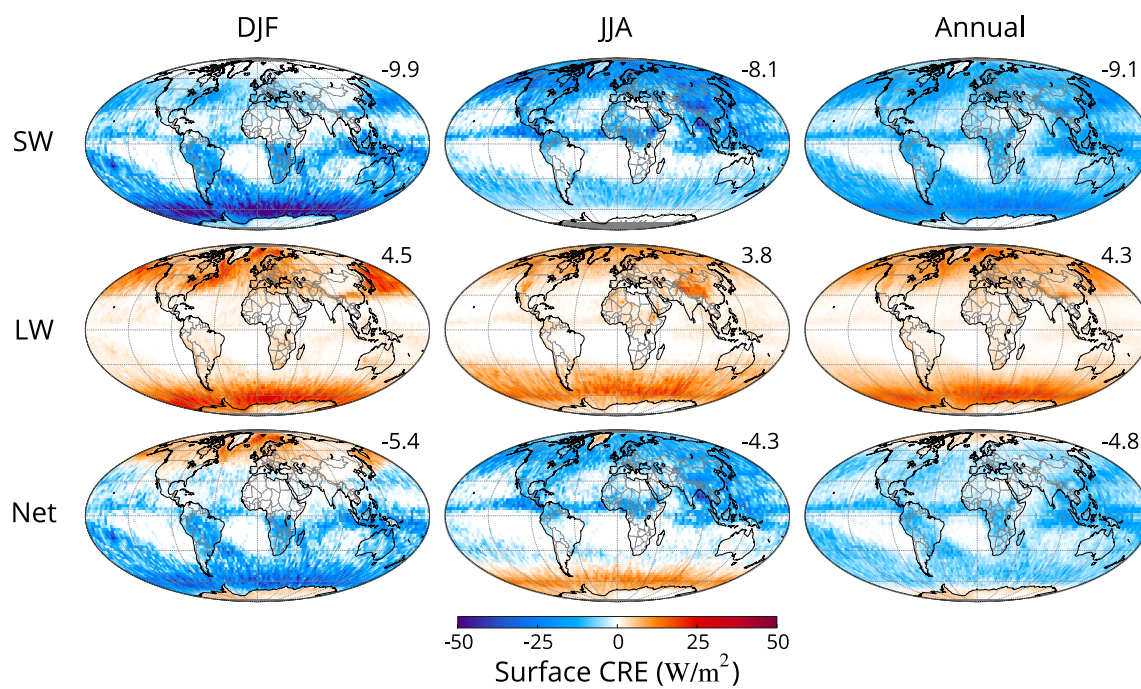


Figure A.7: Same as Figure 9 but for mixed-phase CRE at the surface.

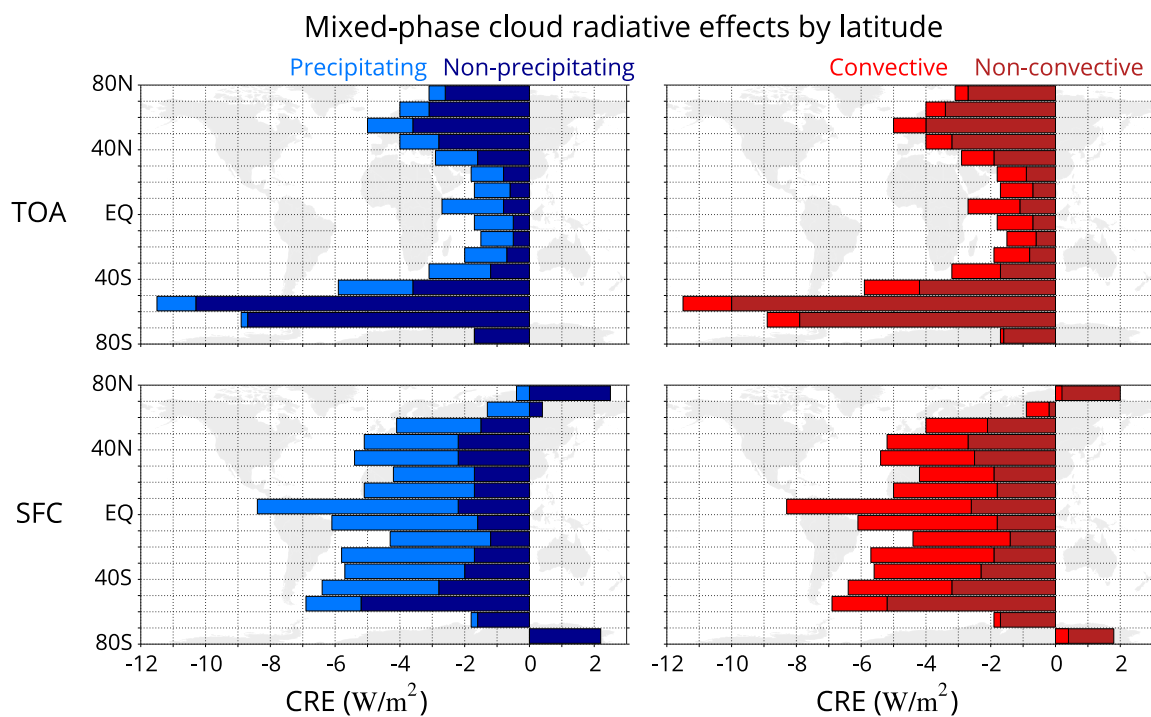


Figure A.8: Annual mean net radiative effects from mixed-phase clouds binned into 10° -latitude bands. Cloud radiative effects at the TOA and surface are stratified by (left column) convective/non-convective clouds and (right column) precipitating/non-precipitating clouds. All data are from R05 2B-FLXHR-LIDAR, 2007–2010.

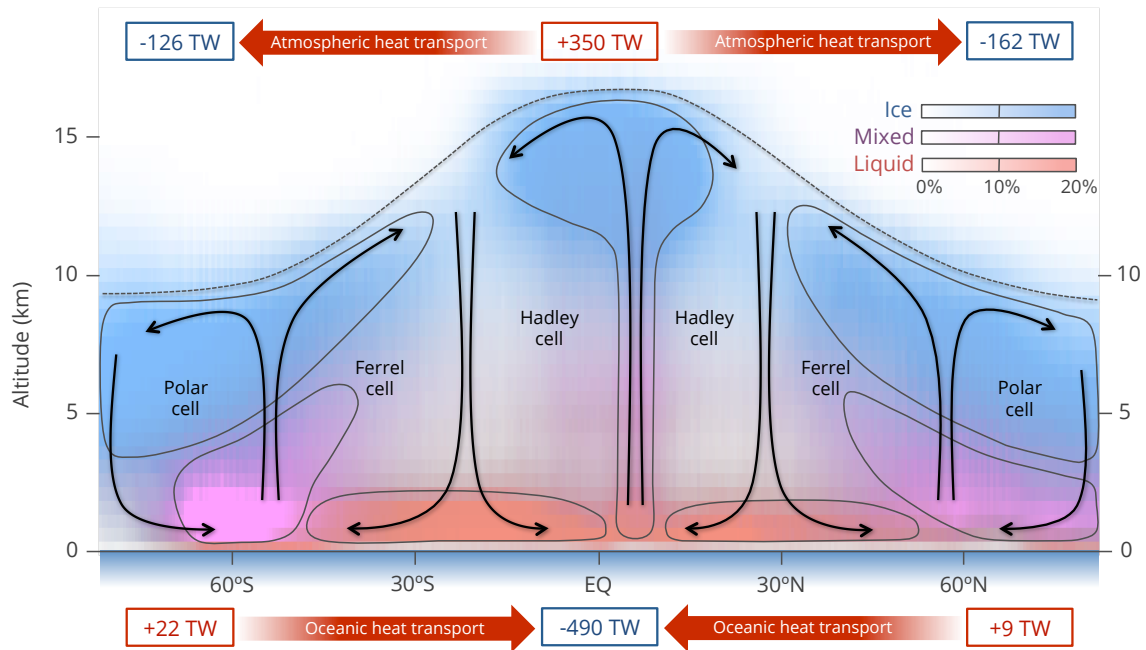


Figure A.9: Conceptual illustration of the location of mixed-phase clouds and their influence on global heat transport. Boxed values indicate the contribution of annual heat flux from mixed-phase clouds within the atmosphere and at the surface. Color shading indicates the observed cloud occurrence of liquid (red), ice (blue), and mixed-phase (purple) clouds using cloud phase classification data from 2B-CLDCLASS-LIDAR, 2007–2010. For illustrative purposes, black arrows indicate the general structure of large-scale atmospheric circulations and gray outlines indicate the boundaries of idealized cloud regimes.

Bibliography

- Albrecht, B. A., 1989: Aerosols, Cloud Microphysics, and Fractional Cloudiness. *Science*, **245** (4923), 1227–1230, doi:10.1126/science.245.4923.1227, URL <http://www.sciencemag.org/cgi/content/abstract/245/4923/1227>.
- Allan, R. P. (2011), Combining satellite data and models to estimate cloud radiative effect at the surface and in the atmosphere, *Meteorol. Appl.*, 18(3), 324–333, doi:10.1002/met.285.
- Anderson, T. L., and Coauthors, 2005: An A-Train strategy for quantifying direct climate forcing by anthropogenic aerosols. *Bull. Amer. Meteorol. Soc.*, 86, 1795–1809, doi:10.1175/BAMS-86-12-1795.
- Atkinson, J. D., B. J. Murray, M. T. Woodhouse, T. F. Whale, K. J. Baustian, K. S. Carslaw, S. Dobbie, D. O’Sullivan, and T. L. Malkin (2013), The importance of feldspar for ice nucleation by mineral dust in mixed-phase clouds, *Nature*, 498(7454), 355–358, doi:10.1038/nature12278
- Balkanski, Y. and M. Schulz, 2007: Reevaluation of mineral aerosol radiative forcings suggests a better agreement with satellite and AERONET data. *Atmospheric Chemistry and Physics*, (2001), 81–95, URL <http://www.atmos-chem-phys.net/7/81/2007/acp-7-81-2007.pdf>.
- Bellouin, N., O. Boucher, J. Haywood, and M. S. Reddy, 2005: Global estimate of aerosol direct radiative forcing from satellite measurements. *Nature*, **438** (7071), 1138–1141, URL <http://www.ncbi.nlm.nih.gov/pubmed/16372005>.
- Bergamo, A., A. M. Tafuro, S. Kinne, F. De Tomasi, and M. R. Perrone, 2008: Monthly-averaged anthropogenic aerosol direct radiative forcing over the Mediterranean from AERONET derived aerosol properties. *Atmos. Chem. Phys. Discuss.* 8, 12 769–12 822, doi:10.5194/acpd-8-12769-2008.
- Blot, R., and Coauthors, 2013: Ultrafine sea spray aerosol over the southeastern Pacific: Open-ocean contributions to marine boundary layer CCN. *Atmos. Chem. Phys.*, 13, 7263–7278, doi:10.5194/acp-13-7263-2013.
- Bony, S., R. Colman, and V. Kattsov (2006), How well do we understand and evaluate climate change feedback processes?, *J. Clim.*, 19, 3445–3482.

- Boucher, O. and D. Tanré, 2000: Estimation of the aerosol perturbation to the Earth's radiative budget over oceans using POLDER satellite aerosol retrievals. *Geophysical research letters*, **27** (8), 1103–1106, URL <http://www.agu.org/pubs/crossref/2000/1999GL010963.shtml>.
- CCSP, 2009: Atmospheric Aerosol Properties and Climate Impacts. Tech. Rep. January, NASA, 128 pp. URL <http://purl.access.gpo.gov/GPO/LPS110658>.
- Cesana, G., J. E. Kay, H. Chepfer, J. M. English, and G. De Boer (2012), Ubiquitous low-level liquid-containing Arctic clouds: New observations and climate model constraints from CALIPSO-GOCCP, *Geophys. Res. Lett.*, **39**, L20804, doi:10.1029/2012GL053385.
- Cesana, G., D. E. Waliser, X. Jiang, and J. L. F. Li (2015), Multimodel evaluation of cloud phase transition using satellite and reanalysis data, *J. Geophys. Res. Atmos.*, **120**, 7871–7892, doi:10.1002/2014JD022932.
- Chand, D., R. Wood, T. L. Anderson, S. K. Satheesh, and R. J. Charlson, 2009: Satellite-derived direct radiative effect of aerosols dependent on cloud cover. *Nat. Geosci.*, **2**, 181–184, doi:10.1038/ngeo437.
- Chand, D., et al., 2012: Aerosol optical depth increase in partly cloudy conditions. *Journal of Geophysical Research: Atmospheres*, **117** (D17), doi:10.1029/2012JD017894, URL <http://doi.wiley.com/10.1029/2012JD017894>.
- Charlson, R. J., S. E. Schwartz, J. M. Hales, R. D. Cess, J. A. Coakley, J. E. Hansen, and D. J. Hofmann, 1992: Climate forcing by anthropogenic aerosols. *Science*, **255** (5043), 423–430, URL <http://www.sciencemag.org/content/255/5043/423>.
- Chepfer, H., S. Bony, D. Winker, G. Cesana, J. L. Dufresne, P. Minnis, C. J. Stubenrauch, and S. Zeng, 2010: The GCM-oriented CALIPSO cloud product (CALIPSO-GOCCP). *J. Geophys. Res.*, **115**, D00H16, doi:10.1029/2009JD012251.
- Chepfer, H., D. Cesana, D. Winker, B. Getzewich, M. Vaughan, and Z. Liu (2013), Comparison of two different cloud climatologies derived from CALIOP-attenuated backscattered measurements (Level 1): The CALIPSO-ST and the CALIPSO-GOCCP, *J. Atmos. Oceanic Technol.*, **30**(4), 725–744, doi:10.1175/JTECH-D-12-00057.1.

- Chin, M., R. A. Kahn, and S. E. Schwartz, 2009: Atmospheric Aerosol Properties and Climate Impacts. DIANE Publishing, 115 pp.
- Chin, M., P. Ginoux, and S. Kinne, 2002: Tropospheric aerosol optical thickness from the GOCART model and comparisons with satellite and Sun photometer measurements. *Journal of the Atmospheric Sciences*, 461–483, URL [http://journals.ametsoc.org/doi/abs/10.1175/1520-0469\(2002\)059%3C0461:TAOTFT%3E2.0.CO%3B2](http://journals.ametsoc.org/doi/abs/10.1175/1520-0469(2002)059%3C0461:TAOTFT%3E2.0.CO%3B2).
- Chung, C. E., V. Ramanathan, D. Kim, and I. A. Podgorny, 2005: Global anthropogenic aerosol direct forcing derived from satellite and ground-based observations. *J. Geophys. Res.*, 110, D24207, doi:10.1029/2005JD006356.
- Christensen, M. W., G. L. Stephens, and M. D. Lebsock (2013), Exposing biases in retrieved low cloud properties from CloudSat: A guide for evaluating observations and climate data, *J. Geophys. Res. Atmos.*, 118, 12,120–12,131, doi:10.1002/2013JD020224.
- Christensen, M. W., A. Behrangi, T. L'Ecuyer, N. B. Wood, M. D. Lebsock, and G. L. Stephens (2016), Arctic observation and reanalysis integrated system: A new data product for validation and climate study, *Bull. Am. Meteorol. Soc.*, 97, 907–915, doi:10.1175/BAMS-D-14-00273.1
- de Graaf, M., L. G. Tilstra, P. Wang, and P. Stammes, 2012: Retrieval of the aerosol direct radiative effect over clouds from spaceborne spectrometry. *J. Geophys. Res. Atmos.*, 117, D07207, doi:10.1029/2011JD017160.
- Deng, M., G. G. Mace, Z. Wang, and R. Paul Lawson (2013), Evaluation of several A-Train ice cloud retrieval products with in situ measurements collected during the SPARTICUS campaign, *J. Appl. Meteorol. Climatol.*, 52(4), 1014–1030, doi:10.1175/JAMC-D-12-054.1.
- Di Biagio, C., A. di Sarra, and D. Meloni, 2010: Large atmospheric shortwave radiative forcing by Mediterranean aerosols derived from simultaneous ground-based and spaceborne observations and dependence on the aerosol type and single scattering albedo. *J. Geophys. Res.*, 115, D10209, doi:10.1029/2009JD012697.
- Diner, D. J., J. C. Beckert, G. W. Bothwell, and J. I. Rodriguez, 2002: Performance of the MISR instrument during its first 20 months in Earth orbit. 1449–1466 pp., doi: 10.1109/TGRS.2002.801584.

- Dubovik, O. and B. Holben, 2002: Variability of absorption and optical properties of key aerosol types observed in worldwide locations. *Journal of the Atmospheric Sciences*, **(ii)**, 590–608, URL [http://journals.ametsoc.org/doi/abs/10.1175/1520-0469\(2002\)059%3C0590:VOAOP%3E2.0.CO%3B2](http://journals.ametsoc.org/doi/abs/10.1175/1520-0469(2002)059%3C0590:VOAOP%3E2.0.CO%3B2).
- Eck, T. F., 2003: Variability of biomass burning aerosol optical characteristics in southern Africa during the SAFARI 2000 dry season campaign and a comparison of single scattering albedo estimates from radiometric measurements. *Journal of Geophysical Research*, **108 (D13)**, 8477, doi:10.1029/2002JD002321, URL <http://doi.wiley.com/10.1029/2002JD002321>.
- Flato, G., et al. (2013), Evaluation of climate models, in *Climate Change 2013: The Physical Science Basis. Contribution of Working Group I to the Fifth Assessment Report of the Intergovernmental Panel on Climate Change*, edited by T. F. Stocker et al., pp. 741–866, Cambridge Univ. Press, Cambridge, U. K., and New York, doi:10.1017/CBO9781107415324.
- Forbes, R. M., and M. Ahlgrim (2014), On the representation of high-latitude boundary layer mixed-phase cloud in the ECMWF global model, *Mon. Weather Rev.*, **142(9)**, 3425–3446, doi:10.1175/MWR-D-13-00325.1.
- Forster, P., V. Ramaswamy, and P. Artaxo, 2007: Changes in Atmospheric Constituents and in Radiative Forcing. *Climate Change 2007 The Physical Science Basis Contribution of Working Group I to the Fourth Assessment Report of the Intergovernmental Panel on Climate Change*, **AR4**, 129–234, URL http://www.ipcc.ch/publications_and_data/publications_ipcc_fourth_assessment_report_wg1_report_the_physical_science_basis.htm.
- Fu, Q. and K. N. Liou, 1992: On the correlated k-distribution method for radiative transfer in nonhomogeneous atmospheres. *Journal of the Atmospheric Sciences*, **49 (22)**, 2139–2156, doi:10.1175/1520-0469(1992)049,2139:OTCDMF.2.0.CO;2.
- Fu, Q., and K. N. Liou (1993), Parameterization of the radiative properties of cirrus clouds, *J. Atmos. Sci.*, **50**, 2008–2025, doi:10.1175/1520-0469(1993)0502.0.CO;2.
- Gettelman, A., H. Morrison, and S. J. Ghan (2007), A new two-moment bulk stratiform cloud microphysics scheme in the NCAR Community Atmosphere Model (CAM3). Part II: Single-column and global results, *J. Clim.*, **21**, 3660–3679, doi:10.1175/2008JCLI2116.

- Hansen, J., M. Sato, and R. Ruedy, 1997: Radiative forcing and climate response. *J. Geophys. Res.*, 102 (D6), 6831–6864, doi:10.1029/96JD03436.
- Haynes, J. M., T. S. L'Ecuyer, G. L. Stephens, S. D. Miller, C. Mitrescu, N. B. Wood, and S. Tanelli (2009), Rainfall retrieval over the ocean with spaceborne W-band radar, *J. Geophys. Res.*, 114, D00A22, doi:10.1029/2008JD009973.
- Haywood, J. M., 2003: The mean physical and optical properties of regional haze dominated by biomass burning aerosol measured from the C-130 aircraft during SAFARI 2000. *Journal of Geophysical Research*, **108 (D13)**, 8473, doi:10.1029/2002JD002226, URL <http://doi.wiley.com/10.1029/2002JD002226>.
- Henderson, D. S., and T. S. L'Ecuyer (2011), Level 2B fluxes and heating rates and 2B fluxes and heating rates w/ lidar process description and interface control document, Tech. Rep. D, CloudSat Algorithm Process Description Documents.
- Henderson, D. S., T. L'Ecuyer, G. Stephens, P. Partain, and M. Sekiguchi, 2013: A Multisensor Perspective on the Radiative Impacts of Clouds and Aerosols. *Journal of Applied Meteorology and Climatology*, **52 (4)**, 853–871, doi:10.1175/JAMC-D-12-025.1, URL <http://journals.ametsoc.org/doi/abs/10.1175/JAMC-D-12-025.1>.
- Hogan, R. J., P. N. Francis, H. Flentje, A. J. Illingworth, M. Quante, and J. Pelon (2003), Characteristics of mixed phase clouds. Part I: Lidar, radar and aircraft observations from CLARE '98, *Q. J. R. Meteorol. Soc.*, 129, 2089–2116, doi:10.1256/qj.01.208.
- Hogan, R. J., M. D. Behera, E. J. O'Connor, and A. J. Illingworth (2004), Estimate of the global distribution of stratiform supercooled liquid water clouds using the LITE lidar, *J. Geophys. Res.*, 31, L05106, doi:10.1029/2003GL018977.
- Hu, Y., S. Rodier, K. M. Xu, W. Sun, J. Huang, B. Lin, P. Zhai, and D. Josset (2010), Occurrence, liquid water content, and fraction of supercooled water clouds from combined CALIOP/IIR/MODIS measurements, *J. Geophys. Res.*, 115, D00H34, doi:10.1029/2009JD012384.

- Hurrell, J. W., and Coauthors, 2013: The Community Earth System Model: A framework for collaborative research. *Bull. Amer. Meteor. Soc.*, 94, 1339–1360, doi:10.1175/BAMS-D-12-00121.1.
- Jaeglé, L., P. K. Quinn, T. S. Bates, B. Alexander, and J.-T. Lin, 2011: Global distribution of sea salt aerosols: New constraints from in situ and remote sensing observations. *Atmos. Chem. Phys.*, 11, 3137–3157, doi:10.5194/acp-11-3137-2011.
- Jiang, J. H., and Coauthors, 2012: Evaluation of cloud and water vapor simulations in CMIP5 climate models using NASA ATrain satellite observations. *J. Geophys. Res.*, 117, D14105, doi:10.1029/2011JD017237.
- Kacenelenbogen, M., and Coauthors, 2014: An evaluation of CALIOP/CALIPSO's aerosol-above-cloud detection and retrieval capability over North America. *J. Geophys. Res. Atmos.*, 119, 230–244, doi:10.1002/2013JD020178.
- Kahn, R. A., 2005: Multiangle Imaging Spectroradiometer (MISR) global aerosol optical depth validation based on 2 years of coincident Aerosol Robotic Network (AERONET) observations. *Journal of Geophysical Research*, **110** (D10), 1–16, doi:10.1029/2004JD004706, URL <http://www.agu.org/pubs/crossref/2005/2004JD004706.shtml>.
- Kato, S., S. Sun-Mack, W. F. Miller, F. G. Rose, Y. Chen, P. Minnis, and B. A. Wielicki (2010), Relationships among cloud occurrence frequency, overlap, and effective thickness derived from CALIPSO and CloudSat merged cloud vertical profiles, *J. Geophys. Res.*, 115, D00H28, doi:10.1029/2009JD012277.
- Kaufman, Y. J., O. Boucher, D. Tanré, M. Chin, L. A. Remer, and T. Takemura, 2005: Aerosol anthropogenic component estimated from satellite data. *Geophys. Res. Lett.*, 32, L17804, doi:10.1029/2005GL023125.
- Kay, J. E., et al., 2012: Exposing Global Cloud Biases in the Community Atmosphere Model (CAM) Using Satellite Observations and Their Corresponding Instrument Simulators. *Journal of Climate*, **25** (15), 5190–5207, doi:10.1175/JCLI-D-11-00469.1, URL <http://journals.ametsoc.org/doi/abs/10.1175/JCLI-D-11-00469.1>.

- Kay, J. E., L. Bourdages, N. B. Miller, A. Morrison, V. Yettella, H. Chepfer, and B. Eaton (2016), Evaluating and improving cloud phase in the Community Atmosphere Model version 5 using spaceborne lidar observations, *J. Geophys. Res. Atmos.*, 121, 4162–4176, doi:10.1002/2015JD024699.
- Kiehl, J. T., J. J. Hack, and B. P. Briegleb (1994), The simulated Earth radiation budget of the National Center for Atmospheric Research community climate model CCM2 and comparisons with the Earth Radiation Budget Experiment (ERBE), *J. Geophys. Res.*, 99(D10), 20,815–20,827, doi:10.1029/94JD00941.
- Kittaka, C., D. M. Winker, M. a. Vaughan, a. Omar, and L. a. Remer, 2011: Intercomparison of column aerosol optical depths from CALIPSO and MODIS-Aqua. *Atmospheric Measurement Techniques*, 4 (2), 131–141, doi:10.5194/amt-4-131-2011, URL <http://www.atmos-meas-tech.net/4/131/2011/>.
- Koch, D., 2005: Distant origins of Arctic black carbon: A Goddard Institute for Space Studies Model-E experiment. *Journal of Geophysical Research*, 110 (D4), D04 204, doi:10.1029/2004JD005296, URL <http://doi.wiley.com/10.1029/2004JD005296>.
- Komurcu, M., T. Storelvmo, I. Tan, U. Lohmann, Y. Yun, J. E. Penner, Y. Wang, X. Liu, and T. Takemura (2014), Intercomparison of the cloud water phase among global climate models, *J. Geophys. Res. Atmos.*, 119, 3372–3400, doi:10.1002/2013JD021119.
- Lamarque, J.-F., and Coauthors, 2013: The Atmospheric Chemistry and Climate Model Intercomparison Project (ACCMIP): Overview and description of models, simulations and climate diagnostics. *Geosci. Model Dev.*, 6, 179–206, doi:10.5194/gmd-6-179-2013.
- L'Ecuyer, T. S., N. B. Wood, T. Haladay, G. L. Stephens, and P. W. Stackhouse, 2008: Impact of clouds on atmospheric heating based on the R04 CloudSat fluxes and heating rates data set. *Journal of Geophysical Research*, 113, D00A15, doi:10.1029/2008JD009951, URL <http://doi.wiley.com/10.1029/2008JD009951>.
- L'Ecuyer, T. S., and J. Jiang, 2010: Touring the atmosphere aboard the A-Train. *Phys. Today*, 63, 36, doi:10.1063/1.3463626.

- L'Ecuyer, T. S., et al. (2015), The observed state of the energy budget in the early twenty-first century, *J. Clim.*, 28(21), 8319–8346, doi:10.1175/JCLI-D-14-00556.1.
- Liu, X., and Coauthors, 2012: Toward a minimal representation of aerosols in climate models: Description and evaluation in the Community Atmosphere Model CAM5. *Geosci. Model Dev.*, 5, 709–739, doi:10.5194/gmd-5-709-2012.
- Loeb, N. and N. Manalo-Smith, 2005: Top-of-atmosphere direct radiative effect of aerosols over global oceans from merged CERES and MODIS observations. *Journal of Climate*, 3506–3526, URL <http://journals.ametsoc.org/doi/pdf/10.1175/JCLI3504.1>.
- Loeb, N. G., N. Manalo-Smith, K. Loukachine, S. Kato, and B. A. Wielicki, 2002: Advances in top-of-atmosphere radiative flux estimation from the Clouds and the Earth's Radiant Energy System (CERES) satellite instrument. doi:10.1109/IGARSS.2002.1025753.
- Loeb, N. G., J. M. Lyman, G. C. Johnson, R. P. Allan, D. R. Doelling, T. Wong, B. J. Soden, and G. L. Stephens (2012), Observed changes in top-of-the-atmosphere radiation and upper-ocean heating consistent within uncertainty, *Nat. Geosci.*, 5(2), 110–113, doi:10.1038/ngeo1375.
- Lü, Q., J. Li, T. Wang, and J. Huang (2015), Cloud radiative forcing induced by layered clouds and associated impact on the atmospheric heating rate, *J. Meteorol. Res.*, 29(5), 779–792, doi:10.1007/s13351-015-5078-7.
- Mahowald, N. M., D. R. Muhs, S. Levis, P. J. Rasch, M. Yoshioka, C. S. Zender, and C. Luo, 2006: Change in atmospheric mineral aerosols in response to climate: Last glacial period, preindustrial, modern, and doubled carbon dioxide climates. *Journal of Geophysical Research*, **111** (D10), D10202, doi:10.1029/2005JD006653, URL <http://doi.wiley.com/10.1029/2005JD006653>.
- Matus, A., T. L'Ecuyer, J. Kay, C. Hannay, and J. Lamarque, 2015: The role of clouds in modulating global aerosol direct radiative effects in spaceborne active observations and the Community Earth System Model, *J. Climate*, **28**, 2986–3003, <https://doi.org/10.1175/JCLI-D-14-00426.1>
- Matus, A., and T. L'Ecuyer, 2017: The role of cloud phase in Earth's radiation budget. *J. Geophys. Res. Atmos.*, **122**, 2559–2578, <https://doi.org/10.1002/2016JD025951>.

- Mccoy, D. T., D. L. Hartmann, M. D. Zelinka, P. Ceppi, and D. P. Grosvenor (2015), Mixed-phase cloud physics and Southern Ocean cloud feedback in climate models, *J. Geophys. Res. Atmos.*, 120, 9539–9554, doi:10.1002/2015JD023603.
- McCoy, D. T., S. M. Burrows, R. Wood, D. P. Grosvenor, S. M. Elliott, P.-L. Ma, P. J. Rasch, and D. L. Hartmann (2015), Natural aerosols explain seasonal and spatial patterns of Southern Ocean cloud albedo, *Sci. Adv.*, 1(6), e1500157, doi:10.1126/sciadv.1500157.
- McIlhattan, E.A., T.S. L'Ecuyer, and N.B. Miller, 2017: Observational Evidence Linking Arctic Supercooled Liquid Cloud Biases in CESM to Snowfall Processes. *J. Climate*, 30, 4477–4495, <https://doi.org/10.1175/JCLI-D-16-0666.1>
- Menon, A., A. Levermann, and J. Schewe, 2013: Enhanced future variability during India's rainy season. *Geophysical Research Letters*, n/a–n/a, doi:10.1002/grl.50583, URL <http://doi.wiley.com/10.1002/grl.50583>.
- Mikami, M., et al., 2006: Aeolian dust experiment on climate impact: An overview of JapanChina joint project ADEC. *Global and Planetary Change*, **52 (1-4)**, 142–172, doi:10.1016/j.gloplacha.2006.03.001, URL <http://linkinghub.elsevier.com/retrieve/pii/S092181810600035X>.
- Miller, S. D., Y.-J. Noh, and A. K. Heidinger (2014), Liquid-top mixed-phase cloud detection from shortwave-infrared satellite radiometer observations: A physical basis, *J. Geophys. Res. Atmos.*, 119, 8245–8267, doi:10.1002/2013JD021262.
- Moody, E. G., M. D. King, S. Member, S. Platnick, and C. B. Schaaf, 2005: Spatially Complete Global Spectral Surface Albedos : Value-Added Datasets Derived From Terra MODIS Land Products. **43 (1)**, 144–158.
- Morrison, H., et al. (2011), Intercomparison of cloud model simulations of Arctic mixed-phase boundary layer clouds observed during SHEBA/FIRE-ACE, *J. Adv. Model. Earth Syst.*, 3, M06003, doi:10.1029/2011MS000066.
- Murray, E. J., B. J. Murray, and V. Sivakumar (2013), Ice nucleation by particles immersed in supercooled cloud droplets, *Chem. Soc. Rev.*, 42(24), 9571–9572.

- Myhre, G., 2009: Consistency between satellite-derived and modeled estimates of the direct aerosol effect. *Science*, 325, 187– 190, doi:10.1126/science.1174461.
- Myhre, G., Y. Govaerts, J. M. Haywood, T. K. Berntsen, and A. Lattanzio, 2005: Radiative effect of surface albedo change from biomass burning. *Geophys. Res. Lett.*, 32, L20812, doi:10.1029/2005GL022897.
- Myhre, G., and Coauthors, 2007: Comparison of the radiative properties and direct radiative effect of aerosols from a global aerosol model and remote sensing data over ocean. *Tellus*, 59B, 115– 129, doi:10.1111/j.1600-0889.2006.00226.x.
- Neale, R., and C. Chen, 2010: Description of the NCAR Community Atmosphere Model (CAM 5.0). NCAR Tech. Note NCAR/TN-4861STR, 274 pp.
- NRC, 2005: *Radiative Forcing of Climate Change: Expanding the Concept and Addressing Uncertainties*. National Academies Press, URL <http://books.google.com/books?id=nWKIVLa5N0sC>.
- Ocko, I. B., V. Ramaswamy, P. Ginoux, Y. Ming, and L. W. Horowitz, 2012: Sensitivity of scattering and absorbing aerosol direct radiative forcing to physical climate factors. *Journal of Geophysical Research*, **117** (D20), D20 203, doi:10.1029/2012JD018019, URL <http://www.agu.org/pubs/crossref/2012/2012JD018019.shtml>.
- Omar, A. H., and Coauthors, 2009: The CALIPSO automated aerosol classification and lidar ratio selection algorithm. *J. Atmos. Oceanic Technol.*, 26, 1994–2014, doi:10.1175/2009JTECHA1231.1.
- Omar, A. H., and Coauthors, 2013: CALIOP and AERONET aerosol optical depth comparisons: One size fits none. *J. Geophys. Res. Atmos.*, 118, 4748–4766, doi:10.1002/jgrd.50330.
- Patadia, F., P. Gupta, and S. A. Christopher, 2008: First observational estimates of global clear sky shortwave aerosol direct radiative effect over land. *Geophys. Res. Lett.*, 35, L04810, doi:10.1029/2007GL032314.
- Penner, J. E., 2003: Soot and smoke aerosol may not warm climate. *J. Geophys. Res.*, 108, 4657, doi:10.1029/2003JD003409.

- Prezzi, A. J., J. Y. Harrington, M. Tjernstöm, P. J. DeMott, A. Avramov, C. N. Long, S. M. Kreidenweis, P. Q. Olsson, and J. Verlinde (2007), Can ice-nucleating aerosols affect arctic seasonal climate?, *Bull. Am. Meteorol. Soc.*, 88(4), 541–550, doi:10.1175/BAMS-88-4-541.
- Pruppacher, H. R., J. D. Klett, and P. K. Wang (1998), Microphysics of clouds and precipitation, *Aerosol Sci. Technol.*, 28(4), 381–382.
- Quijano, A. L., I. N. Sokolik, and O. B. Toon, 2000: Radiative heating rates and direct radiative forcing by mineral dust in cloudy atmospheric conditions. *J. Geophys. Res.*, 105, 12 207– 12 219, doi:10.1029/2000JD900047.
- Ramanathan, V., P. J. Crutzen, J. T. Kiehl, and D. Rosenfeld, 2001: Aerosols, climate, and the hydrological cycle. *Science*, **294 (5549)**, 2119–24, doi:10.1126/science.1064034, URL <http://www.ncbi.nlm.nih.gov/pubmed/11739947>.
- Randall, D. A., et al. (2007), Climate models and their evaluation, in *Climate Change 2007: The Physical Science Basis. Contribution of Working Group I to the Fourth Assessment Report of the IPCC (FAR)*, edited by S. Solomon et al., pp. 589–662, Cambridge Univ. Press, Cambridge, U. K., and New York.
- Rauber, R. M., and A. Tokay (1991), An explanation for the existence of supercooled water at the top of cold clouds, *J. Atmos. Sci.*, 48, 1005–1023, doi:10.1175/1520-0469(1991)048<1005:CO;2>
- Reddy, M. S., 2005: Estimates of global multicomponent aerosol optical depth and direct radiative perturbation in the Laboratoire de Mé té orologie Dynamique general circulation model. *Journal of Geophysical Research*, **110 (D10)**, D10S16, doi:10.1029/ 2004JD004757, URL <http://doi.wiley.com/10.1029/2004JD004757>.
- Redemann, J., M. A. Vaughan, Q. Zhang, Y. Shinzuka, P. B. Russell, J. M. Livingston, M. Kacenelenbogen, and L. A. Remer, 2012: The comparison of MODIS-Aqua (C5) and CALIOP (V2 & V3) aerosol optical depth. *Atmos. Chem. Phys.*, 12, 3025–3043, doi:10.5194/acp-12-3025-2012.
- Remer, L. A., and Coauthors, 2005: The MODIS aerosol algorithm, products, and validation. *J. Atmos. Sci.*, 62, 947–973, doi:10.1175/JAS3385.1.

- Remer, L. A. and Y. J. Kaufman, 2006: Aerosol direct radiative effect at the top of the atmosphere over cloud free ocean derived from four years of MODIS data. *Atmospheric Chemistry and Physics*, **6** (1), 237–253, doi:10.5194/acp-6-237-2006, URL <http://www.atmos-chem-phys.net/6/237/2006/>.
- Remer, L. A., et al., 2005: The MODIS Aerosol Algorithm, Products, and Validation. *Journal of the Atmospheric Sciences*, **62** (4), 947–973, doi:10.1175/JAS3385.1, URL <http://www.journals.ametsoc.org/doi/abs/10.1175/JAS3385.1>.
- Ritter, B. and J.-F. Geleyn, 1992: A Comprehensive Radiation Scheme for Numerical Weather Prediction Models with Potential Applications in Climate Simulations. *Monthly Weather Review*, **120** (2), 303–325, doi: 10.1175/1520-0493(1992)120<0303:ACRSFN>2.0.CO;2, URL <http://cat.inist.fr/?aModele=afficheN&cpsidt=5205974>.
- Sakaeda, N., R. Wood, and P. J. Rasch, 2011: Direct and semidirect aerosol effects of southern African biomass burning aerosol. *J. Geophys. Res.*, 116, D12205, doi:10.1029/2010JD015540.
- Sassen, K., and Z. Wang (2012), The clouds of the middle troposphere: Composition, radiative impact, and global distribution, *Surv. Geophys.*, 33(3–4), 677–691, doi:10.1007/s10712-011-9163-x.
- Satheesh, S., and K. Krishna Moorthy, 2005: Radiative effects of natural aerosols: A review. *Atmos. Environ.*, 39, 2089–2110, doi:10.1016/j.atmosenv.2004.12.029.
- Scholes, M., and M. O. Andreae (2000), Biogenic and pyrogenic emissions from Africa and their impact on the global atmosphere, *Ambio.*, 29, 23–29.
- Schulz, M., et al., 2006: Radiative forcing by aerosols as derived from the AeroCom present-day and pre-industrial simulations. *Atmospheric Chemistry and Physics*, **6** (12), 5225–5246, doi:10.5194/acp-6-5225-2006, URL <http://www.atmos-chem-phys.net/6/5225/2006/>.
- Schuster, G. L., M. Vaughan, D. MacDonnell, W. Su, D. Winker, O. Dubovik, T. Lapyonok, and C. Trepte, 2012: Comparison of CALIPSO aerosol optical depth retrievals to AERONET measurements, and a climatology for the lidar ratio of dust. *Atmos. Chem. Phys.*, 12, 7431–7452, doi:10.5194/acp-12-7431-2012.

- Sheuyange, A., G. Oba, and R. B. Weladji, 2005: Effects of anthropogenic fire history on savanna vegetation in northeastern Namibia. *J. Environ. Manage.*, **75**, 189–198, doi:10.1016/j.jenvman.2004.11.004.
- Shindell, D. T., et al., 2013: Radiative forcing in the ACCMIP historical and future climate simulations. *Atmospheric Chemistry and Physics*, **13** (6), 2939–2974, doi:10.5194/acp-13-2939-2013, URL <http://www.atmos-chem-phys.net/13/2939/2013/>.
- Slingo, A. (1989), A GCM parameterization for the shortwave radiative properties of water clouds, *J. Atmos. Sci.*, **46**, 1419–1427, doi:10.1175/1520-0469(1989)046<1419:CO;2>
- Smirnov, A., B. N. Holben, T. F. Eck, O. Dubovik, and I. Slutsker, 2000: Cloud-Screening and Quality Control Algorithms for the {AERONET} Database. *Remote Sensing of Environment*, **73** (3), 337–349, doi:10.1016/S0034-4257(00)00109-7, URL <http://www.sciencedirect.com/science/article/pii/S0034425700001097>.
- Soden, B., A. Broccoli, and R. Hemler, 2004: On the use of cloud forcing to estimate cloud feedback. *J. Climate*, **17**, 3661–3665, doi:10.1175/1520-0442(2004)017<3661:OTUOCF.2.0.CO;2>
- Soden, B., and I. Held (2006), An assessment of climate feedbacks in coupled ocean-atmosphere models, *J. Clim.*, **19**(23), 3354–3360, doi:10.1175/JCLI9028.1. Stephens, G. L., and T. L'Ecuyer (2015), The Earth's energy balance, *Atmos. Res.*, **166**, 195–203, doi:10.1016/j.atmosres.2015.06.024.
- Storelvmo, T., J. E. Kristjánsson, and U. Lohmann (2008), Aerosol influence on mixed-phase clouds in CAM-Oslo, *J. Atmos. Sci.*, **65**(10), 3214–3230, doi:10.1175/2008JAS2430.1.
- Su, H., and Coauthors, 2013: Diagnosis of regime-dependent cloud simulation errors in CMIP5 models using A-Train satellite observations and reanalysis data. *J. Geophys. Res. Atmos.*, **118**, 2762–2780, doi:10.1029/2012JD018575.
- Takemura, T. T. Nakajima, and O. Dubovik, 2002: Single-scattering albedo and radiative forcing of various aerosol species with a global three-dimensional model. *Journal of Climate*, **15**, 333–352, URL [http://journals.ametsoc.org/doi/abs/10.1175/1520-0442\(2002\)015%3C0333%3ASSAARF%3E2.0.CO%3B2](http://journals.ametsoc.org/doi/abs/10.1175/1520-0442(2002)015%3C0333%3ASSAARF%3E2.0.CO%3B2).

- Tegen, I. and I. Fung, 1995: Contribution to the atmospheric mineral aerosol load from land surface modification. *Journal of Geophysical Research*, **100 (D9)**, 18 707–18 726, doi: 10.1029/95JD02051, URL <http://dx.doi.org/10.1029/95JD02051>.
- Teixeira, J., and Coauthors, 2011: Tropical and subtropical cloud transitions in weather and climate prediction models: The GCSS/WGNE Pacific Cross-Section Intercomparison (GPCI). *J. Climate*, **24**, 5223–5256, doi:10.1175/2011JCLI3672.1.
- Torres, O., A. Tanskanen, B. Veihelmann, C. Ahn, R. Braak, P. K. Bhartia, P. Veefkind, and P. Levelt, 2007: Aerosols and surface UV products from Ozone Monitoring Instrument observations: An overview. *J. Geophys. Res.*, **112**, D24S47, doi:10.1029/2007JD008809.
- Tsushima, Y., S. Emori, T. Ogura, M. Kimoto, M. J. Webb, K. D. Williams, M. A. Ringer, B. J. Soden, B. Li, and N. Andronova (2006), Importance of the mixed-phase cloud distribution in the control climate for assessing the response of clouds to carbon dioxide increase: A multi-model study, *Clim. Dyn.*, **27**(2–3), 113–126, doi:10.1007/s00382-006-0127-7.
- Twomey, S., 1974: Pollution and the planetary albedo. *Atmospheric Environment*, **8 (12)**, 1251–1256, doi:10.1016/0004-6981(74)90004-3, URL <http://www.sciencedirect.com/science/article/pii/0004698174900043>.
- van Tricht, K., S. Lhermitte, J. T. M. Lenaerts, I. V. Gorodetskaya, T. S. L'Ecuyer, B. Noël, M. R. van den Broeke, D. D. Turner, and N. P. M. van Lipzig (2016), Clouds enhance Greenland ice sheet meltwater runoff, *Nat. Commun.*, **7**, 10266, doi:10.1038/ncomms10266.
- Vaughan, M. A., and Coauthors, 2009: Fully automated detection of cloud and aerosol layers in the CALIPSO lidar measurements. *J. Atmos. Oceanic Technol.*, **26**, 2034–2050, doi:10.1175/2009JTECHA1228.1.
- Verlinde, J., et al. (2007), The mixed-phase arctic cloud experiment, *Bull. Am. Meteorol. Soc.*, **88**(2), 205–221, doi:10.1175/BAMS-88-2-205.
- Vial, J., J. L. Dufresne, and S. Bony (2013), On the interpretation of inter-model spread in CMIP5 climate sensitivity estimates, *Clim. Dyn.*, **41**(11–12), 3339–3362, doi:10.1007/s00382-013-1725-9. Wallace, J. M., and P. V. Hobbs (2006), *Atmospheric Science*, pp. 419–465, Elsevier, doi:10.1016/B978-0-12-732951-2.50015-6.

- Waquet, F., J. Riedi, L. C. Labonnote, P. Goloub, B. Cairns, J.-L. Deuzé, and D. Tanré, 2009: Aerosol remote sensing over clouds using A-Train observations. *J. Atmos. Sci.*, 66, 2468–2480, doi:10.1175/2009JAS3026.1.
- Warren, S. G., R. M. Eastman, and C. J. Hahn, 2007: A survey of changes in cloud cover and cloud types over land from surface observations, 1971–96. *J. Climate*, 20, 717–738, doi:10.1175/JCLI4031.1.
- Wilcox, E., 2012: Direct and semi-direct radiative forcing of smoke aerosols over clouds. *Atmos. Chem. Phys.*, 12, 139–149, doi:10.5194/acp-12-139-2012.
- Wild, M., D. Folini, M. Z. Hakuba, C. Schar, S. I. Seneviratne, S. Kato, D. Rutan, C. Ammann, E. F. Wood, and G. König-Langlo (2014), The energy balance over land and oceans: An assessment based on direct observations and CMIP5 climate models, *Clim. Dyn.*, 44, 3393–3429, doi:10.1007/s00382-014-2430-z.
- Winker, D. M., and Coauthors, 2010: The CALIPSO Mission: A global 3D view of aerosols and clouds. *Bull. Amer. Meteor. Soc.*, 91, 1211–1229, doi:10.1175/2010BAMS3009.1.
- Winker, D. M., J. L. Tackett, B. J. Getzewich, Z. Liu, M. a. Vaughan, and R. R. Rogers, 2013: The global 3-D distribution of tropospheric aerosols as characterized by CALIOP. *Atmospheric Chemistry and Physics*, **13** (6), 3345–3361, doi:10.5194/acp-13-3345-2013, URL <http://www.atmos-chem-phys.net/13/3345/2013/>.
- Wong, J. and Z. Li, 2002: Retrieval of optical depth for heavy smoke aerosol plumes: uncertainties and sensitivities to the optical properties. *Journal of the Atmospheric Sciences*, 250–261, URL [http://journals.ametsoc.org/doi/abs/10.1175/1520-0469\(2002\)059%3C0250%3AROODFH%3E2.0.CO%3B2](http://journals.ametsoc.org/doi/abs/10.1175/1520-0469(2002)059%3C0250%3AROODFH%3E2.0.CO%3B2).
- Worley, P. and A. Craig, 2012: Performance of the Community Earth System Model. *Int. J. High Performance Computing Appl.*, 26, 17–30.
- Yu, H., 2004: Direct radiative effect of aerosols as determined from a combination of MODIS retrievals and GOCART simulations. *Journal of Geophysical Research*, **109** (D3), D03 206, doi:10.1029/2003JD003914, URL <http://doi.wiley.com/10.1029/2003JD003914>.

- Yu, H., et al., 2006: A review of satellite-based assessments of the aerosol direct radiative effect and forcing. *Atmospheric Chemistry and Physics*, **6** (3), 613– 666, doi:10.5194/acp-6-613-2006, URL <http://www.atmos-chem-phys.net/6/613/2006/>.
- Zatko, M. C., and S. G. Warren (2015), East Antarctic sea ice in spring: Spectral albedo of snow, nilas, frost flowers and slush, and light-absorbing impurities in snow, *Ann. Glaciol.*, 56(69), 53–64, doi:10.3189/2015AoG69A574.
- Zelinka, M. D., S. A. Klein, K. E. Taylor, T. Andrews, M. J. Webb, J. M. Gregory, and P. M. Forster (2013), Contributions of different cloud types to feedbacks and rapid adjustments in CMIP5, *J. Clim.*, 26(14), 5007–5027, doi:10.1175/JCLI-D-12-00555.1.
- Zhang, Y., W. B. Rossow, A. A. Lacis, V. Oinas, and M. I. Mishchenko (2004), Calculation of radiative fluxes from the surface to top of atmosphere based on ISCCP and other global data sets: Refinements of the radiative transfer model and the input data, *J. Geophys. Res.*, 109, D19105, doi:10.1029/2003JD004457.
- Zhang, J., 2005: Shortwave aerosol radiative forcing over cloud-free oceans from Terra: 2. Seasonal and global distributions. *Journal of Geophysical Research*, **110** (D10), D10S24, doi:10.1029/2004JD005009, URL <http://doi.wiley.com/10.1029/2004JD005009>.
- Zuidema, P., et al., 2016: Interactions: Smoke and Clouds above the Southeast Atlantic Upcoming Field Campaigns Probe Absorbing Aerosol's Impact on Climate, *Bull. Am. Meteorol. Soc.*, 19–23, doi:10.1175/BAMS-D-15-00082.1.